Fatigue Crack Growth in Laser Shock Peened Aerofoils Subjected to Foreign Object Damage

Sven Klaus Spanrad, Dipl. Ing (FH)

A thesis submitted to the University of Portsmouth for the degree of

Doctor of Philosophy

2011

To my family

DECLARATION

Whilst registered as a candidate for the above degree, I have not been registered for any other research award. The results and conclusions embodied in this thesis are the work of the named candidate and have not been submitted for any other academic award.

Signed: Date:

ACKNOWLEDGEMENTS

I wish to express my profound debt to my first supervisor and Director of Studies, Professor J. Tong for the enthusiastic support and guidance provided throughout my period of study and the encouragement for personal development.

I would also like to thank my second supervisor Dr L.G. Zhao for his advice during the modelling phase and gratitude for proof-reading this thesis.

Special thanks are due to all the members of the Mechanical Behaviour of Materials group of the University of Portsmouth, and in particular, Mr C. Lupton for all his help during the experimental phases and otherwise, as well as Dr L. Bing for always kind and productive cooperation for the analytical part of this study. I would like to thank all the colleagues past and present with whom I shared my office during these last three years.

I wish to thank Prof. Dr-Ing Habil. H.-J. Christ for his support and for always making himself available for discussions along with his associates; for excellent assistance during my research at the University of Siegen.

Finally I would like to express my gratitude to all my family and friends for believing in me and their continued, patient support, understanding and encouragement during the course of this work

The research project was fully funded by the Engineering and Physical Science Research Council and the Ministry of Defence, UK. Rolls-Royce plc provided the test specimens. Thanks also to the colleagues at the Universities of Manchester and Oxford for carrying out some of the experimental work related to this study.

ABSTRACT

Foreign Object Damage (FOD) is one of the main life limiting factors for aeroengine fan blades. The FOD impacts during takeoff and landing cause severe damage to aerofoils, resulting in reduced air safety and life time with an estimated annual cost of $4 billion for the aeroengine industry. Advanced surface treatments, such as Laser Shock Peening (LSP) have significantly improved the fatigue strength and crack growth resistance of critical components under FOD. However, it is not yet possible to predict the protective residual stresses and utilise their full potential for enhancing fatigue resistance and damage tolerance capacity in service. This research programme aims to utilise some of the established methods for fatigue tolerance assessment of critical components, based on fracture mechanics principles, to address the effects of complex residual stresses due to LSP and FOD on fatigue crack growth in aerofoils under simulated service loading conditions.

The experimental study involved fatigue testing of LSPed and FODed specimens with a geometry representative of fan blades made from Ti-6Al-4V alloy. A four point bend fatigue test setup was designed and calibrated. A real-time computer-controlled crack growth monitoring system and optical crack monitoring techniques were developed. Scanning Electron Microscopy (SEM) and Back-Scatter Electron (BSE) were used to conduct metallographic and fractographic studies, including crack initiation, early fatigue crack growth and FOD damage characterisation. The fracture mechanics analyses used the weight function method and the finite element method to obtain a modified stress intensity factor considering residual stresses due to LSP and FOD. Fatigue crack growth data under low cycle fatigue (LCF), high cycle fatigue (HCF) and combined LCF and HCF loading conditions were correlated using a standard and the modified stress intensity factors. The influence of impact angles and loading conditions on fatigue crack growth behaviour was assessed, and the results were compared with those from untreated FODed specimens.

CONTENTS

NOMENCLATURE

Symbols

a	Crack length
B	Specimen thickness
C	Constant used in the Paris equation
da/dN	Crack growth per number of cycles
da/dB	Crack growth per number of blocks
f	Frequency
h	Specimens thickness
I_x	Moment of inertia
J	Joule
K	Stress intensity factor
K_{app}	Applied stress intensity factor
K_{eff}	Effective stress intensity factor ($K_{eff}=K_{app}+K_{res}$)
K_{max}	Maximum stress intensity factor
K_{min}	Minimum stress intensity factor
K_{norm}	Normalised stress intensity factor
K_{op}	Crack opening stress intensity factor
K_t	Stress concentration factor
K_{res}	Residual stress intensity factor
K_I	Stress intensity factor in Mode I, plain strain conditions
K_c	Critical stress intensity factor
L	Support-roller spacing
L/t	Ratio of support-roller spacing / load-roller spacing
M	Bending moment
m	Material constant
$m_{(x,a)}$	Weight function term
N	Number of cycles
P	Load
Q	Quantity of heat
R^2	Coefficient of determination
R	Load ratio
R_{eff}	Effective load ratio
R_{minor}	Load ratio of minor cycle
R_{major}	Load ratio of major cycle
t	Load roller-spacing
t/W	Ratio of load-roller spacing/specimen width
V_{act}	Active potential
V_{ref}	Reference potential
V_r	Voltage ratio V_{act}/V_{ref}
W	Specimen width

Y	Geometry or shape factor
y	Distance in Y direction from the neutral axis
α	Low temperature from of titanium
β	High temperature form of titanium
Δa	Crack increment
ΔK	Stress intensity range (K_{max} - K_{min})
$\Delta K_{app, max}$	Maximum effective applied stress range
$\Delta K_{app, min}$	Minimum effective applied stress range
ΔK_{eff}	Effective stress intensity range
$\Delta K_{eff, max}$	Effective maximum stress intensity range
$\Delta K_{eff, min}$	Effective minimum stress intensity range
ΔK_{HCF}	Stress intensity range for HCF cycles
ΔK_{LCF}	Stress intensity range for LCF cycles
ΔK_{major}	Stress intensity factor associated with a major cycle
ΔK_{max}	Maximum stress intensity range
ΔK_{minor}	Stress intensity factor associated with a minor cycle
ΔK_{min}	Minimum stress intensity range
ΔK_{onset}	Value of ΔK_{total} at which the onset of minor crack growth occurs
ΔK_{th}	Derived threshold stress intensity factor
ΔK_{total}	Stress intensity factor associated with a total cycle
Δσ	Local stress range
$\Delta\sigma_{max}$	Maximum stress range
$\Delta\sigma_{min}$	Minimum stress range
$\Delta\sigma_{nom}$	Nominal stress range
$\Delta\sigma_{peak}$	Peak stress range
σ	Applied stress
σ_{max}	Maximum stress in the load cycle
σ_{res}	Residual stress
σ_y	Yield tensile stress
ϴ	FOD impact angle
δ	Relative error

Abbreviations

ASB	Adiabatic shear-bands
ASTM	American Society for Testing Materials
BSE	Back-scatter electron
CCF	Combined cycle fatigue
DC	Direct current
DCPD	Direct current potential drop method
DR	Deep rolling
DSTL	Defence Science and Technology Laboratory
DVM	Digital voltmeter
EBSD	Electron back-scatter detection
EDM	Electro discharge machining
EN	European norm
ENSIP	Engine structural integrity program
EPSRC	Engineering and Physical Sciences Research Council
FCG	Fatigue crack growth
FCGR	Fatigue crack growth rate
FE	Finite element
FEM	Finite element method
FOD	Foreign object damage
HCF	High cycle fatigue
Hz	Hertz
ISDG	Interferometric strain/displacement gauge
LCF	Low cycle fatigue
LEFM	Linear plastic fracture mechanics
LE	Leading edge
LOM	Loss of material
LPB	Low plasticity burnishing
LSP	Laser shock peening
MSRR	Material Standard Rolls-Royce
MOD	Ministry of Defence
NDI	Non-destructive inspections
PC	Personal computer
PD	Potential drop
RS	Residual stress
SIF	Stress intensity factor
SEM	Scanning electron microscopy
SP	Shot peening
SR	Surface replicas
TEM	Transmission electron microscopy
USAF	United States Air Force
UK	United Kingdom
UoP	University of Portsmouth

UoM	University of Manchester
WF	Weight function
WFM	Weight function method
XRD	X-Ray Diffraction

1 Introduction

1.1 Background

FOD refers to Foreign Object Damage caused by objects ingested into turbine engines during takeoff and landing, the velocities of the objects can reach 60 to 500m/s. These impacts cause severe damage to parts of aeroengines, with the leading edge of aerofoils particularly susceptible. FOD has been identified as one of the main life limiting factors for aeroengine fan blades. The list of typical runway debris, acting as ingested projectiles are extensive and can be divided into two categories of "soft body" debris, such as ice, cloth rags and animals; and "hard body" debris, such as rocks and small metallic objects. Boeing estimated that the annually direct costs for aeroengine maintenance are about $4 billion for the aeroengine industry (Bachtel, 1998). A study by Insight SRI Ltd., UK (2008) suggested that indirect costs such as delays[1] or fuel inefficiency[2] (2 cases out of 33) would be roughly 10 times the direct costs.

The occurrence of FOD in fan and compressor blades can significantly reduce the high cycle fatigue (HCF) resistance of advanced turbine engines. The reduction of fatigue strength is related to highly elevated tensile stresses and microcracks from FOD impacts onto the surface of the components. From a FOD site, at a blade resonant frequency within the engine's speed regime, the cyclic stress can be sufficient to initiate and propagate a crack. In 1994, the U.S. Air Force initiated a program entitled the "National High Cycle Fatigue Science and Technology Program" to better understand HCF and its relationship to FOD. Research results of this program led to good design practice and new design initiatives for FOD prevention and mitigation,

[1] At large airports the costs can come to well over $1 million per year.
[2] For example, the operating costs for a Boeing 767 for a typical flight would increase by $147.85 per flight. This indirect fuel costs alone is more than three times the direct engine costs per flight ($47).

including damage tolerant design methods, enhanced blade coatings, inlet particle separators, and surface treatments such as laser shock peening.

A laser shock peening (LSP) technology has been applied to turbine engine blades by introducing compressive residual stresses in the components surface layer to improve FOD resistance. Compared to traditional surface treatments such as shot peening used often in civil aviation, LSP introduces a layer of 10 times deeper compression, which is more effective against FOD (Ruschau et al., 1999a; 1999b). LSP treated engine blades were reported to last 3 to 5 times longer than non-peened blades (Heller, 1998). The U.S. Air Force used LSP to treat fan blades (B-1B program)[3] and found that the treatment was essentially insensitive to FOD defects up to 6.35mm deep (See, 2000; Tenaglia and Lahrman, 2003). Stronger engine blades result in less FOD to engines, less risk to aircraft and improved air safety. Despite the higher costs of LSP in the manufacturing process of engine blades, it has avoided over $59 million in costs through reduced blade replacement, reduced secondary damage engine repair, and avoidance through airfoil failures. Additionally, $40 million cost avoidance was realised by avoiding 42 catastrophic failures, according to U.S. Air Force (Web site 1-1). Calculating this impact over all engines in the Air Force fleet, the potential savings could easily approach one billion dollars (Web site 1-1).

A fundamental understanding of fatigue damage process due to FOD in the presence of LSP is vital, if such advanced surface treatments are to be utilized to their full potential for enhancing fatigue resistance of engine blades. Although methods for damage tolerance assessment of critical components based on fracture mechanics principles are well established, methods of dealing with the effects of residual stresses due to FOD or LSP on fatigue behaviour of these components are in their infancy. It is not yet possible to predict the most favourable residual stress states for improvements in damage tolerance capacity in service. Numerous LSP parameters must be tested by costly trial-and-error and the costs increase sharply with the need for extensive specimen and component testing under service loading conditions. The proposed work aims at characterising fatigue crack growth due to FOD in LSP treated aerofoil

[3] The B-1B Lancer is a four-engine, variable-sweep wing strategic bomber used by the U.S. Air Force.

specimens to assess the effects of complex residual stresses caused on crack driving force under service loading conditions.

1.2 Aims and objectives

This project brought together the Mechanical Behaviour of Materials Group at the University of Portsmouth (UoP) and the Residual Stress group at the University of Manchester (UoM) to tackle the influence of surface residual stresses on fatigue crack growth behaviour due to FOD and LSP. The proposed research has been developed in collaboration with the Defence Science and Technology Laboratory (DSTL), Rolls-Royce plc., and QinetiQ. The project was funded by the Engineering and Physical Science Research Council (EPSRC) and the Ministry of Defence (MOD), UK. Aerofoil type specimens were provided by Rolls-Royce plc., who also provided the surface treatment (LSP) of the specimens prior to FOD.

The aim of this thesis is to understand how foreign object damage influences fatigue crack growth behaviour in aerofoil samples protected by deep compressive residual stresses under service loading conditions, using essentially experimental approaches. The residual compressive stresses were introduced by LSP, FOD was simulated by using a gas gun, and loading conditions were representative of flight cycles including both high cycle fatigue (HCF) and low cycle fatigue (LCF) loading conditions.

The specific objectives to reach the aim are:

- To develop an accurate experimental method to test complex shaped aerofoil specimens, to carry out mechanical testing under LCF, HCF and combined LCF and HCF loading conditions and monitor fatigue crack growth.

- To conduct metallographic and fracographic studies on LSP+FODed samples to characterize the morphology of FOD damage, crack initiation and early crack growth.
- To use the concept of Fracture Mechanics and the finite element method to consider residual stresses due to LSP and FOD, and to modify the stress intensity factor.
- To correlate the fatigue crack growth rates using standard and modified stress intensity factors.
- To compare fatigue crack growth behaviour due to FOD in LSPed and untreated specimens to assess the influence of LSP.

1.3 The research programme

The research presented in this thesis contains both experimental and numerical aspects. A schematic illustration of the thesis's outline is given in Figure 1-1.

Chapter 2 aims to set the stage for this research based on a comprehensive review of the literature related to the topics of the research, including basic concepts of fracture mechanics and fatigue, as well as the research activities carried out up to date on the studies of FOD, LSP and fatigue behaviour of materials under service loading conditions. The experimental work of simulating FOD, calibrating and setting up crack monitoring methods and the mechanical test system is presented in Chapter 3. Further, this chapter provides information on the types of damage and loading conditions considered, test specimen geometry, surface treatments (LSP), and material details. Typical damage characteristics and their role in the crack initiation and early crack growth under simulated service loading conditions obtained by optical examination are covered in Chapter 4. Chapter 4 also presents comparisons with research results from previous studies such as cubical FOD impacts from specimens without LSP and those of spherical FOD impacts.

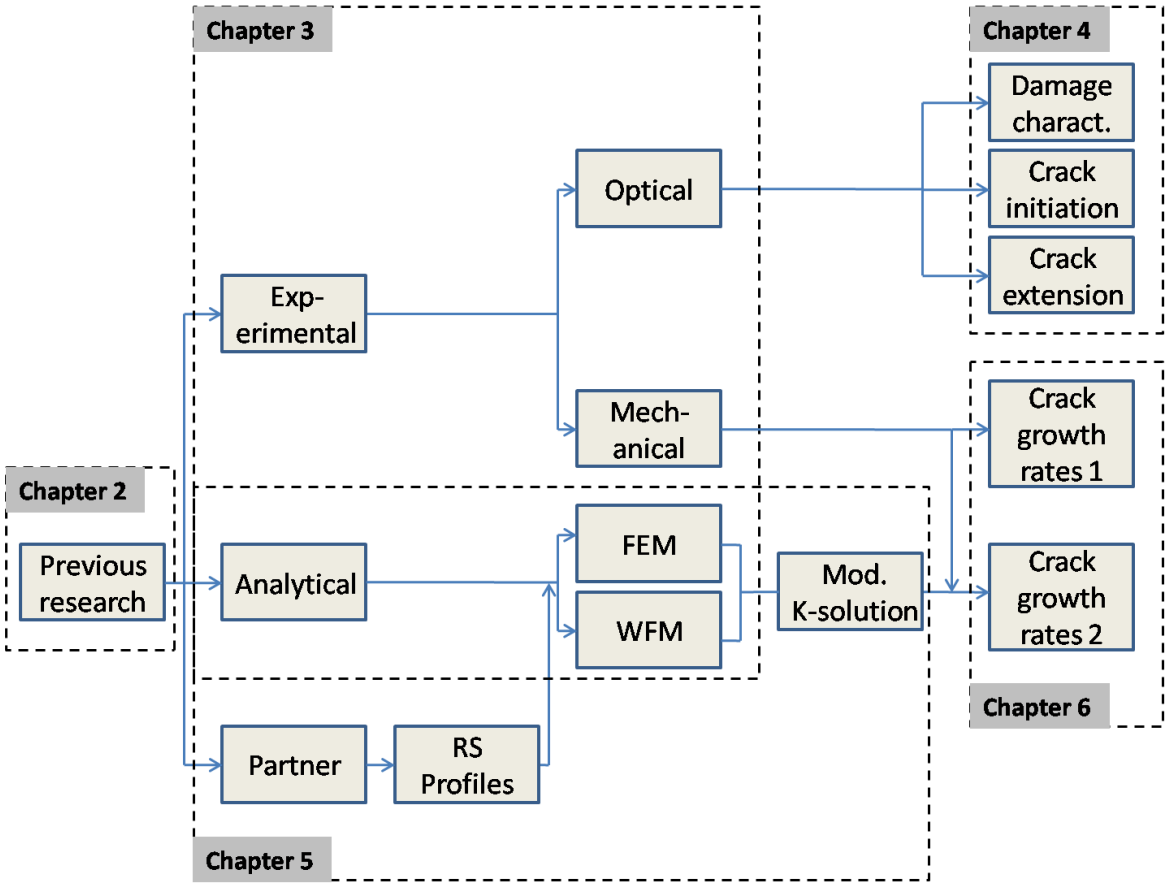

Figure 1-1 Schematic outline of the thesis.

Chapter 5 presents a study on the application of the weight function method and the finite element method to evaluate the crack driving force in the presence of residual stresses due to LSP and FOD. Experimentally measured one-dimensional residual stress distributions provided by our research partner were used in the analyses and the results of both methods were compared and processed for further application in Chapter 6. Chapter 6 focuses on the fatigue crack growth characterisation. The crack growth rates are correlated with the stress intensity factors using a standard single edge crack solution and a modified stress intensity factor (Chapter 5). The results are discussed with regard to the role of residual stresses in the characterization of fatigue crack growth due to head-on and 45° impact under LCF, HCF and combined LCF and HCF loading conditions. Results of the present specimens (LSPed+FODed) were also compared with those from unpeened FODed specimens of the same alloy from a previous study.

1.4 References

Bachtel, B., 1998. Foreign object debris and damage prevention. Aeromagazine 1, Article S.

Heller, A., 1998. Blasts of Light Strengthen Metals. Web site: https://www.llnl.gov/str/Hackel.html.

Insight SRI Ltd., UK (2008). The economic cost of FOD to airlines. No 400, 456-458, The Strand, London, WC2R 0DZ, UK.

Ruschau, J.J., Reji, J., Thompson, S.R., Nicholas, T., 1999a, Fatigue crack growth rate characteristics of laser shock peened Ti-6Al-4V. Journal of Engineering Materials and Technology 121, 321-329.

Ruschau, J.J., Reji, J., Thompson S.R., Nicholas T., 1999b. Fatigue crack nucleation and growth rate behaviour of laser shock peened titanium. International Journal of Fatigue, 199-209.

See, D., 2000. Laser Shock Peening - The Right Technology at the Right Time. Air Force Research Laboratory. Web site: http://www.ml.afrl.af.mil/stories/mlm-00413.html.

Tenaglia, R.D., Lahrman, D.F., 2003. Preventing fatigue failures with laser peening, AMPTIAC, Vol. 7, No. 2., 3-7.

Web site 1-1. Air Force Research Laboratory AFRL. High-cycle fatigue. Available: http://www.ml.afrl.af.mil/publications/factsheets/High_Cycle_Fatigue.pdf. Last accessed 01/02/2011.

2. Literature review

It has been estimated that approximately 90% of all engineering failures can be attributed to fatigue (Anderson et al., 1990). Fatigue crack growth may be divided into two stages: Crack initiation and crack growth (Forsyth, 1963). Both require the accumulation of irreversible plastic deformation due to repeated stress cycles. Hence, a total fatigue life will be the summation of the life spent initiating a crack and subsequently propagating it to a critical value, which may be the critical crack length necessary for fast fracture to occur (Figure 2-1).

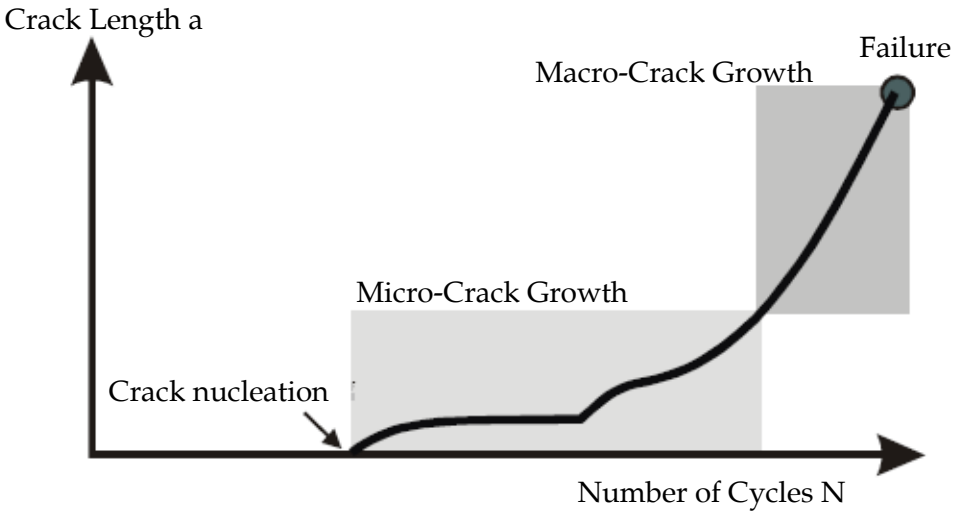

Figure 2-1 A schematic of the stages of fatigue crack growth.

Generally, cracks develop at free surfaces where the material is often exposed to environmental effects and applied stresses are high (Broek, 1986). In idealised defect-free pure metals, cracks initiate as a result of the formation of persistent slip-bands. Common to most materials are sub-surface-defects (shrinkage, gas porosity or

impurities) and notch like features resulting from scratches, which potentially serve as initiation sites for cracks from which early crack growth may occur.

In Stage I, micro-crack growth is also referred to as "small-crack growth" regime, where a microcrack develops at approximately 45° to the direction of the nominal tensile stress in a length scale of 1-10μm. The phases of crack nucleation and micro-crack growth can consume up to 90% of the service performance of a component (Pearson, 1975; Erdogan, 2000; Suresh, 2001). The transition from micro- to macro-crack growth is called Stage II crack growth, where a crack propagates on a plane normal to the maximum tensile stress. The crack grows faster and usually forms beach marks known as striations, indicating the position of the crack fronts on successive load cycles. Striations often indicate the number of cycles experienced.

Based on this theory, the safe-life approach has been developed for designing components against fatigue. This approach determines the components life by conducting a rig test under typical in-service conditions. The endurance or fatigue limit is defined as the cyclic stress sustained by the specimen over 10^7 cycles. The end of life point is taken to be either life to first engineering crack (>0.75mm) or a fraction of life to rapid fracture. However, in fracture critical applications in certain aircraft components, the existence of initial defects formed during manufacturing processes or in-service accidents such as foreign object damage is often unavoidable and must be accounted for.

These considerations led to a new design philosophy, damage tolerance, which is based on fracture mechanics. This concept assumes that a defect in a component will act like a crack under service conditions; hence analysis should be focused only on the propagation life of the component. The initial defect size is often determined by non-destructive inspection (NDI) limits and the critical crack length may be estimated from the applied stress and material properties. The life is determined by using fracture mechanics concepts and ensures that, at any time, the remaining fatigue life to grow a crack until fracture is greater than the expected service duration. This life may be used in conjunction with the safe-life method, allowing appropriate inspection intervals to be determined, which is usually half the

predicted crack growth life (tolerable crack length). If no crack or a crack smaller than the tolerable crack length is detected during these inspections, the component is returned to service until the predicted safe life is reached.

Crack growth laws based on fracture mechanics are necessary to predict crack propagation lifetime and determine the inspection intervals accurately. In this context, one of the objectives of the current study is to determine fatigue crack growth under surface treatment (LSP) and surface damage (FOD) to describe fatigue crack growth behaviour based on a damage tolerant concept. The stress intensity factor (SIF) approach allows applications of basic fracture mechanics to quantify fatigue crack growth and to assess the remaining fatigue life.

2.1 Basic Fracture Mechanics

Stress intensity factor, K, is one of the most important concepts in linear elastic fracture mechanics (LEFM), and is a single-parameter which provides a measure of the intensity of the near-tip stress fields under linear elastic conditions. In general, a cracked body can be loaded in three possible modes of crack surface displacements for which stress intensity factors can be calculated. The majority of engineering fatigue failures, however, is predominantly caused by the most damaging tensile Mode I, where cracks grow perpendicular to the applied load (Campbell and Ritchie, 2000). This study focuses on this load type and further references to the SIF will refer to the stress intensity factor in Mode I, K_I, which may be expressed in terms of crack size, a, remote stress, σ, and a geometry factor, Y as:

$$K = \sigma\sqrt{\pi a}\,Y \tag{2-1}$$

For standard loading conditions and geometries, Y can often be obtained from handbooks such as (Tada et al., 1973; Rooke and Cartwright, 1976). Paris and Erdogan (1963) demonstrated that the rate of crack propagation is governed by the

cyclic stress intensity factor ΔK, defined as the difference between the maximum and minimum values of K in a fatigue cycle:

$$\Delta K = K_{max} - K_{min} \tag{2-2}$$

The typical life of a material subjected to a constant cyclic load is shown in a sigmoidal curve in Figure 2-2. Region I has very low crack growth rates and a fatigue threshold, ΔK_{th}, below which crack growth is extremely low, typically below 10^{-10}m/cycle (ASTM, 1995). In Region III crack growth rates increase rapidly with increasing ΔK towards fast fracture bounded by the fracture toughness, K_C. Region II shows a log-log relationship between ΔK and da/dN, usually referred to as the Paris law:

$$\frac{da}{dN} = C(\Delta K)^m \tag{2-3}$$

where C and m are material constants.

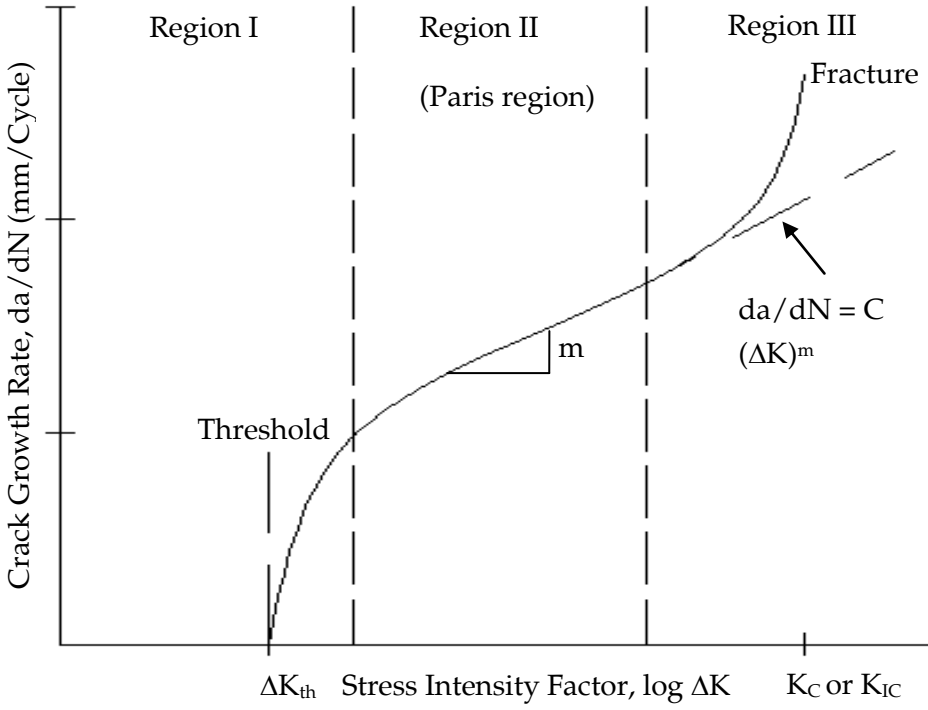

Figure 2-2 A Schematic illustration of fatigue crack growth behaviour in metals.

The fatigue crack growth rates can be influenced by the phenomena of crack closure effects. Elber (1971) observed that cracks can physically close behind the crack tip by contact of cracked surfaces, even under a nominal tensile load. This contact may occur at a stress intensity level above the K_{min} value of a cycle. Thus, the fatigue crack growth rate might no longer be determined by the nominal value of stress intensity factor ΔK, rather by an effective value of ΔK:

$$\Delta K_{eff} = K_{max} - K_{op} \tag{2-4}$$

where K_{max} is the maximum stress intensity factor and K_{op} is the stress intensity factor to open the crack. This equation accounts not for the mechanism of crack closure, for example due to plastic wake, oxidation, fracture surface misalignment (Suresh, 2001). Studies on fatigue of LSPed materials by Ruschau et al. (1999a; 1999b) for Ti-6Al-4V and Hatamleh (2009) for an Al alloy, reported increased crack closure effects due to the high compressive residual stresses. In the current study, LSP treatment and FOD impact both generate considerable residual stresses; hence closure effects should be examined. Plasticity-induced crack closure was proposed by Elber (1971) arising from the consideration of the plastic zones left behind as the crack advances. The plastic wake tends to be a source of compressive residual stress, which presses the crack flanks together. This may superimposes a constant negative stress on the applied cyclic stress and shifting the mean stress of the cycle to a lower value (Oakley and Nowell, 2007). Oxide-induced closure (Endo et al., 1969) may be explained by a gradual breaking and reforming of the oxide scale formed behind the crack tip due to repeated contact between the fracture surfaces, along with any debris originated from a foreign source or the cracked materials. Roughness-induced crack closure, originally termed as non-closure by Beevers (1981), arises due to the rough nature of the fracture surfaces as the two halves of the crack do not fit together perfectly. Opposing asperities will come into contact at some point, transmitting stress across the crack faces and causing closure effects.

Fatigue crack initiation and growth behaviour can be influenced by stress raiser such as a hole or a notch e.g. as a result of FOD. The presence of a notch introduces an

increase in stress or stress concentration at the root of the notch, where a stress gradient starting from the root of the notch toward the centre of the sample, and a triaxial stress state. The effect of notch may be measured by the stress concentration factor, K_t, which may be derived based on the notch geometries (Peterson, 1974). The stress concentration factor is the peak stress at the root of the notch and the nominal stress that would be present if the notch did not exist.

$$K_t = \frac{\sigma_{peak}}{\sigma_{nom}} \tag{2-5}$$

Haritos et al. (1999) and Lanning et al. (1999) characterised FOD as a notch using the K_t factor to estimate the remaining fatigue life, but concluded that many factors besides the notch geometry affects the fatigue life of a notched component, such as notch root plasticity along with stress state and stress ratio at the notch root. The influence of each parameter upon fatigue limit predictions must be recognized. A K_t based stress description is inappropriate when notch root plasticity is present. This plasticity can change the level of fatigue reduction resulting in fatigue conditions different from those estimated from K_t. This fact limits the K_t approach for the application of FOD-induced notches such as geometrical irregularities of the FOD notch, the residual stresses resulting from the impact and the LSP treatment. In addition, the geometry of FOD notches is highly influenced by geometry of the component. Generally the V-notches possess a very sharp notch root radius and the corresponding K_t solutions are not available in standard reference books. K_t factor may be used to compare FOD notches resulting from different impact conditions though.

2.2 Fatigue crack growth under LCF, HCF and combined LCF+HCF loading

Fatigue may be divided into two categories: Low-cycle fatigue (LCF) and high-cycle fatigue (HCF). LCF refers to fatigue cycles with large amplitudes (R≈0) and low frequencies (0.01 – 1Hz), often under strain-control, where total number of fatigue lives is typically less than 10^4 - 10^5 cycles; as opposed to HCF where fatigue cycles consist of small amplitudes (R≥0.7) and high frequencies (100 – 10,000), often under load-control, and total number of fatigue lives usually exceeds 10^6 cycles (Suresh, 2001; Nicholas, 2006).

Gas turbine aero-engine components such as discs and blades usually experience complex load spectrums derived from thermal and mechanical stresses during a flight cycle. The loading of a typical flight cycle can be simplified by dividing it into the three phases: 1) Take off and initial climb, 2) climb and 3) cruise (Hawkyard, 1997). The large amplitude, low frequency loadings during takeoff and landing would contribute to LCF and usually referred to as major cycles. The rotary motions of a gas turbine engine give rise to vibrational, or minor stress, cycles, mainly during cruise. The stress ratios of these cycles are usually greater than 0.8 and they are superimposed on the peak of the major cycles. These minor cycles contribute to HCF.

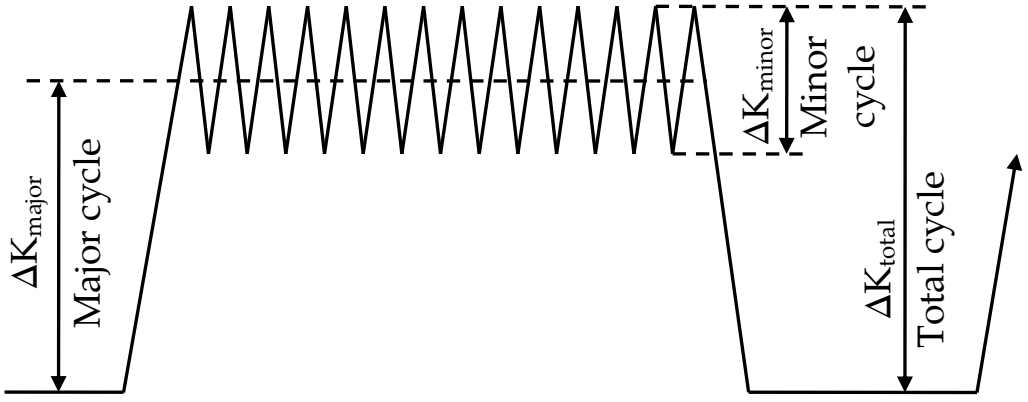

Figure 2-3 Schematic of a combined LCF + HCF cycle fatigue load block (Powell, 1985).

Figure 2-3 shows the major cycle (LCF) as a trapezoidal stress wave with a hold time in between them during which HCF cycles are superimposed. LCF loading produces a stress intensity factor range ΔK_{major} during its dwell times at maximum K, a vibratory loading occurs whose range is denoted by ΔK_{minor}. In the combined loading case, the total contribution of the total growth rate is the sum of $\Delta K_{total}+\Delta K_{minor}$ since the LCF cycle now goes from minimum to maximum through an amplitude ΔK_{total} (Nicholas, 2006). The load ratios in combined loading consist of R_{minor} and R_{major}, representing the values of R for HCF and LCF cycles, respectively. The number of HCF cycles per LCF cycle is given by n. Combined LCF+HCF loading can be referred as combined cycle fatigue (CCF). The CCF loading pattern consisting of one major cycle with n minor cycles superimposed has been termed as one loading block, and the FCG rate is written as da/dBlock or da/dB, ΔK_{total} or ΔK_{major} may be used to correlate the crack growth rate (Powell, 1985).

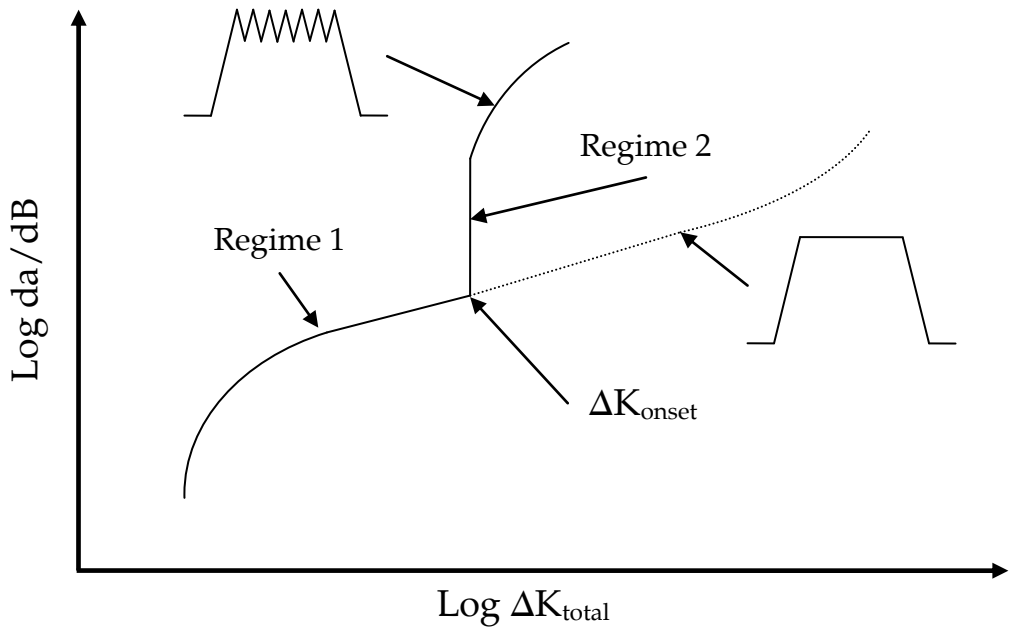

Figure 2-4 Fatigue crack growth regimes for LCF+HCF loadings (Byrne et al., 2003).

When CCF loading is applied, crack growth behaviour is shown to follow two different patterns, as depicted in Figure 2-4 where the minor cycle prompts faster crack growth once an onset is reached (Byrne et al., 2003). The LCF growth rates

follow the rate for LCF alone below ΔK_{onset}. A transition to an accelerated crack growth occurs when the threshold ΔK_{onset} is reached, and if the number n of HCF cycles per block is high enough (Powell and Duggan, 1986; Hawkyard et al., 1996; Powell et al., 1997; Byrne et al., 2003). On the other hand, a decrease in the HCF vibratory amplitude significantly increased the fatigue life by delaying the onset of HCF crack growth (Hall and Powell, 1997; Powell et al., 1997). Similarly, Cowles (1996) studied CCF fractured surfaces and observed the LCF and HCF portions of the applied cycle at distances greater than 0.75mm from the initiation point, but a decrease and eventual disappearance of damage attributed to HCF loading when moving closer to the origin. A single and block LCF overloads influence the crack growth rates and an increased stress intensity level is required for the onset of HCF growth (Byrne et al., 2003). It was concluded that HCF crack growth could be suppressed by increasing the magnitude of LCF overload.

A few studies investigated the fatigue behaviour of FODed materials under LCF+HCF loading conditions. Oakley and Nowell (2007) introduced an elastic short-crack arrest approach to estimate the fatigue life of Ti-6Al-4V blade-like specimens subjected to FOD under combined high- and low-cycle fatigue loading conditions. The studies of (Ruschau et al., 1999a; 1999b; Ding et al., 2007a; 2007b; Hall et al., 2008) focused on the fatigue crack growth behaviour due to FOD. Ding et al. (2007a; 2007b) found, for combined LCF+HCF loading, no onset point ΔK_{onset} for the fast crack growth but overall higher FCG rates for LCF+HCF loading conditions compared with those under LCF loading. It was concluded that HCF cycles contribute to crack growth from the very beginning, suggesting the disappearance of ΔK_{onset}. Ruschau et al. (1999a; 1999b) investigated the combined loading behaviour of FODed aerofoil shaped LSPed specimens and found that under high compressive residual stresses the FCG behaviour is dominated by HCF at high stress ratios.

2.3 Foreign Object Damage (FOD)

One of the earliest studies conducted on the effect of FOD on fatigue was in 1956 by Kaufman and Meyer (1956). The type and location of impact damage were studied by simulating FOD on the first stage compressor blades and fatigue testing of these blades until failure. The most detrimental region in terms of the reduction in fatigue resistance was found at 30% of the span from the base of the aerofoil, in the area where maximum vibratory stresses occurred. Away from this critical area, there was little reduction of fatigue life. Notch damage, even of smaller sizes, was observed to be more detrimental than that caused by dents. The subsequent study of Kaufman (1958) investigated the fatigue strength of reworked blades, where the FOD damage was simulated on compressor blades with a pendulum perpendicular to the edge of the specimen, forming small V-notches. The blades were made of stainless steel and the suggested process to rework blades showed restorable effects on the fatigue strength. Spakowski (1957) investigated blades using a rapid emission spectroscopic method to identify the type and properties of the objects ingested into the turbine. The analysis found 14 elements and classified these for aluminium and stainless steel blades.

Until the 1980 there was little research carried out in the area of FOD. The study of Nicholas et al. (1980) was the first to investigate the impact damage on leading edges of titanium alloy in relation to impact speed, firing small spheres over a range of velocities of 120 to 490m/s. A relation between the impact speed and the impact damage was found, and after subsequent fatigue tests the damage due to different speeds was correlated to its effect on fatigue life reduction. Further, it was demonstrated that a stationary blade was sufficient to simulate FOD damage, and this provided a good basic principle to study the influence of FOD on blades.

The Engine Structural Integrity Program (ENSIP, 1999) was initiated in 1984 by the U.S. Air Force (USAF) and aimed to adopt a damage tolerant approach in new design of critical components. Extensive experimental investigations for different titanium alloys were carried out under LCF conditions providing a database for damage tolerant design of gas turbine engine components. Similar data were

obtained under HCF conditions in this program, but have been recognised later in the 1990 as being inadequate in the presence of FOD to predict HCF strength of airfoils (Cowles, 1996; Nicholas, 1999).

In 1994, the USAF initiated the "National High Cycle Fatigue Science and Technology Program". The program focused on the capability of titanium and nickel-base alloys for propulsion systems to withstand HCF after being subjected to initial and service induced damage such as high and low cycle fatigue interactions, foreign object damage and fretting fatigue. Cowles (1996) and Larson et al. (1996) reviewed the current industrial methodologies to design for HCF within aero engines, and accounted reduced HCF capability due to critically located FOD, and much research was necessary to understand how FOD affects HCF failures.

Field surveys were carried out to evaluate the characteristics of FOD damage. Typical FOD damage was found to consist of dents, tears and notches at the leading edge of the aerofoil blades with sizes in a range from 0.05mm up to 13mm with an average depth of approximately 1.5mm (RTO, 2005). Pratt & Whitney and the USAF determined, in an extensive field study of FOD damage (Haake et al., 1989; Larson et al., 1996), a typical FOD geometry by measuring the FOD-root radii and correlating it to the number of occurrence. Together with the notch depth an average elastic stress concentration factor K_t of about 4 was determined, but maximum values of K_t up to 10 were seen for more severe FOD notches.

During the USAF's HCF program, five practicable methods for imparting damage under laboratory conditions were identified, listed in perceived order of increasing difficulty, these are: Notch-machining, shear chisel application, quasi-static indentation, solenoid gun usage, and light gas gun impact. The methods for simulation FOD damage differ from each other in terms of controlling notch parameters such as geometry and notch depth, introduction of residual stresses, changes in microstructure, impact induced cracking, and resistance of a given blade design. Specifications of the particular simulation methods can be found in (RTO, 2005; Nicholas, 2006).

Several studies of the Lambda Research (Cincinnati) (e.g. Prevey et al., 2001; 2002; 2003; 2004a; 2004b; Jayaraman et al., 2005) simulated FOD by electrical discharge machining. The machined V-notch was chosen as a reproducible simulation of the FOD notch. Major differences between machining and the impact event are the different residual stresses introduced, lack of change in the microstructure of the material and lack of impact-induced cracking.

Shear chisel, quasi-static indentation, and solenoid gun are quick and affordable methods for simulating FOD which also produce significant residual stresses unlike machining, but the amount of stress and cold work are very different from those created by in-service FOD (RTO, 2005). In addition, material removal can be caused by the dynamics of this impact method. These characteristics are closer to in-service FOD damage than the notch produced by machining.

Ballistic impacts from a projectile fired with a light gas gun were found to be the most accurate method for simulating in-service FOD. However, special expertise is required to produce and control damage parameters. Impact projectiles, such as spheres and cubes, and their impact velocities can be adjusted to investigate a specific damage type. Ballistic simulated FOD damage typically involves enough variation in nominally identical damage sites to affect post-damage mechanical testing. Gas guns are expensive to operate and damage generation is very time consuming, but the FOD sites created are the closest to real FOD damage than those created by any other simulation methods. Boyce et al. (2001) and Ruschau et al. (2003) found that low strain rates quasi-static indentation resulted in different fatigue results compared to specimens ballistically indented. They concluded that the residual stresses introduced by quasi-static indentation and ballistic impact are different. Thus limits the quasi-static indention method for the purpose of simulating FOD.

Most of the published research studies on FOD have used a gas gun to create FOD damage with spherical shaped projectiles such as glass beads (Thompson et al., 2001; Martinez at al., 2002; Ruschau et al., 2001) or steel pallets (e.g. Nicholas et al., 1980; Peters and Ritchie, 2000; Bache et al., 2002; 2003). The glass beads should simulate

the effects of shattering or chipping of stones upon impact. Spherical projectiles result in rounded indents. Recent studies considered sharp V-notches and tears as more detrimental than rounded damage due to the higher stress concentration (K_t), and these are considered more representative of the worst-case of FOD in-service. Early studies on V-notches were carried out by Kaufman (1958) using a chisel-tip attached to a pendulum. Following this approach more work was carried out at Oxford University (Nowell et al., 2003a; 2003b; Oakley and Nowell, 2007; Duo et al., 2007) and at the University of Portsmouth (Ding et al., 2007a; 2007b; Hall et al., 2008) by using a gas gun to fire hardened steel cubes as projectiles. This latter method of simulating FOD damage was the method used in the present study.

2.4 Effects of FOD on fatigue behaviour

Crack initiation due to FOD was investigated in numerous studies and it seems to depend on damage features associated with the impact method, projectile shape and impact velocity. Nicholas et al. (1980) investigated the impact damage on leading edges in relation to impact speed, using small spheres over a range of velocities of 120 to 490m/s. With increasing impact velocity, the impact produced a dent, a dent including a sharp tear or a perforation. A dent including a sharp notch was found to be most detrimental on fatigue life. Thompson et al. (2001) observed similar results that irregular shaped notches as a result of tears and material removal were most detrimental to fatigue life. For double-edged specimens with a dent and tear on one edge, and a notch on the other from spherical ballistic impacts, Bache et al. (2002; 2003) and Martinez et al. (2002) found that the crack typically started at the root of the notch, specifically at the root of the larger notch. Similarly, Ruschau et al. (2001) observed, for two nominally identical notches, the marginally deeper notch initiates a crack earlier.

For 30º angled spherical ballistic impacts on specimens with tapered edges, Ruschau et al. (2001) observed that fatigue cracks often initiate at impact-induced tears at the edge of the notch, rather than at the notch root. However, Martinez et al. (2002)

found that for 30º impacts, although surface damage features produced sharp edges and micro-folds, sites favourable for crack initiation, cracks initiated near the centre of the notch nevertheless.

Meyers and Pak (1985) observed the formation of shear-bands produced by the impact of a projectile on titanium. Adiabatic shear-bands (ASB)[2-1] were formed during the high rate deformation, effectively melting and re-solidifying the metal and resulting in a different grain structure. It was showed that shear-bands involve high density of dislocations and deformation twins. Murr et al. (2009) analysed ASB in Ti-6Al-4V by microindentation and transmission electron microscopy (TEM), and found that the length of ASB increased with the increase of the impact velocity, together with cracks nucleating and propagating within these ABSs. Birkbeck et al. (2002) also observed that, for 0º and 30º FOD impacts on tapered specimens, shear-bands were responsible for the initiation of the fatigue failures. Contrary to the above, Roder et al. (1999), Peters et al. (2000) and Martinez et al. (2002) found that the fatigue cracks did not initiate from the shear-bands. They proposed that the lack of influence of the shear-bands on crack initiation was due to the parallel orientation of these bands with the loading direction. Ruschau et al. (2001) observed shear-bands formed parallel to the impact damage (ballistic spherical damage) and found crack-like features formed along these shear-bands; but noted that these features were orientated parallel to the applied loading and therefore had little influence on crack initiation.

Ritchie et al. (1999a; 1999b) investigated crack initiation in relation to impact velocity by fatigue testing rectangular gauge sectioned tensile specimens subjected to spherical ballistic impacts of 0º. For samples impacted at 200m/s cracks initiated near the bottom of the crater; while for samples impacted at 300m/s crack initiation occurred at the crater rim. The studies of Roder et al. (1999), Peters and Ritchie (2000) and Peters et al. (2000) showed that higher velocities introduce tensile residual stresses at the crater rim which promotes cack initiation; while crack initiation for lower velocities is driven by the notch concentration effect. Subsequent

[2-1] The term 'adiabatic' indicates that the formation of the shear bands is so rapid that there is no heat exchanged.

investigations by Peters et al. (2002) and Peters and Ritchie (2000; 2001a; 2001b) also showed crack initiation at the crater rim, away from the impact indentation for low applied stress ranges. Chen and Hutchinson (2001; 2002) validated these preferred fatigue crack initiation sites by using the finite element method to simulate the impact, and found tensile stresses at regions around the crater rim, at the base of the notch and below the surface of the notch.

Studies using a cubical projectile within a gas gun to simulate FOD on tapered specimens were carried out by Nowell et al. (2003a; 2003b) and Hall et al. (2008), who reported that all specimens failed by propagation of a fatigue crack from the impact damage site. Ding et al. (2007a; 2007b) also investigated V-notches on plate specimens and described the characteristics associated with FOD damage were the appearance of folds, small sharp notches and small cracks in the FOD notch. The microcracks formed as a result of impact were found to be preferred sites for subsequent crack propagation. Multi-crack initiation sites at the root of the FOD indent were observed. Hall et al. (2008) found, by comparing specimens with and without stress relief, that the compressive residual stresses at the bottom of the indent inhibit crack propagation from that region.

Typical angles of incidence between the ingested particle and a rotating blade in an aero engine are dependent on radial location, rotational speed and the forward velocity of the engine, ranging between 0º and 60º (Nicholas, 2006). Ritchie et al. (1999a; 1999b) found, for 0º impacts by small spheres against a flat surface, fatigue life was reduced by many magnitudes compared to un-impacted samples. Computer simulations of this case by Chen and Hutchinson (2001) predicted deficits up to 60%. Ruschau et al. (2001) investigated spherical 0º impacts on specimen edges, found fatigue strength reduction between 10 and 40%. Considering different impact angles for spherical ballistic impacts, Ruschau et al. (2001; 2003) and Martinez et al. (2002) found the greatest loss in fatigue strength at an impact angle of 30º, in contrast to little reduction in fatigue life for 0º impacts. Ruschau et al. (2001) showed that, for specimens with two different leading edge (LE) radii (0.127mm and 0.38mm), the fatigue strengths were similar for both specimens despite deeper impact damage

occurred in the thinner leading edge. Martinez et al. (2002), however, observed higher fatigue strength for specimens with smaller LE radius.

For cubical ballistic impacts, Nowell et al. (2003a) investigated the effects of impact angle on the fatigue strength, considering 20, 50 and 80 degrees. Higher fatigue strength was recorded for 20º impacts compared to that obtained following 50º and 80º impacts. It was argued that 20º impacts were closer to head-on (0º) therefore compressive stresses were more likely to be introduced behind the notch. The same study investigated the influence of the leading edge geometry on fatigue strength by using LE radii of 0.25, 0.51 and 0.89mm. Little difference between the results for the two smaller radii was noted. A high scatter band for the larger radius was observed, partly due to the difficulties in measuring the notch depth.

The residual stresses due to FOD impacts also affect the fatigue behaviour. Comparing two sets of specimens (spherical ballistic impact 30º on a tapered edge), Thompson et al. (2001) found that the stress relieved specimens showed higher fatigue strength than that in the as-FODed specimens, indicating that residual stresses due to the FOD impact contribute to reduce the fatigue strength. Ruschau et al. (2003) and Nicholas et al. (2003), however, found for similar specimens and impact conditions, reduced fatigue life for stress-relieved specimens, indicating probably the beneficial effect of compressive residual stresses.

Nowell et al. (2003b), Duo et al. (2007) and Hall et al. (2008) studied ballistic cubical impacts on blade-like specimens and found by finite element simulation a zone of residual compression ahead of the FOD notch, with a depth of about 100μm. It was concluded that a crack growing away from the notch would experience a compressive residual stress field in the region where crack arrest may take place. Ding et al. (2007a) also studied V-notches (cubical ballistic impacts) and observed qualitative differences in crack shape and fatigue lives for stress relieved specimens compared to as-FODed specimens, indicating that both geometry and residual stress play an important role in the fatigue behaviour and must be considered in the prediction of fatigue crack growth. Ding et al. (2007b) simulated the FOD impact by finite element analysis and found compressive residual stresses below the bottom of

the impact site and tensile immediately outside the damage rim. Hall et al. (2008) investigated ballistic cubical 0º FOD impacts and recorded for the same loading conditions a much lower fatigue life of the stress relieved FOD specimen compared to the unrelieved FOD specimens, concluding that residual compressive stresses, predominantly at the bottom of the FOD indent, inhibit crack propagation from that region. Further, the stress intensity factor was modified considering residual stresses and correlated with the FCG rates. Significant differences in the early crack growth behaviour were observed between the as-FODed and the stress relieved specimens. For all loading conditions (LCF, HCF, LCF+HCF) reduced values of ΔK, together with delayed early crack growth due to the presence of compressive residual stresses, were observed. Similar crack growth rates and K values were recorded for stress relieved and as FODed specimens away from the influence of the FOD. The fatigue lives under LCF+HCF loading condition was shorter than those under LCF or HCF loading conditions.

Oakley and Nowell (2007) considered the influence of residual stresses near the root of the FOD V-notch on the R-ratio, and found that the predicted fatigue strength underestimated the experimental results when residual stresses were not taken into account. It was argued that for high-applied R-ratios, residual compressive stresses merely modify the local R-ratio of a propagating crack and have relatively little effect on the crack driving force; whereas for low applied R-ratio, the crack driving force K will be reduced due to the compressive residual stresses. The calculated effective R ratio (residual stress corrected) was calculated for each crack length and the values decreased from a nominal R-ratio of 0.8 to 0. Similarly, Mall et al. (2001) simulated a quasi-static indentation by using the FE method and obtained a residual stress distribution. By calculating the local R-ratio it was found that tensile stresses near the damage site increased the applied R-ratios from R=0.1 and 0.5 to between R=0.71 and 0.77.

However, during subsequent fatigue loading post FOD, Boyce et al. (2003) reported that the initial residual stresses associated with FOD might not sustain due to stress relaxation. After Holzapfel et al. (1998), relaxation occurs when the sum of the load and the residual stress exceeds the yield stress of the material. The magnitude of

residual stress relaxation is dependent on the applied load level and FOD-induced stress concentration. Relaxation is associated with the re-ordering of dislocations and the occurrence of cyclic softening and can further increase upon the formation and growth of a fatigue crack due to the stress concentration effect[2-2]. Boyce et al. (2003) observed, for spherical FOD impacts on Ti-6Al-4V, little residual stress relaxation at an applied stress of $0.35\sigma_Y$, σ_Y is the yield stress; while significant stress relaxation occurred at $0.54\sigma_Y$. Peters et al. (2000) noted a considerable amount of residual stress relaxation at the base of a ballistic spherical FOD impact during the first few fatigue load cycles. Boyce et al. (2001) found a 40% reduction of residual stresses caused by a quasi-static indentation after the first cycle.

2.5 Laser Shock Peening and its effects on fatigue behaviour

The principal of a pulsed laser beam to generate shock waves was first recognised and explored in the early 1960's. Laser shock peening (LSP) was invented in the 1970's as a method to enhance fatigue properties of metals (Monstross et al., 2002; Zhang, 2009b). Until now, the technique has not been used in production on commercial parts for leading edges.

The process of laser shock peeing is shown in Figure 2-1 and the following description of the process is based on (Monstross et al., 2002). A high-energy laser pulse (1-100J) passes through the transparent overlay (water), vaporizes an absorbing layer (black paint), and rapidly forms a plasma that absorbs the rest of the laser pulse. The hydrodynamic expansion of the plasma creates a short duration pressure pulse with high amplitude, which propagates partly as a shockwave through the work piece. When the pressure of the shockwave exceeds the yield strength of the material, plastic deformation occurs, resulting in residual compressive stresses below the surface. This deep level of residual stresses up to 1mm is much greater than that achievable with shot peening (Monstross, 2002; Ruschau et al., 1999a; 1999b), and it provides a barrier to crack initiation and crack

[2-2] Residual stress relaxation is further discussed in Chapter 2.5.

growth and a damage tolerance in situations of corrosion, fretting or FOD. Processing parameters such as laser power + power density = spot size, pulse duration, absorbent coating, transparent overlay and multiple laser shocks (overlapping) are adjustable to meet the goals in performance, cost and efficiency (Monstross et al., 2002; Liu, 2008).

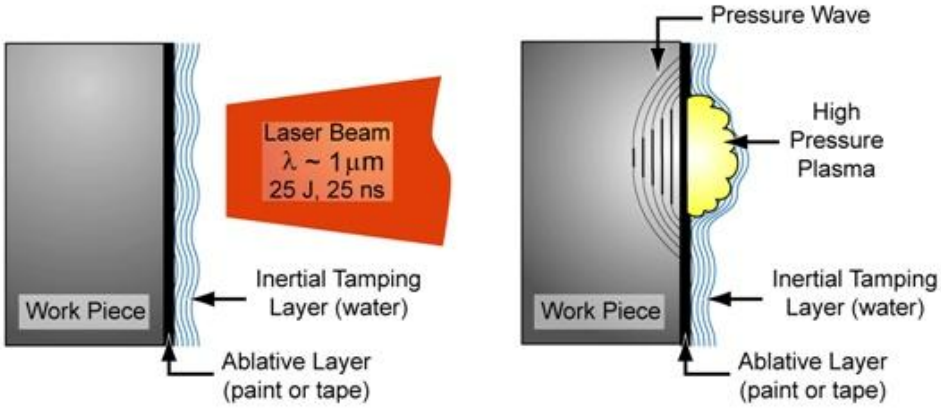

Figure 2-1 Laser shock peening process (after Luong and Hill, 2008; 2010).

Residual stress refers to a stress distribution which is present in an unloaded component or structure. The structure contains a balance of tensile and compressive residual stress within the body to remain in equilibrium. The occurrence and magnitude of the stress are a function of the component size and the process parameters used. The X-ray diffraction technique is a non-destructive method for determining residual stresses and is capable of high spatial resolution (Prevey, 1990). This evaluation method is commonly used to determine residual surface stresses present in a material and is considered to be the most accurate and best developed technique for this application (Prevey, 1990; Cheong et al 2004; Greenacre et al., 2005). X-ray diffraction measurements were carried out by our project partner, the University of Manchester. Several studies used the x-ray diffraction method to map the residual stresses involved with a FOD impact and comparison with FE simulated FOD residual stress distributions. Boyce et al. (2001; 2003) found a good correlation between the two techniques for indentation by a sphere on a flat surface; whereas

Frankel et al. (2006) and Duo et al. (2007) mapped residual stresses around the vicinity of V-notches of cubical impacts.

The residual stresses introduced by LSP have a significant influence on the material properties, crack initiation and fatigue behaviour. Nalla et al. (2003) and Zhang et al. (2009b) investigated the microstrucure of LSPed Ti-6Al-4V by nanoindentation and found that LSP increased the hardness at the surface up to 15% for a single shot and 24% for two successive laser shocks. Possible improvement of fracture toughness was also assumed. Ruschau et al. (1999a; 1999b) showed that LSP caused microstructural changes at the sub-grain level in Ti-6Al-4V. A very high dislocation density within the grains of the LSP treated region, compared to an extremely low dislocation density outside the LSP region, was also found. Swalla and Neu (2006) used the electron backscatter diffraction (EBSD) technique to quantify the evolution of strain-induced microstructural changes due to deformation in the near-surface layers in LSPed Ti-6Al-4V, and found shifted misorientation angles due to large plastic deformation. These areas were referred to as micro-texture and were found to be susceptible for crack nucleation (Swalla and Neu, 2006).

Almer et al (2000) used X-ray diffraction and FE analysis to predict fatigue crack initiation in the presence of residual stresses, and observed that multiple crack initiation occurred at sites where the compressive residual stresses were found to be small. Multiple cracks initiated near the notch and linked-up to form the main fatigue crack responsible for failure. Liu (2008) investigated fatigue of LSPed aluminium AA7050 specimens and noted that, generally, fatigue cracks initiated at subsurface locations, but also sporadically occurred at the surface from machining marks. Greenacre et al. (2005) studied the crack initiation behaviour of LSPed materials and found that crack initiation depended on the applied stress. Crack initiation usually takes place near surface for high mean stresses; whereas subsurface crack initiation occurs at low mean stresses. Liu (2008) also noted that, for internal cracked fracture surfaces of LSPed Al specimens, the fracture profile was markedly 'stepped' as a result of at least two connected fatigue fracture planes, indicating multiple crack initiation and link-up of these cracks.

The substantial fatigue resistance improvement resulting from surface treatments[2-3] such as LSP is attributed to the high levels of compressive residual stresses, which reduce the mean stress in a fatigue cycle (McClung, 2006). The mean stress has a significant influence on fatigue crack growth, and a higher level of mean stress generally produces higher crack growth rates (James et al., 2004). The effective stress intensity factor that controls the fatigue crack growth in LSPed specimens may be lower than the unpeened condition and may result in a reduction in the crack propagation rates (Ruschau et al., 1999a; 1999b; Hatamleh, 2009). In addition, compressive residual stresses increase the fatigue crack closure effects primarily by plasticity-induced crack closure, decreasing the applied stress intensity and reducing the crack growth rates, as discussed in the previous Chapter 2.1 (Elber, 1970; Hatamleh, 2009; Ruschau et al., 1999a; 1999b; Beghini et al., 1994; Nelson, 1982).

Various studies on Al alloy showed the beneficial effects of LSP on fatigue crack growth and fatigue life. Peyre et al. (1996) investigated HCF behaviour of different Al alloys and observed an enhanced fatigue performance of LSPed materials compared to SPed materials, and the fatigue performance improvements mainly occurred during the crack initiation stage. Luong and Hill (2008; 2010) quantified the enhanced fatigue life of LSPed Al specimens by a factor of 5.6 and a fatigue strength improvement at 10^5 by 38% compared to as machined samples. Rubio-Gonzalez et al. (2004) compared fatigue crack growth data under R=0.1 for Al specimens with and without LSP, and found reduced fatigue crack growth rates and increased fracture toughness for LSPed specimens. Further, Rubio-Gonzalez et al. (2011) observed reduced fatigue crack growth for LSPed 2205 duplex stainless steel, but no effects of the LSP on the microstructure or micro-hardness. Liu (2008) also studied LSPed Al alloy, and recorded a 3-4 times increased fatigue life compared to as-machined specimens. Investigations of different applied stress levels revealed that the beneficial effects of compressive residual stresses induced by LSP are more

[2-3] Surface treatments including glass bead peening (GBP) (e.g. Reed and Viens, 1960; Dorr and Wagner, 1999), deep rolling (DR) (e.g. Nalla et al., 2003), shot peening (SP) (e.g. Wagner, 1999) and low plasticity burnishing (LPB) (e.g. Prevey et al., 2001) vary in their specific mechanics and mechanism but share the common characteristic that localised plastic deformation of arbitrary engineering surfaces is used to induce compressive residual stresses near the surfaces.

significant at a lower maximum applied stress (Ruschau et al., 1999a; 1999b). LSP is more effective in delaying crack growth and enhancing fatigue life at low applied stress and less effective at higher applied stresses because the deformation during the applied load may overcome the compressive residual stresses (Liu, 2008). However, it was shown that the fatigue life was reduced if the laser power density was too high, due to the formation of internal cracking and surface damage caused by the laser shock wave (Liu, 2008).

A research group at Lambda Research (Cincinnati) (Prevey et al., 2001; 2002; 2003; 2004a; 2004b; Jayaraman et al., 2005) studied the effects of low plasticity burnishing (LPB, similar to LSP) on FOD tolerance benefits in Ti-6Al-4V blade and vane edged specimens under HCF conditions. Electrical discharging machined (EDM) V-notches were used and significantly enhanced fatigue performance was noted. In the HCF regime a tenfold damage tolerance increase was obtained (from 0.05mm to at least 0.5mm), together with doubled fatigue strength recorded from LPBed vanes compared to untreated ones. In the LCF regime, under low R ratios (R=0.1 and R=-1), even higher FOD damage tolerance (up to 1.5mm) was observed.

Ruschau et al. (1999a; 1999b) investigated the crack growth behaviour of notched, LSPed Ti-6Al-4V aerofoil specimens under low (R=0.1) and high (R=0.8) load ratios. Delayed FCG rates were recorded when the cyclic stress was below the residual stress field created by the LSP process. For HCF conditions (R=0.8) little improvement in FCGR was found; whereas for LCF conditions (R=0.1) significant improvement in crack growth rates, nearly three orders in magnitude slower for the LSPed material compared to untreated material, was observed. It was noted that differences in the crack behaviour due to LSP could be accounted for by using closure models to achieve a closure corrected effective stress intensity range. Nalla et al. (2003) compared fatigue results of LSPed and deep rolled (DR) Ti-6Al-4V to untreated material and found that both surface treatments lower the plastic strain amplitude throughout the majority of the lifetime, resulting in an enhanced fatigue life. Hardness tests showed a significantly higher work hardening near the surface of DR materials compared to LSPed materials. Further, considerably less residual stress

relaxation due to fatigue cycle for LSPed materials was recorded compared to DR materials, especially at room temperature.

For cyclic bending, Voehringer et al. (1984) found only limited residual stress relaxation during continued fatigue after the first cycle for shot peened specimens. Prevey et al. (2004a; 2004b) observed mild relaxation between 10 and 30% of the residual stresses due to LPB after two fully reversed stress amplitudes. Cheong et al. (2004) carried out LCF tests at R=0.05 on disk bore featured specimens of Ti-6Al-4V, observed about 20% reduction in surface residual stresses from shot peening (SP), and little or no change in LPB-induced residual stresses, even the latter were initially about one third of those generated by SP.

Generally, residual stress relaxation can occur even when the applied mechanical loads do not cause any macroscopic plastic deformation. Residual stress relaxation is more pronounced under large cyclic stresses or strains. Relaxation is negligible at the lowest and extensive at the highest fatigue stress amplitudes (McClung, 2006). Several studies found that, under reversed bending fatigue, significant relaxation of the compressive surface residuals stresses after the first cycle, followed by a more gradual relaxation with subsequent cycles (Taira and Murakami, 1960; Wick et al., 2000). The large change in the first cycle is apparently due to the static effect, when the superposition of residual stress and applied stress of the same sign exceed the yield condition (Holzapfel et al., 1998). Subsequent relaxation often decreases linearly with the logarithm of the cycles during this second stage of relaxation (McClung, 2006). The rate and extent of cyclic relaxation were observed to depend on various parameters, including peening intensity and coverage (Torres and Voorwald, 2002), peening temperature (Wick et al., 2000), the original hardness of the material (Torres and Voorwald, 2002), and the loading type (McClung, 2006). The most common model to predict cyclic relaxation of peened materials is the linearly decrease with the logarithm of fatigue cycles after the initial relaxation (e.g. Holzapfel et al., 1998; Bergstreom and Ericsson, 1986). Lu et al. (1988) developed a finite element model based on simplified inelastic analysis, employing a group of internal parameters that characterise local inelastic mechanism to predict the relaxation of residual stresses. Relaxation due to thermal effects is not considered in

this thesis, as all experiments were carried out under ambient temperature. An excellent overview about thermal residual stress relaxation is presented by McClung (2006).

2.6 The effects of residual stress on SIF

When a cyclic load is applied to a part with residual stresses present, a superposition of the residual stresses with the applied stress normally applies (Nelson, 1982). The stress amplitude will not change as the residual stress affects the maximum and minimum stress at the same time. The mean stress will change according to the nature of the residual stress. If the residual stress is compressive, the mean stress will be reduced which is favourable for fatigue life enhancement and vice versa for tensile residual stress. The evaluation of the crack tip stress intensity factor (SIF) must consider the influence of residual stresses in these cases for damage tolerance analysis. A residual SIF (K_{res}) is required to estimate the fatigue crack growth rates and the fatigue life. If the crack is subjected to a residual (K_{res}) and an applied (K_{app}) stress intensity factor, the resultant or effective SIF (K_{eff}) can be calculated as the sum of the SIF given by the two types of SIF:

$$K_{eff} = K_{app} + K_{res} \tag{2-6}$$

Evaluation of a SIF in a residual stress field has been approached by using the weight function method (e.g. Bao et al., 2010; Pouget and Reynolds, 2008), modified J-integral (e.g. Lei et al., 2000; Servetti and Zhang, 2009) or crack compliance method (e.g. Schindler et al., 1997; Prime, 1999). The latter method was proposed by Elber (1971) and is based on the crack closure concept (Nelson, 1982). The use of the weight function method (WFM) in fracture mechanics was first proposed by Bueckner (1970) and successively generalised by Rice (1972). For application of the WFM the knowledge of the stresses acting in the uncracked body is required. Therefore the redistribution produced by the crack needs not to be considered and

calculations can be based on residual stress fields measured for the uncracked body (Beghini et al., 1997). Hence, the WFM allows calculating the SIF due to superposition of residual stresses with stresses due to external load, also including the effects of possible crack closure phenomena (Beghini et al., 1997).

Due to the availability of an experimentally measured residual stress field, the application of the weight function and the finite element method to modify the effective crack driving force appears to be particularly suitable for this study. Considering a 2D body with an edge crack and under Mode I loading, the SIF can be calculated as

$$K_{res} = \int_0^a \sigma_{res}(x) \bullet m(x,a)dx \tag{2-7}$$

where $m_{(x,a)}$ is the weight function, depending on the cracked body geometry, and σ_{res} is the nominal residual stress distribution. Standard solutions for weight functions are provided in the literature (Wu and Carlsson, 1991; Tada et al., 1973); or can be obtained by numerical techniques, but the latter involves high computational effort (Beghini et al., 1997). Once the residual maximum and minimum SIFs are calculated, an effective SIF range and R-ratio **(**ΔK_{eff}, R_{eff}) can be calculated.

The weight function was successfully used to modify K_{eff} and to calculate K_{res} considering residual stresses from welding (e.g. Bao et al., 2010; Pouget and Reynolds, 2008) as well as for residual stresses for welding+laser shock peening (e.g. Hatamleh et al., 2009) and for LSPed material (e.g. Reji et al., 2001; Ren et al., 2009; Zhang et al., 2009a). However, this approach has not been used so far to modify a SIF considering residual stresses due to FOD impacts alone or in combination with a surface treatment. Oakley and Nowell (2007) modified the SIF at the notch tip of a FOD notch using the dislocation density method and added it to the applied SIF using the principle of superposition. Hall et al. (2008) modified the SIF considering residual stresses resulting from a FOD impact by using the finite element method. The latter method will be explained in the next chapter.

2.7 Finite element analysis in Fracture Mechanics

The analysis of fatigue crack driving force using the linear elastic fracture mechanics (LEFM) theory is based on the stress intensity factor or the elastic J-integral. Under Mode I loading conditions, the J-integral can be correlated to K_I. The FE method has been used to modify SIF in welded components, considering the residual stresses (Liljedahl et al., 2010; Servetti and Zhang, 2009; Bao et al., 2010), and FOD only (Hall et al., 2008). Hall et al (2008) introduced the longitudinal residual stress component along the crack path in a FE model to obtain the effective SIF and correlated fatigue crack growth data with the corrected SIF considering the residual stress due to FOD.

This study utilises results from the previous studies and incorporates the residual stresses caused by both LSP and FOD in the estimation of SIF. The finite element code ABAQUS was used. Initial stress facility in the ABAQUS code is one method that is able to apply residual stresses as an initial condition prior to the analysis. This technique was used to modify a J-integral (Lei et al., 2000; Servetti and Zhang, 2009). The initial stress can be applied by defining the relevant stress components at each integration point of the model. These stresses must be self-equilibrating, which usually requires an equilibrium step after the residual stress is applied. Cook et al (2002) used the principle of superposition to apply the residual stress on the surface of a crack face by using ABAQUS DLOAD subroutine. Using this method the residual stresses do not need to be balanced.

2.8 References

Almer. J.D., Cohen, J.B., Moran, B., 2000. The effects of residual macrostresses and microstresses on fatigue crack initiation. Materials Science and Engineering A 284, 268-279.

Anderson, J.C., Leaver, K.D., Rawlings, R.D., Alexander, J.M., 1990. Materials Science, (4th edition), Chapman and Hall.

ASTM Standards, 1995. Standard Test Method for Measurement of Fatigue Crack Growth Rates. ASTM E647-95a, 557-593.

Bache, M.R., Evans, W.J., Voice W., 2002. The resistance to impact damage and subsequent response of two titanium alloys. Material Science and Engineering A 333, 287-294.

Bache, M.R., Bradshaw, C., Voice W., 2003. Characterisation of foreign object damage and fatigue strength in titanium based aerofoil alloys. Materials Science and Engineering A 354, 199-206.

Bao, R., Zhang, X., Yahaya, N.A., 2010. Evaluating stress intensity factors due to weld residual stresses by the weight function and finite element methods. Engineering Fracture Mechanics 77, 2550-2566.

Beevers, C.J., 1981. Some aspects of the influence of microstructure and environment on ΔK threshold. Fatigue Thresholds 1, EMAS, Warley, UK, 257-275.

Beghini, M., Bertini, L., Vitale, E., 1997. Weight functions applied to fatigue crack growth analysis. Fatigue & Fracture of Engineering Materials & Structures 20, 1093-1104.

Beghini, M., Bertini, L., Vitale, E., 1994. Fatigue crack growth in residual stress fields: experimental results and modelling. Fatigue & Fracture of Engineering Materials & Structures 17, 433-444.

Bergstrom, J., Ericsson, T., 1986. Relaxation of shot peening induced compressive stress during fatigue of notched steel samples. Surface Engineering 2, 115–120.

Birbeck, J.C., Eylon, D., Nicholas, T., Thompson, S.R., 2002. Effects of FOD on fatigue crack initiation of ballistically impacted Ti-6Al-4V simulated engine blades. Proceedings: 7th National Turbine Engine High Cycle Fatigue Conference, Palm Beach Gardens, FL.

Boyce, B.L., Chen, X., Hutchinson, J.W., Ritchie, R.O., 2001. The residual stress state due to a spherical hard-body impact. Mechanics of Materials 33, 441-454.

Boyce, B.L., Chen, X., Peters, R.O., Hutchinson, J.W., Ritchie, R.O., 2003. Mechanical relaxation of localised residual stresses associated with foreign object damage. Materials Science and Engineering A 349, 48-58.

Broek, D. 1986. Elementary Engineering Fracture Mechanics. Martinus Nijhoff Publishers.

Bueckner, H.F., 1970. A novel principle for the computation of stress intensity factors. 2. Angenwandte Mathematik und Mechanik 50, 529-546.

Byrne, J., Hall, R.F., Powell, B.E., 2003. Influence of LCF overloads on combined HCF/LCF crack growth. International Journal of Fatigue 25, 27–834.

Campbell, J.P., Ritchie, R.O., 2000. Mixed-mode, high-cycle fatigue-crack growth thresholds in Ti–6Al–4V: I. A comparison of large- and short-crack behaviour. Engineering Fracture Mechanics 67, 209-227.

Chen, X., Hutchinson, J.W., 2001. Foreign object damage and fatigue crack threshold: Cracking outside shallow indents. International Journal of Fracture 107, 31-51.

Chen, X., Hutchinson, J.W., 2002. Particle impact on metal substrates with application to foreign object damage to aircraft engines. Journal of the Mechanics and Physics of Solids 50, 2669-2690.

Cheong, W., Zhuang, W., Zhang, L., 2004. Study of residual stress relaxation using x-ray diffraction. Key Engineering Materials 274–276, 871–876.

Cook, G., Timbrell, C.M, Wiehahn, M., 2002. Using ABAQUS to analysis fatigue crack growth under the combined influence of residual stress and cyclic external load, UK ABAQUS User GROUP Conference.

Cowles, B.A., 1996. High cycle fatigue in aircraft gas turbines – an industry perspective. International Journal of Fracture 80, 147-163.

Ding, J., Hall, R.F., Byrne, J., Tong, J., 2007a. Fatigue crack growth from foreign object damage under combined low and high cycle loading, Part I: experimental studies. International Journal of Fatigue 29, 1339–1349.

Ding, J., Hall, R.F., Byrne J., Tong, J., 2007b. Fatigue crack growth from foreign object damage under combined low and high cycle loading. Part II: A two-parameter predictive approach. International Journal of Fatigue 29, 1350-1358.

Dorr, T., Wagner, L., 1999. Fatigue response of various titanium alloys to shot peening. In: Surface Treatment IV: Computer Methods and Experimental Measurements. Proceedings of the 4th International Conference on Computer Methods and Experimental Measurements for Surface Treatment Effects, Assisi, Italy, 349–357.

Duo, P., Liu, J., Dini, D., Golshan, M., Korunsky, A.M., 2007. Evaluation and analyisis of residual stresses due to foreign object damage. Mechanics of Materials 39, 199-211.

Elber, W., 1970. fatigue crack closure under cyclic tension. Engineering Fracture Mechanics 2, 37-45.

Elber, W., 1971. The significance of fatigue crack closure. Damage Tolerance in Aircraft Structures. ASTM STP 486, 230–242.

Endo, K., Komai, K., Matsuda, Y., 1969. Effects of stress history and corrosive environments on fatigue crack propagation. Memo of Fracture Engineering 31, 25-43.

ENSIP 1999, Engine Structural Integrity Program (ENSIP), Department of Defense Handbook, Downloaded from http://www.everyspec.com on 2011-02-17T10:20:56.

Erdogan, F., 2000. Fracture Mechanics. International Journal of Solids and Structure 37, 171-183.

Forsyth, P.J.E., 1963. Fatigue damage and crack growth in aluminium alloys. Acta Metallurgica. 703-715.

Frankel, P., Ding, J., Preuss, M., Byrne, J., Withers, P.J., 2006. Residual Stress Analysis Around Foreign Object Damage Using Synchrotron Diffraction. Materials Science Forum 524 - 525, 291-296.

Greenacre, P., Schofield, J., McElhone, M., Rugg, D., Lawson, M., 2005. Measurement and understanding of the level and effect of residual stresses induced by the laser shock peening process. In Evaluation, Control and Prevention of High Cycle Fatigue in Gas Turbine Engines for Land, Sea and Air Vehicles, Meeting Proceedings RTO-MP-AVT-121, paper 35, 35-1 - 35-14.

Haake, F.K., Salivar, G.C., Hindle, E.H., Fischer, J.W., Annis, C.G., 1989. Threshold Fatigue Crack Growth Behaviour, United States Air Force Technical Report, WRDC-TR-89-4085, Wright-Patterson AFB, OH.

Hall, R., Byrne J., Zhao, T., Tong, J., 2008. Influence of foreign object damage on fatigue crack growth of gas turbine aerofoils under complex loading conditions. Fatigue & Fracture of Engineering Materials & Structures 31, 386-397.

Hall, R.F., Powell, B.E., 1997. The growth of corner cracks by fatigue. International Journal of Fatigue 19, 429-435.

Haritos, G.K., Nicholas, T., Lanning, D.B., 1999. Notch size effects in HCF behaviour of Ti–6Al–4V. International Journal of Fatigue, 21, 643-652.

Hatamleh, O., Hill, M., Forth, S., Garcia, D., 2009. Fatigue crack growth performance of peened friction stir welded 2195 aluminum alloy joints at elevated cryogenic temperatures, Material Science and Engineering A 519, 61-69.

Hatamleh, O., 2009. A comprehensive investigation on the effects of laser and shot peening on fatigue crack growth in friction stir welded AA 2195 joints. International Journal of Fatigue 31, 974-988.

Hawkyard, M., 1997. The fatigue crack growth resitance of Ti-6Al-4V. PhD thesis, University of Portsmouth.

Hawkyard, M., Powell, B.E., Hussey, I., Grabowski, L., 1996. Fatigue crack growth under the conjoint action of major and minor stress cycles. Fatigue & Fracture of Engineering Materials and Structures 19, 217–227.

Holzapfel, H., Schulze, V., Vohringer, O., Macherauch, E., 1998. Residual stress relaxation in an AISI 4140 steel due to quasistatic and cyclic loading at higher temperatures. Material Science and Engineering A248, 9–18.

James, M.N., Hughes, D.J., Hattingh, D.G., Bradley, G.R., Mills, G., Webster, P.J., 2004. Synchrotron diffraction measurment of residual stresses in fricton stir welded 5383-H321 aluminium butt joints and their modification by fatigue cycling. Fatigue & Fracture of Engineering Materials & Structures 27, 187-202.

Jayaraman, N., Prevey, P.S., Ravindranath, R., 2005. Improved damage tolerance of Ti-6Al-4V aero engine blades and vanes using residual compression by design. NATO RSV, Granada, Spain.

Kaufman, A., 1958. Method for determining the need to rework of replace compressor rotor blades damaged by foreign objects, technical note 4324, Lewis Flight Propulsion Laboratory, Cleveland, OH, National Advisory Committee for Aeronautics Washington.

Kaufman, A., Meyer, A.J. Jr., 1956. Investigation of the effect of impact damage on fatigue strength of jet-engine compressor rotor blades, Technical note 3275, Lewis Flight Propulsion Laboratory, Cleveland, OH, National Advisory Committee for Aeronautics Washington.

Lanning, D.B., Haritos, G.K., Nicholas, T., 1999. Influence of stress state on high cycle fatigue of notched Ti-6Al-4V specimens. International Journal of Fatigue 21, 87-95.

Larson, J.M., Worth, B.D., Annis, C.G. Jr., Haake, F.K., 1996. Anassessment of the role of near-threshold crack growth in high-cycle-fatigue life prediction of aerospace titanium alloys under turbine engine spectra. International Journal of Fracture 80, 237-255.

Lei, Y., O'Dwod, Webster, G.A., 2000. Fracture analysis of a crack in a residual stress field. International Journal of Fracture 106, 195-216.

Liljedahl, C.D.M., Zanellato, O., Fitzpatrick, M.E., Lin, J., Edwards, L., 2010. The effect of weld residual stresses and their re-distribution with crack growth during fatigue under constant amplitude loading. International Journal of Fatigue 32, 735-743.

Liu, Q., 2008. An effective life extension technology for 7xxx series aluminium alloys by laser shock peening. Australian Government, Department of Defence, Defence Science and Technology Organisation, DSTO-TR-2177.

Lu, J., Flavenot, J.F., Turbat, A., 1988. Prediction of residual stress relaxation during fatigue. In: Mechanical Relaxation of Residual Stresses, ASTM STP 993 (Edited by L. Mordfin). American Society for Testing and Materials, 75–90.

Luong, H., Hill, M.R., 2008. The effects of laser peening on high-cycle fatigue in 7085-T7651 aluminum alloy. Materials Science and Engineering A 477, 208-216.

Luong, H., Hill, M.R., 2010. The effects of laser peening and shot peening on high cycle fatigue in 7050-T7451 aluminum alloy. Materials Science and Engineering A 527, 699-707.

Mall, S., Hamrick, J.L, Nicholas, T., 2001. High cycle fatigue behaviour of Ti-6Al-4V with simulated foreign object damage. Mechanics of Materials 33, 679-692.

Martinez, C.M., Eylon, D., Nicholas, T., Thompson, S.R., Ruschau, J.J., Birkbeck, J., Porter, W.J., 2002. Effects of ballistic impact damage on fatigue crack initiation in Ti-6Al-4V simulated engine blades. Material Science and Engineering A325, 465–477.

McClung RC, 2006, A literature survey on the stability and significance of residual stresses during fatigue, Fatigue & Fracture of Engineering Materials & Structures 30, 173-205.

Meyers, M.A., Pak, H-R., 1985. Observation of an adiabatic shear band in titanium by high-voltage transmission electroscopy. Acta metall 34, 2493-2499.

Monstross, C.S., Wei, T., Ye, L., Clark, G., Mai, Y-W., 2002. Laser shock processing and its effects on microstructure and properties of metal alloys: a review. International Journal of Fatigue 24, 1021-1036.

Murr, L.E., Ramirez, A.C., Gaytan, S.M, Lopez, M.I., Martinez, E.Y., Hernandez, D.H., Martinez, E., 2009. Microstructure evolution associated with adiabatic shear bands and shear band failure in ballistic plug formation in Ti-6Al-4V targets. Material Science and Engineering A 516, 205-216.

Nalla, R.K., Altenberger, I., Noster, U., Liu, G.Y., Scholtes, B., Ritchie, R.O., 2003. On the influence of mechanical surface treatments - deep rooling and laser shock peening - on the fatigue bahaviour of Ti-6Al-4V at ambient and elevated temperatures, Materials Science and Engineering A 355, 216-230.

Nelson, D.V., 1982. Effects of residual stress on fatigue crack propagation, residual stress effects in fatigue, ASTM STP 776, American Society for Testing and Materials, 172-194.

Nicholas, T., 1999. Critical issues in high cycle fatigue. International Journal of Fatigue 21, 221-231.

Nicholas, T, Ruschau, J.J., Thompson, S.R., 2003. The influence of foreign object damage technique in fatigue strength of Ti airfoils. Proceedings: 8th National High Cycle Fatigue Conference, Monterey, CA.

Nicholas, T., 2006. High Cycle Fatigue a mechanics of materials perspective. Elsevier, 2006.

Nicholas, T., Barber, J.P., Bertke, R.S., 1980. Impact damge on titanium leading edges from small hard objects. Experimental Mechanics, Oct., 357-364.

Nowell, D., Duo, P., Stewart, I.F., 2003a. Prediction of fatigue performance in gas turbine blades after foreign object damage. International Journal of Fatigue 25, 963-969.

Nowell, D., Dini, D., Duo, P., 2003b. Stress analysis of V-notches with and without cracks, with application to foreign object damage. The Journal of Strain Analysis for Engineering Design 38, 429-441.

Oakley, S.Y., Nowell D., 2007. Prediction of the combined high- and low-cycle fatigue performance of gas turbine blades after foreign object damage. International Journal of Fatigue 29, 69-80.

Paris, P., Erdogan, F., 1963. A critical analysis of crack propagation laws. ASME, Journal of Basic Engineering, 528-534.

Pearson, S., 1975. Initiation of Fatigue cracks in commercial Aluminium alloys and subsequent propagation of very short cracks. Engineering Fracture Mechanics, 238-240.

Peters, J.O., Ritchie, R.O., 2000. Influence of Foreign-object damage on crack initiation and early crack growth during high cycle fatigue of Ti-6Al-4V. Engineering Fracture Mechanics, 193-207.

Peters, J.O., Roder, O., Boyce, B.L., Thompson, A.W., Ritchie, R.O., 2000, Role of foreign object damage on thresholds for high cycle fatigue in Ti-6Al-4V. Metallurgical and Materials Transactions A 31, 1571-1583.

Peters, J.O., Ritchie, R.O., 2001a. Foreign-object damage and high cycle fatigue of Ti-6Al-4V. Materials Science and Engineering A319-321, 597-601.

Peters, J.O., Ritchie, R.O., 2001b. Foreign-object damage and high cycle fatigue: role of microstructure in Ti-6Al-4V. International Journal of Fatigue 23, 413-421.

Peters, J.O., Boyce, B.L., Chen, X., McNaney, J.M., Hutchinson, J.W., Ritchie, R.O., 2002. On the application of the Kitagawa-Takahashi diagram to foreign object damage and high cycle fatigue. Engineering Fracture Mechanics 69, 1425-1446.

Peterson, R.E., 1974. Stress concentration factors, John Wiley & Sons.

Peyre, P., Fabbro, R., Merrien, P., Lieurade, H.P., 1996. Laser shock processing of aluminium alloys. Application to high cycle fatigue bahviour. Materials Science and Engineering A210, 102-113.

Pouget, G., Reynolds, A.P., 2008. Residual stress and microstructure effects on fatigue crack growth in AA2050 friction stir welds. International Journal of Fatigue 30, 463-472.

Powell, B.E., 1985. The influence of minor cycles on low cycle fatigue crack growth. PhD thesis, University of Portsmouth.

Powell, B.E., Duggan, T.V., 1986. Predicting the onset of high cycle fatigue damage: an engineering application for long crack fatigue threshold data, International Journal of Fatigue 8, 187–194.

Powell, B.E., Hawkyard, M., Grabowski, L., 1997. The growth of cracks in Ti–6Al–4V plate under combined high and low cycle fatigue. International Journal of Fatigue 19, 167–176.

Prevey, P.S., 1990. X-ray diffraction characterisation of residual stresses produced by shot peening. In Niku-Lari, A. (ed.). Shot Peening Theory and Application, IITT-International, Gournay-Sur-marne, France, Web site: htttp://www.lambda-research.com/2002.pdf.

Prevey, P.S., Shepard, M.J., Smith, P.R., 2001. The effect of low plasticity burnishing (LPB) on the fatigue HCF performance and FOD resistance of Ti-6Al-4V. Proceedings: 6th National Turbine Engine High Cycle Fatigue Conference, Jacksonville, Fl.

Prevey, P.S., Hornbach, D.J., Cammett, J.T., Ravindranath, R., 2002. Damage tolerance improvement of TI-6-4 fan blades with low plasticity burnishing. 6th Joint FAA/DoD/NASA Aging Aircraft Conference.

Prevey, P.S., Hornbach, D.J., Ravindranath, R., Cammett, J.T., 2003. Application of low plasticity burnishing to improve damage tolerance of a Ti-6Al-4V first stage fan blade. Proceedings 44th AIAA/ASME/ASCE/AHS Structures, Structural Dynamics & Materials Conf., Norfolk, VA.

Prevey, P.S., Jayaraman, N., Ravindranath, R., 2004a. HCFperformance and FOD tolerance improvement in Ti-6Al-4V vanes with LPB treatment. Proceedings 42nd AIAA Aerospace Science Meeting Reno, NV.

Prevey, P.S., Jayaraman, N., Shepard, M.J., 2004b. Improved HCF performance and FOD tolerance of surface treated Ti-6-2-4-6 compressor blades. 9th National Turbine Engine High Cycle Fatigue Conference, Pinehurst, NC.

Prime, M.B., 1999. Measuring residual stress and the resulting stress intensity factor in compact tension specimens. Fatigue & Fracture of Engineering Materials & Structures 22, 195–204.

Reed, E.C., Viens, J.A., 1960. The influence of surface residual stress on fatigue limit of titanium. Journal Engineering Ind., 76–78.

Reji, J., Larsen, J.M., Buchanan, D.J., Ashbaugh, N.E., 2001. Incorporating residual stresses in life prediction of turbine engine disks. Proceddings: RTO AVT "Ageing Mechanisms and Control: Part B – Monitoring and Management of Gas Turbine Fleets for Extended Life and Reduced Costs". Manchester, UK.

Ren, X.D., Zhang, Y.K., Zhou, J.Z., Lu, J.Z., Zhou, L.C., 2009. Influence of compressive stress on stress intensity factor of hole-edge crack by high strain rate laser shock processing. Materials and Design 30, 3512-3517.

Rice, J.R., 1972. Some remarks on elastic crack-tip stress fields. International Journal Solids Structures 8, 751-758.

Ritchie, R.O., Boyce, B.L., Campbell, J.P., Roder, O., Thompson, A.W., Milligan, W.W., 1999a. Thresholds for high-cycle fatigue in turbine engine Ti-6Al-4V alloy. International Journal of Fatigue 21, 653-662.

Ritchie, R.O., Davidson, D.L., Boyce, B.L., Campbell, J.P., Rode, O., 1999b. High cycle fatigue of Ti-6Al-4V. Fatigue Fracture Engineering & Material Structures 22, 621-631.

Roder, O., Peters, J.O., Thompson, A.W., Ritchie, R.O., 1999. Influence of simulated foreign object damage on the high-cycle-fatigue properties of Ti-6Al-4V for gas turbine blades. Proceedings: 4th National Turbine Engine High Cycle Fatigue Conference, Monterey, CA.

Rooke, D.P., Cartwright, D. J., 1976. Comprendium of Stress intensity factors. London: Ministry of Defence.

RTO, 2005. Best Practices for the Mitigation and Control of Foreign Object Damage-Induced High Cycle Fatigue in Gas Turbine Engine Compression System Airfoils. RTO Technical Report.

Rubio-Gonzalez, C., Ocana, J.L., Gomez-Rosas, G., Molpeceres, C., Paredes, M., Banderas, A., Porro, J., Morales, M., 2004. Effect of laser shock processing on fatigue crack growth and fracture toughness of 6061-T6 aluminum alloy. Material Science and Engineering A386, 291-295.

Rubio-Gonzalez, C., Felix-Martinez, C., Gomez-Rosas, G., Ocana, J.L., Morales, M., Porro, J.A., 2011. Effect of laser shock processing on fatigue crack growth of duplex stainless steel. Materials Science and Engineering A 528, 914-919.

Ruschau, J.J., Reji, J., Thompson, S.R., Nicholas, T., 1999a. Fatigue crack growth rate characteristics of laser shock peened Ti-6Al-4V. Journal of Engineering Materials and Technology 121, 321-329.

Ruschau, J.J., Reji, J., Thompson, S.R., Nicholas, T., 1999b. Fatigue crack nucleation and growth rate behaviour of laser shock peened titanium. International Journal of Fatigue, 199-209.

Ruschau, J.J., Nicholas, T., Thompson, S.R., 2001. Influence of foreign object damage (FOD) on the fatigue life of simulated Ti-6Al-4V airfoils. International Journal of Impact Engineering 25, 233-250.

Ruschau, J.J., Thompson, S.R., Nicholas, T., 2003. High cycle Fatigue limit stresses for airfoils subjected to foreign object damage. International Journal of Fatigue 25, 955-962.

Schindler, H-J., Cheng, W., Finnie, I., 1997. Experimental determination of stress intensity factors due to residual stresses. Exp. Mech. 37, 272–277.

Servetti, G., Zhang, X., 2009. Predicting fatigue crack growth rate in a welded butt joint: the role of effective R ratio in accounting for residual stress effect. Engineering Fracture Mechanics 76, 1589-1602.

Spakowski, A.E., Graab, J., 1957. Identification of foreign objects damaging compressor blades in turbojet engines, Research Memorandum, Lewis Flight Propulsion Laboratory, Cleveland, OH, National Advisory Committee for Aeronautics Washington.

Suresh, S., 2001. Fatigue of materials, 2nd edition. Cambridge University Press.

Suresh, S., Ritchie, R.O., 1984. Short crack effects, a consequence of crack tip shielding, Proceedings of Conference on Small fatigue Cracks, 167-189.

Swalla, D.R., Neu, R.W., 2006. Fretting damage assessment of titanium alloys using orientation imaging microscopy. Tribology International 39, 1016-1027.

Tada, H., Paris, P.C., Irwin, G.R., 1973. The Stress Analysis of Cracks Handbook, Del Research Corporation, Hellertown, Pennsylvania.

Taira, S., Murakami, Y., 1960. On the changes in residual stresses due to repeated stressing. In: Proceedings of the 3rd Japan Congress on Testing Materials, Kyoto, Japan, 52–55.

Thompson, S.R., Ruschau, J.J., Nicholas, T., 2001. Influence of residua; stresses on high cycle fatigue strength of Ti-6Al-4V subjected to foreign object damage. International Journal of Fatigue 23, 405-412.

Torres, M.A.S., Voorwald, H.J.C., 2002. An evaluation of shot peening, residual stress and stress relaxation on the fatigue life of AISI 4340 steel. International Journal of Fatigue 24, 877–886.

Voehringer, O., Hirsch, Th., Macherauch, E., 1984. Relaxation of shot peening induced residual stresses of Ti-6Al-4V by annealing or mechanical treatment. Proceedings: 5th Conference on Titanium, Munich, FRG, 2203-2210.

Wagner, L., 1999. Effect of mechanical surface treatments on fatigue performance of titanium alloys. In: Fatigue Behavior of Titanium Alloys. TMS, 253–265.

Wick, A., Schulze, V., Vohringer, O., 2000. Effects of warm peening on fatigue life and relaxation behaviour of residual stresses in AISI 4140 steel. Material & Science Engineering A293, 191–197.

Wu, X.R., Carlsson A.J., 1991. Weight functions and stress intensity factor solutions. 1st ed. Oxford: Pergamon Press.

Zhang, Y.K., Ren, X.D., Zhou, J.Z., Lu, J.Z., Zhou, L.C., 2009. Investigation of the stress intensity factor changing on the hole crack subject to laser shock processing. Material and Design 30, 2769-2773.

Zhang, Y.K, Lu, J.Z., Ren, X.D., Yao, H.B., Yao, H.X., 2009. Effect of laser shock processing on the mechanical properties and fatigue lives of the turbojet engine blades manufactured by LY2 aluminum alloy. Materials and Design 30, 1697-1703.

Chapter 3 Research methodologies

3.1 Experimental investigation

3.1.1 Material

In the aerospace industry rotating components such as blades in fan and compressor stages as well as static parts for airframes or landing gears are commonly made of titanium alloys. The test specimens in this study are made of titanium alloy Ti-6Al-4V, which is generally used for aerofoils in aero engines.

Titanium Ti-6Al-4V is a polycrystalline material. At a temperature of 882ºC pure titanium undergoes an allotropic transformation and changes from the low-temperature closed-packed hexagonal α-phase to the higher-temperature body centred cubic β-phase. Titanium alloys are classified in (near-α)-, (α-β)- and β-alloys, depending on the percentage of hexagonal close-packaged microstructure. Alloying elements tend to stabilise the α- or the β-phase which alters the transformation temperature and changes the shape and extend of the α-β field. α-stabilizers such as aluminium, carbon and nitrogen raise the transformation temperature, whereas vanadium decreases it by stabilizing the β-phase. Oxygen influences the α-phase by stabilizing intermettalic Ti_3Al-particles. The α-phase and β-phase create a lamellar structure known as Widmanstätten structure within the grains. Ti-6Al-4V is an α+β material where both phases exist at room temperature.

The specimens were supplied by Rolls-Royce plc., and machined from blanks for the production of fan blades. The material has a typical microstructure of a bimodal distribution of primary α-phase and lamellar colonies of α+β, as illustrated in Figure 3-1. The material was first forged in the β phase and continued into the α+β phases, then rolled in the α+β phase. The appropriate heat treatment was conducted to

optimize the properties of the titanium plates for fan blades. The materials properties at room temperature are: Young's modulus, 103GPa, yield stress, 860MPa and tensile strength, 980MPa. The chemical composition of the material is given in Table 3-1 (Rolls-Royce standard MSRR 8610).

Table 3-1 Chemical composition of Ti-6Al-4V alloy in wt. (%).

Elements	**Al**	**V**	**Fe**	**C**	**O_2**	**N_2**	**Y**	**H_2**
MSRR 8610	5.50 - 6.75	3.5 - 4.5	< 0.3	< 0.08	0.14 - 0.23	< 0.03	< 0.005	0.0125

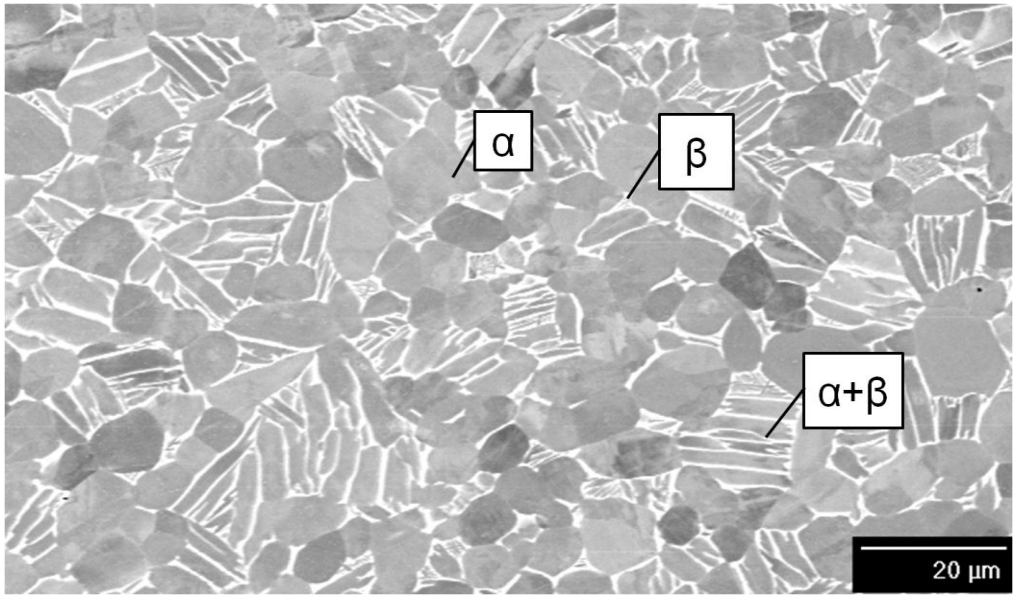

Figure 3-1 The bimodal microstructure of Ti-6AL-4V (as received).

3.1.2 Specimen

Two types of specimen made of the same Ti-6Al-4V material were used in this study. A simplified *plate specimen* was used to verify the four-point bending rig and to obtain the crack length calibration from direct current potential drop readings; whilst simplified *aerofoil specimens* were used for the main study.

FOD damage on blades in aero-engines is known to occur mostly on the leading edge of an aerofoil section. The *aerofoil specimen* was designed to be similar to a

typical leading edge of in-service compressor aero engine or fan blades, with an aerofoil session and a rectangle session. The leading edge of the aerofoil section has a circular tip of a radius of 0.53mm, and an elliptical taper to bridge the tip and another circular radius of 3mm next to the rectangular section of the sample (Figure 3-2). Part of the taper section of the sample was later treated with laser shock peening (LSP), whilst the rectangular section is significantly thicker than the aerofoil section, necessary to retain the residual stresses as well as to prevent buckling during four-point bend fatigue testing.

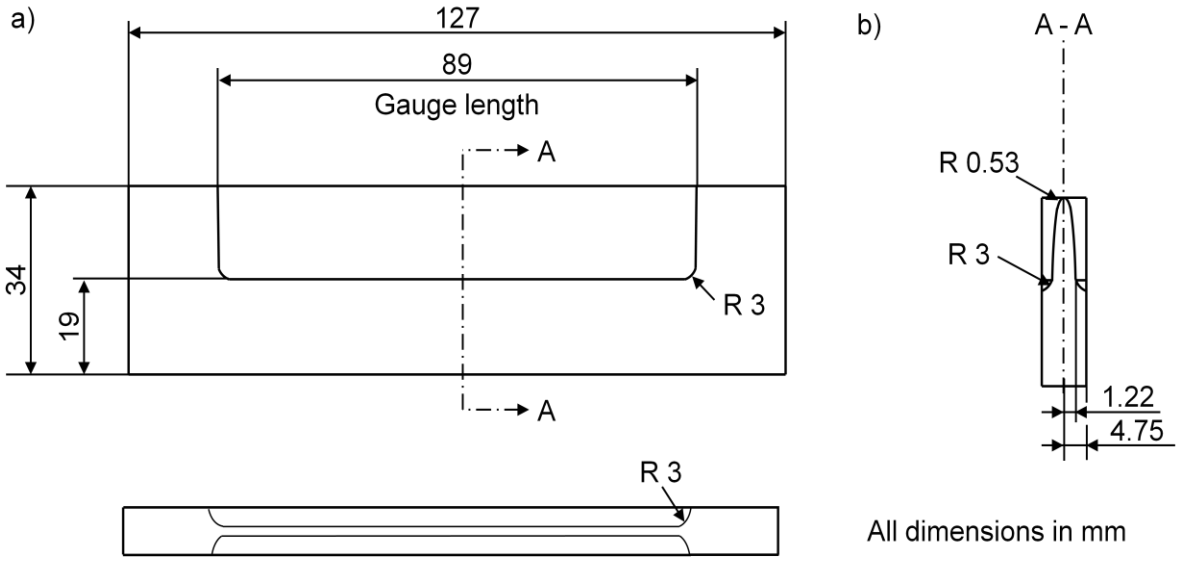

Figure 3-2 Showing a) the geometry of the four-point bend aerofoil specimen (dimensions in mm), and b) the cross sectional view of the aerofoil specimen.

To evaluate the experimental setup, two virgin (not laser shock peened (LSPed) or foreign object damaged (FODed)) plate specimens made of the same material and four virgin aerofoil specimens were used. To simulate a FOD indent, notches were cut, using the electro discharge machining (EDM) technique, to a similar notch depth to that obtained from a ballistic cubical FOD impact.

Similar aerofoil specimens with varied geometries of the leading edge and of same material were used in previous studies, notably: (Ruschau et al., 1999a; 1999b; Ruschau et al., 2001; Peters and Ritchie, 2000; Peters and Ritchie, 2001; Mall et al., 2001; Peters, 2003; Ruschau et al., 2003; Ding et al., 2007a; Hall et al., 2008).

3.1.3 Laser Shock Peening (LSP)

The specimens were laser shock peened (LSPed) on both sides of the leading edge using parameters that provided an optimum balance between induced residual stresses and acceptable distortion of the leading edge profile. The total LSPed area measured approximately 65mm x 6mm wide from the tip of the leading edge. The distortion on the surface is shown in Figure 3-3.

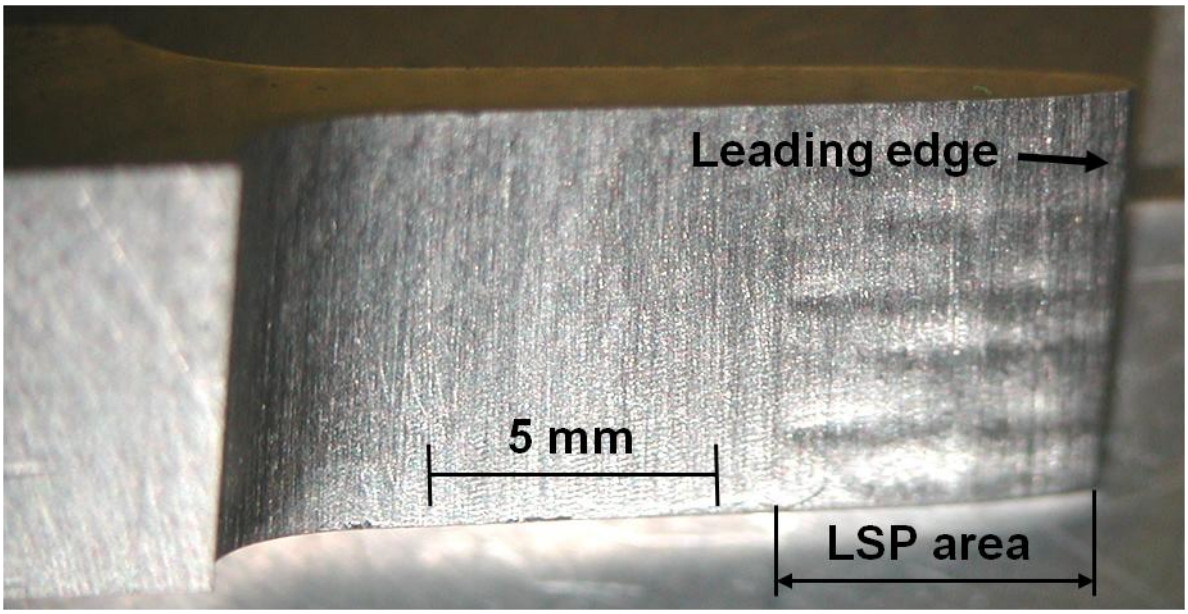

Figure 3-3 Leading edge of the aerofoil specimen and distortion caused by the laser shock treatment near the tip of the leading edge.

3.1.4 Foreign Object Damage (FOD)

FOD was simulated using a light gas gun at the University of Oxford, UK. The gun consisted of a 2-litre gas cylinder connected via a pneumatic valve to a 2.5m long sleeved barrel, as shown in Figure 3-4; and described in detail in Nowell et al., (2008). The target was held in a cross-vice which can be rotated and translated with micrometer precision.

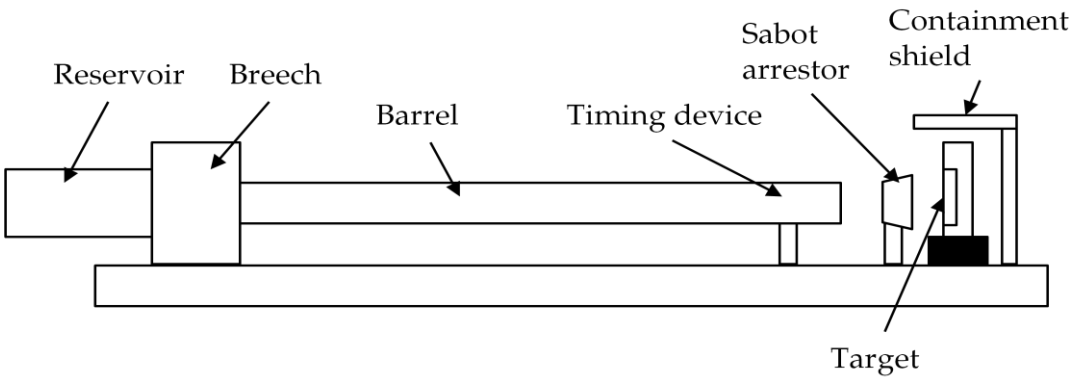

Figure 3-4 Schematic diagram of the gas gun at Oxford, UK (Nowell, 2008).

Velocity was measured using photodiodes at the end of the barrel. Hardened steel cubes with hardness values between 62 and 64 on the Rockwell C scale were used. Two impact conditions, edge first for 0° and point first for 45° onto the mid-point of the leading edge, as shown in Figure 3-5a, were specified as follows:

(i) Zero degree orientation (Θ=0°), using a 3.2mm hardened steel cube at an impact velocity of 200 m/s;

(ii) 45 degree orientation (Θ=45°), using a 4.8mm hardened steel cube at an impact speed of 250m/s. In this case the position of the specimen relative to the gun-axis was varied in order to adjust the amount of overlap between the cube and the leading edge to achieve a desired impact depth.

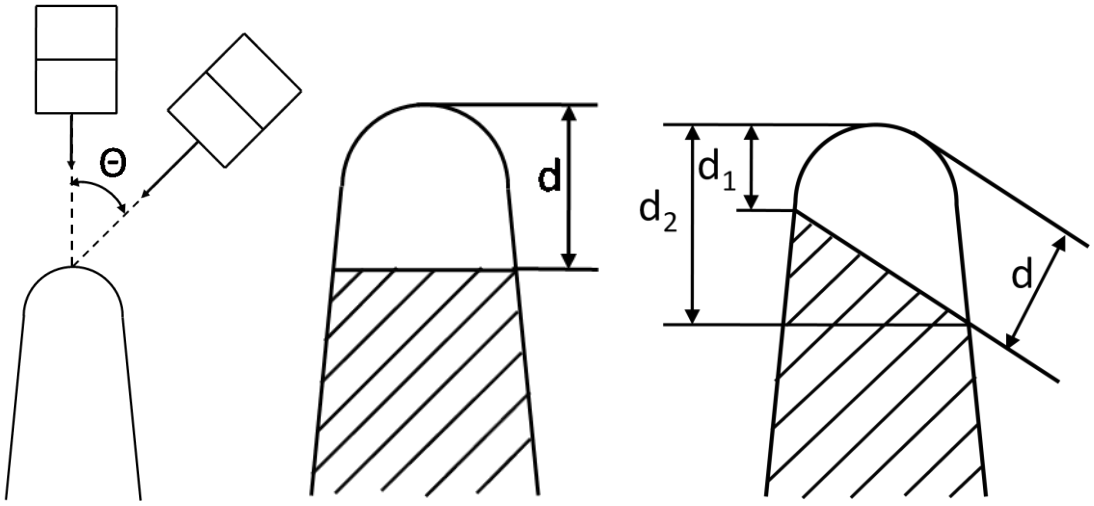

Figure 3-5 a) Schematic of selected impact angles; notch measurement techniques for b) a 0° impacted notch, and c) a 45° impacted notch.

The nominal impact velocities were 200m/s and 250m/s, representing typical values of impact velocities observed in-service on aero engine fan blades. The recorded velocities were within 8% of the nominal values. Every specimen impacted was examined by suitably positioning an optical microscope to achieve a profile view of the notches and measure the depth from the leading edge on each side, as shown in Figure 3-5b-c. An average notch depth might also be estimated by the distance (d) from the leading edge to the centre of the notch root (Figure 3-5c).

3.1.5 Mechanical test system and setup

Fatigue testing of plate and aerofoil specimens was carried out under a 4-point bend arrangement in a servo-hydraulic twin actuator ESH 100kN testing machine, as shown in Figure 3-6.

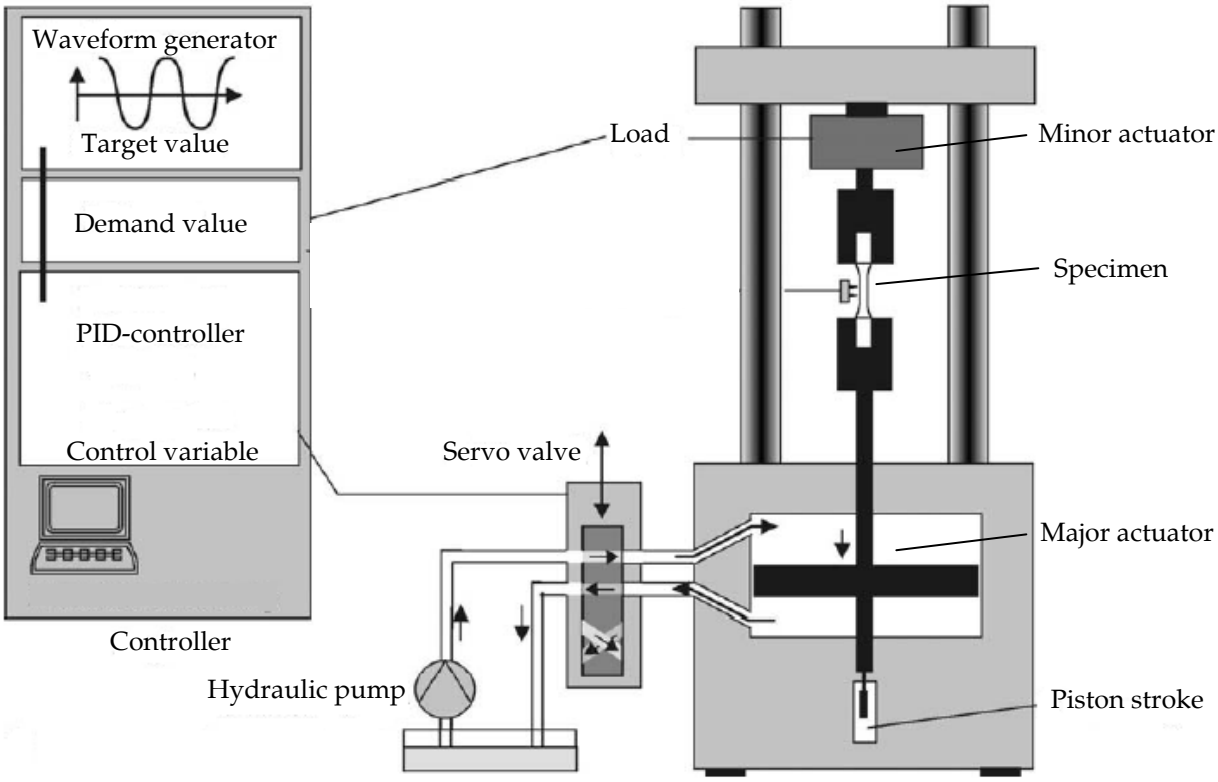

Figure 3-6 Schematic assembly of the servo-hydraulic twin actuator after (Krupp, 2004).

This hybrid machine combines an electromagnetic vibrator with a servo hydraulic cyclic testing machine and is capable of producing low frequency major cycles (for LCF) and high frequency minor cycles (for HCF) either separately or conjointly. Due to the limitation of the loading capacity of the test rig, a 4-point bend testing setup was chosen and developed. This setup provides a gauge section between the two inner loading rollers with a uniform bending moment within the specimen that includes the FOD notch. Fatigue tests may be interrupted at stages and optically examined due to the convenience of specimen mounting and dismounting.

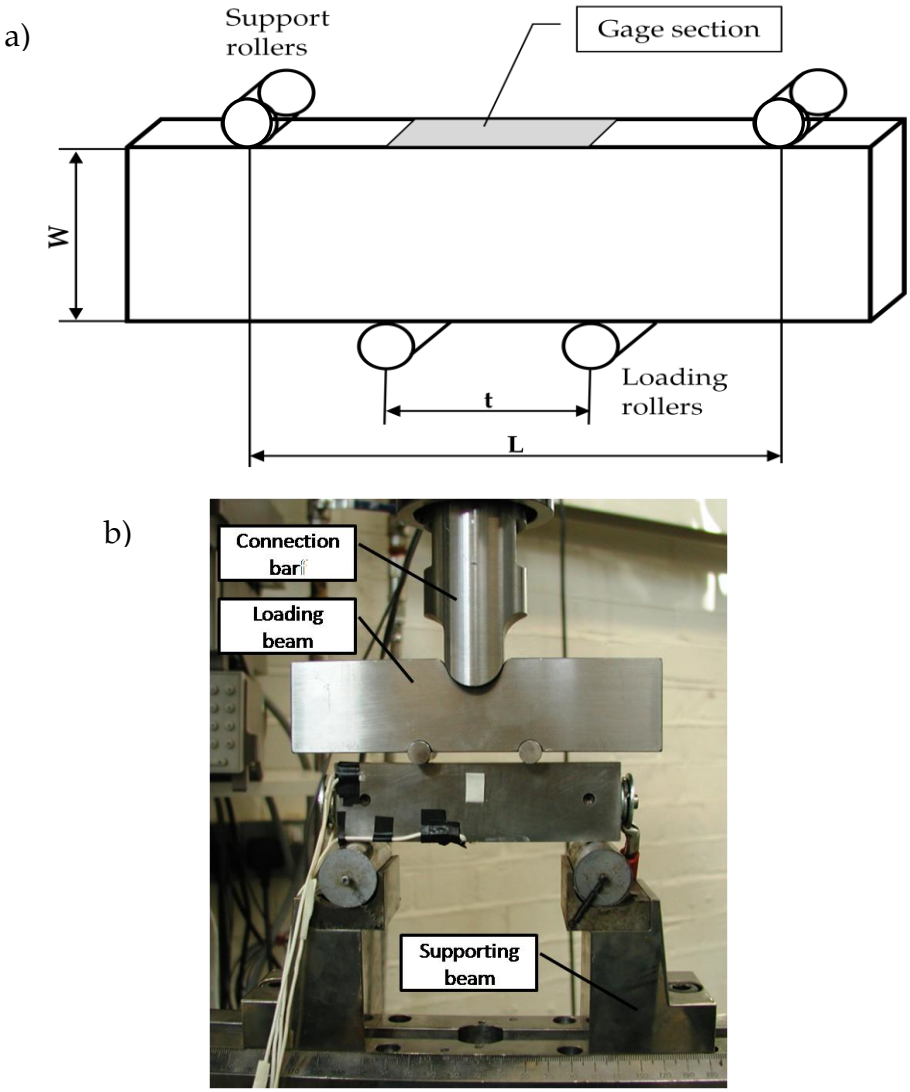

Figure 3-7 a) Schematic four point bend setup (Cadario and Alfredsson, 2007), and b) the present 4-point bend experimental setup.

A number of finite element studies (Zhai et al., 1999; Grabowski and Yates, 1992) have been carried out to investigate the relation between the specimen geometry and the stress distribution in four-point bending configurations to achieve an uniform pure-bending stress distribution within the specimen cross-section (Figure 3-7a). They found ideal values for load-roller spacing/specimen width (t/W) and support-roller spacing/load-roller spacing (L/t) are between 1.2 and 1.5 and between 3 and 5, respectively. This configuration was the optimum testing geometry which led to a relatively uniform stress distribution consistent with the value calculated by the beam theory.

To achieve these three parts were designed:

1. a *connection bar* that extends the loading rod of the hydraulic twin-actuator,
2. a *loading beam* which accommodates the loading rollers at the required spacing,
3. a *supporting beam* which accommodates the supporting rollers.

Figure 3-7b shows the four-point bending fatigue testing arrangement designed for this study. The hinge connects the extension bar of the loading rod. The grooves of the loading beam are chamfered and larger than the diameter of the rollers to allow movement of the rollers whilst loading.

A semi-sphere connection between the hinge and loading beam provides an evenly distributed contact pressure and facilitates the alignment procedure. For a given specimen width W of 34mm, and a support-roller spacing (L) of 107mm, limited due to the leading edge of the specimen, the load-roller spacing (t) was chosen to be 57mm which gives a (L/t) ratio of 1.9 and a (t/h) ratio of 1.7. The technical drawings including the dimensions of the loading and connection rig can be found in the Appendix A. All parts were manufactured out of stainless steel.

3.1.6 Fatigue testing methods and the test matrix

Tests were carried out under cyclic loading conditions including low cycle (LCF), high cycle (HCF) and a combined LCF and HCF loading block. A load-increasing scheme following Bellows et al. (1999) was used, where the load level was raised between 3% and 5% when a crack growth was not detected after $2x10^6$ number of cycles, until a crack growth was detected. The test was terminated when the crack length reached about 7mm. The load cycle for LCF was a trapezoidal waveform with one second rise and fall, and one second hold at maximum and minimum load giving a frequency of 0.25Hz, and a load ratio of R=0.1. The load cycle for HCF was a sinusoidal wave form with a frequency of 80Hz and a stress ratio of R=0.7. A conjoint action of LCF and HCF cycles, referred to as combined LCF+HCF loading that represents a simplified flight spectrum, was also used as shown in Figure 3-8.

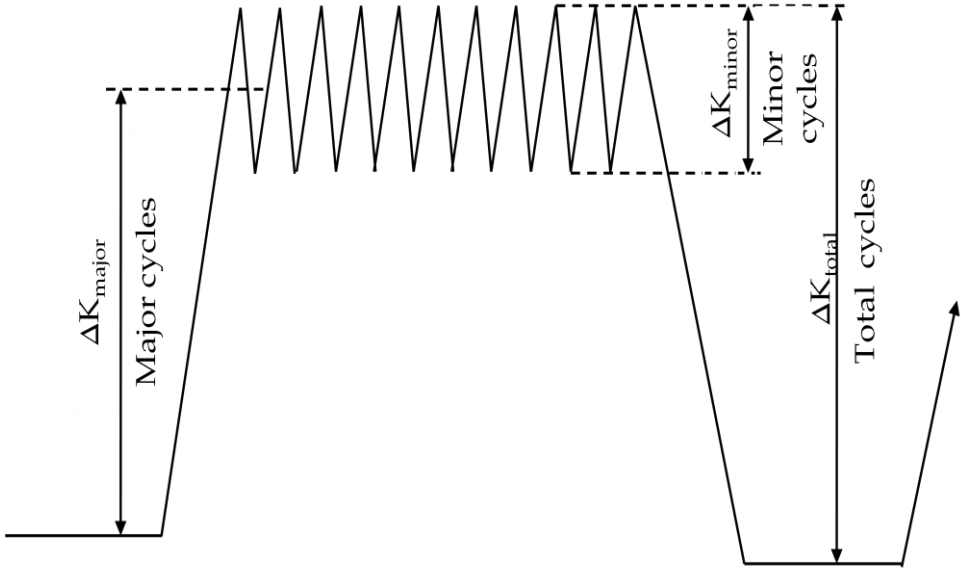

Figure 3-8 A combined cycle waveform consists of one LCF and n HCF cycles.

In this simplified load sequence, one loading block was composed of a LCF cycle which was superimposed by 1000 HCF cycles. To provide such a block, the hold time at the maximum load of a LCF cycle was extended to 12.5s to accommodate 1000 HCF cycles and the maximum stress σ_{max} of HCF cycles was the same as that of the LCF cycles. A summary of the tests, including loading and impact conditions, is summarised in Table 3-2.

Table 3-2 The Test Matrix.

Impact Condition	Number of tests	Type of test	Stress ratio R	Cycle ratio LCF:HCF
EDM notch	4	LCF+HCF	0.1/0.7	1:1000
FOD 0	2	LCF	0.1	n.a.
FOD 0	2	HCF	0.7	n.a.
FOD 0	2	LCF+HCF	0.1/0.7	1:1000
FOD 45	2	LCF	0.1	n.a.
FOD 45	2	HCF	0.7	n.a.
FOD 45	2	LCF+HCF	0.1/0.7	1:1000

3.1.7 Crack detection and monitoring methods

The use of fracture mechanics to accurately model fatigue crack propagation rates requires an accurate measurement of crack size from initiation to final fracture. In this study, both crack initiation and growth were monitored using the direct current potential drop (DCPD) method and surface replicas (SR).

The acetate surface replication method is well established and has been used for decades, whereas the silicon rubber-based technique represents a relatively new SR method (Newman et al., 2009). The acetate replica technique was used in this study due to availability and experience. The area of interest was covered by a strip of transparent acetate, with a small amount of acetone applied between the component and the strip. Acetone dissolves and softens the acetate tape allowing it to adhere to the specimen and impress the surface features such as a crack onto the tape. After the acetone dries, the acetate strip was removed as a replica of the surface and can be

investigated under a microscope. In this study, measurement of crack length was performed on both sides of the FOD notch, using the surface replica method to calibrate and confirm the measurements obtained from the potential drop method as well as to monitor crack initiation.

The potential drop (PD) method provides a sensitive, flexible and adaptable system for automated data collection and processing, with no need for direct time consuming optical measurements. The principle of this method involves a direct current flowing through the test piece and an accurate measuring device which measures the electrical potential drop across the flaw by a pair of potential probes (Figure 3-9). In a parallelepiped material of uniform electrical conductivity with a plane crack, the voltage follows the Laplace equation to satisfy the equation of continuity and Ohm's law. When the crack propagates, the resistance, and hence the measured potential drop, increases due to the reduction in uncracked cross sectional area of the test piece. A direct current (DC) measuring system was adopted in this study (Belloni et al., 2002). There are a few issues related to this method and these are discussed as follows (ASTM E 647-08):

I. Error sources

The main error sources in a PD system are: temperature changes, thermoelectric errors and failures in the correct positioning of the leads (Wei and Brazill, 1981; Donald and Ruschau, 1991; Gangloff et al., 1992).

Temperature variations are in the range of 0.1% to 0.15% of the measured potential drop and do not need any correction filter (Belloni et al., 2002). Compared to constant current flow, a pulsed current causes smaller rise in temperature due to the joule effect[3-1] and is therefore often recommended for both ambient and elevated temperatures (Bardal et al., 1982).

[3-1] The Joule effect expresses the relationship between the heat generated by the current flowing through a conductor: $Q=I^2xRxt$, where Q is the heat generated by a constant current I flowing through a conductor of electrical resistance R, for a time t. The unit of Q is joule and the heating effect of conductors flowed through by currents is known as Joule heating/effect.

Thermo electrical forces due to the interface resistance of bimetallic connections such as specimen to probe can affect the measurements. At room temperature the thermo-electromotive force in μV/K due to a copper-steel connection is about 40 times higher than that for the connection between copper and a noble metal (Ag, Au, Pt) (Belloni et al., 2002).

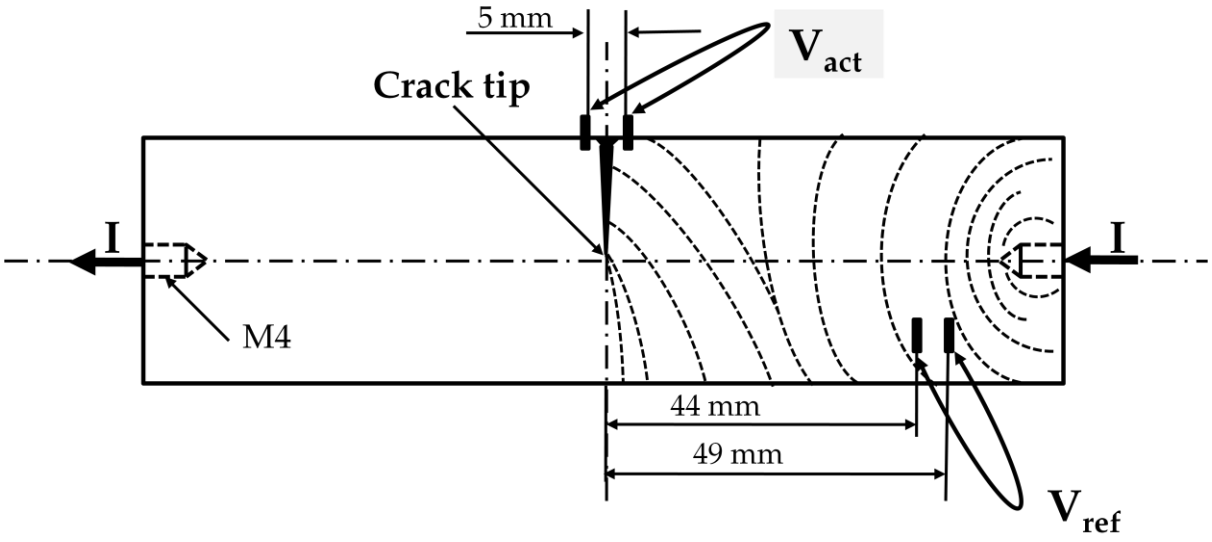

Figure 3-9 Principle of the PD method, indicating current in- and output (I), active (V_{act}) and reference potential (V_{ref}) as well as electrical field distribution within the specimen (dashed) (Belloni et al., 2002).

II. Positioning current input, active and reference leads

To obtain a crack monitoring system with high sensitivity, accuracy, repeatability and resolution, the electrical field distribution within the specimen is of primary importance. Analyses have been conducted by Ritchie et al. (1971), Tong (2001) and Belloni et al. (2002), investigating the relations between the current input location, the number of probes and the probe location. The current distribution close to the crack tip plane is most uniform if the current inputs are applied at the ends of the specimen, as indicated in Figure 3-9.

The active potential measurement is taken by a pair of spot welded leads closely spaced across the notch. Most common positions for the active probes are close to the notch on the specimen's *top surface*, because small errors in positioning are less

critical on the measured potential difference compared to lateral positioning (Tong, 2001). *Lateral surface* positioning close to the notch tip gives a greater sensitivity, but less reproducible results, because the gradients at the crack tip are very high and small variations in the probe location can cause large measurement errors for a given crack length (Klintworth and Webster, 1979).

A reference potential compensates system errors such as electrical noise, thermoelectric effects and instrumentation drift during the test (Gangloff et al., 1992) by normalising the active potential. Reference leads are normally placed at a location where the voltage reading is not affected by stable crack growth, electrical field irregularities or plastic deformation of the specimen (Donald and Ruschau, 1991; Cerny, 2004; Cerny et al., 1992; Ennaceur et al., 2006).

The DCPD method adopted in this study has the following features to reduce the influence of potential errors:

- a 40 amps constant current was used and pulsed for 1 second, triggered each time when peak load was reached,
- a Keithley 2000 digital high resolution nano-voltmeter with a resolution of 1μV was used to collect the data, and digitally recorded onto a personal computer (PC),
- noble and fine platinum (Pt) wires of a diameter of Ø 0.2 mm were used,
- current leads were screwed to the ends of the specimens, as the threads were manufactured to high precision and guaranteed an excellent electrical connection,
- potential leads were spot-welded onto the specimen using a high resolution MacGregor constant current micro welder[3-2], which employs a micrometer

[3-2] A stabilised constant voltage passes through a welding head fitted with parallel tungsten electrodes. The result is two weld points at a distance of 0.4 mm, producing a robust weld. The weld settings include weld duration, weld voltage, electrode spacing and electrode pressure, which are dependent of the probe wire material, the thickness and the specimen material.

mounted specimen holder, a fine tipped electrode, and a stereomicroscope, to precisely locate potential probes,

- active potential leads were placed close to the FOD notch (2.5mm), on either side, which gave good sensitivity of the measured voltage and also ensured that the welded wires were sufficiently far away from the notch to prevent cracks initiating from the wires themselves,
- reference leads were attached away from any influencing parameters,
- the laboratory was air-conditioned to minimise the temperature variation.

The whole system was controlled by a PC using a customized program written in Test-point software, which triggered the direct current, measured and recorded the voltage ratio and recorded the corresponding number of cycles each time when a maximum load of the cycle was detected.

3.1.8 Mechanical and DCPD system calibration

I. Mechanical system calibration

The calibration of the hydraulic twin actuators load cell was performed by a specialist company, who checked the outputs from the testing machine against a standard load cell and load indicator. This work was performed according to the European standards EN 10002-2, EN 1000-3 and the accuracy of the load cell was rated as within 0.5%.

II. DCPD calibration

The integrity of the DCPD technique is completely reliant on an accurate calibration, which relates the change in voltage readings to the change in crack length.

As an analytical PD calibration is not available for the current complex specimen geometry with an irregular FOD notch, experimental calibrations were carried out. The PD calibrations are expressed as a relation of the active electrical potential V_{act} or

its normalized value by the reference potential, V_{ref}, to the crack length: $a=f(V_{act}/V_{ref})$.

(i) Analogue Calibration

Analogue calibration was used to obtain a relationship between the voltage ratio and the crack length and to determine the locations for the current, active and reference potential leads (Clark and Knott, 1975; Hicks and Pickard, 1982; Read and Pfuff, 1991; Donald and Ruschau, 1991). This technique simplifies the 3-dimensional specimen geometry to a 2-dimensional shape by examining the current distribution on the 2-dimensional specimen profile.

The 2-D aerofoil specimen shape was simulated using aluminium foil which was cut to a size of 5 times the geometry of the sample. A constant current of 4 ampere was supplied at the sides. The foil was cut in predetermined small increments using a scalpel to simulate the crack extension from the notch. After each increment, the crack length was measured and the corresponding voltage readings were taken from a digital voltmeter (DVM) with a resolution of 1μV. This procedure was repeated, probes were adjusted until satisfying sensitivity and repeatability was reached. The technique proved to be useful in obtaining an approximate PD calibration rapidly and inexpensively.

(ii) Plate and aerofoil specimen calibration

These experiments were aimed to verify and calibrate the designed experimental arrangements and prove their repeatability. The specimens were pre-notched by electrical discharge machining (EDM). The notch of the plate specimens was 3mm deep and 3mm wide at the mind-point of the leading edge. FOD notches were simulated in four virgin aerofoil specimens by EDM, as shown in Figure 3-10. Due to scatter in FOD impact notches two different notch depths for each impact condition were chosen: depths of 0.7mm and 1.3mm for 0º impacts and average notch depths of 1.5mm and 1.8mm for 45º impacts. On both specimens type M3 threads (6mm

deep) were drilled. Copper wires with a diameter of 5mm were screwed at both ends of the specimen to carry the current. Spot welding of the potential leads was done by using a MacGregor micro welder. The nano-voltmeters and power supply were stabilised before starting the test.

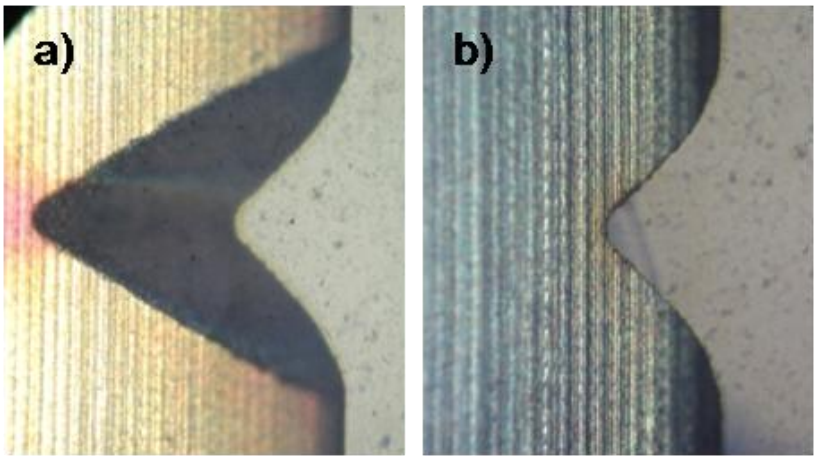

Figure 3-10 a) Entry and b) exit sites of a simulated 45° FOD impact by EDM for DCPD calibration.

A calibration curve can be obtained either by using a set of specimens (typically three specimens) or a single specimen (Belloni et al., 2002). If a single specimen is employed a beach marking technique should be used. The beach marking technique uses alternately two different loading conditions to produce a change in the fracture surface appearance due to the change in the crack growth mechanism.

In this work, the specimen was cyclically loaded under load control of combined HCF+LCF loading blocks at a load ratio R of 0.7 for HCF and a load ratio of 0.1 for LCF. After reaching a predetermined voltage ratio that corresponds to a certain crack length, the test was stopped; replicas were taken on both sides of the specimen surface and the crack lengths were measured under an optical microscope. A different frequency from that of the previous step was applied to generate a "beach mark" on the fracture surface. This frequency change gave rise to an increase in fatigue crack growth rate, affected by a change in crack growth mechanism, which created a change in the appearance of the fracture surface (Burgess, 2005). By applying alternating blocks of the two frequency conditions a "marked" fracture surface was generated and the crack depths were measured and related to the

voltage ratios. These measurements were then compared with the replica crack lengths. Frequencies of 35Hz and 65Hz were used to produce the change of surface morphology. Post fatigue testing, the sample was heat tinted at about 450ºC for around 2h, to oxidise the fracture surfaces and broken open to determine the final crack shape and measure the final crack length. Figure 3-11 shows the fracture surface generated from such a beach- marked test.

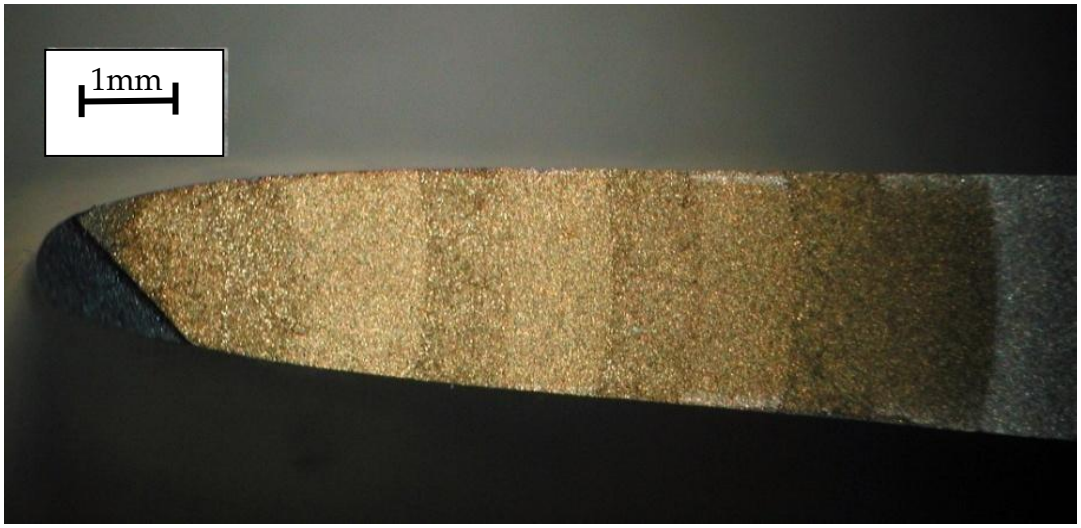

Figure 3-11 Crack fronts in cross sectional view of the leading edge, produced by alternating fatigue loads and heat tinting treatment post testing.

3.1.9 K calibration

In this work the following K calibrations for a four point bend specimen were used:

$$K_I = \frac{M}{BW^{3/2}} f_b\left(\frac{a}{W}\right) \tag{3-2}$$

where a is the crack length, M is the bending moment, B and W are the specimen thickness and width respectively; and

$$f_b\left(\frac{a}{W}\right) = 6\left\{\pi\left(\frac{a}{W}\right)^{0.5}\left[1.12 - 1.39\left(\frac{a}{W}\right) + 7.32\left(\frac{a}{W}\right)^2 - 13.1\left(\frac{a}{W}\right)^3 + 14\left(\frac{a}{W}\right)^4\right]\right\} \tag{3-3}$$

for 0<a/W<0.6 after Brown and Srawley (1966); and

$$f_b\left(\frac{a}{W}\right) = \frac{3.99}{\left(1-\frac{a}{W}\right)^{1.5}} \quad (3\text{-}4)$$

for a/W>0.6 after Wilson (1970). The theoretical solution was verified by a 2D finite element model in ABAQUS (Chapter 5). The bending moment (M) of the 4 point bending set-up, as schematically shown in Figure 3-7, was calculated by:

$$\sigma = \frac{M \times y}{I_x} = \frac{3P(l-h)}{Wh^2} \quad (3\text{-}5)$$

where l is the support roller spacing, t is loading roller spacing, I_x is the moment of inertia, y is the distance in Y direction from the neutral axis and P is the applied load.

3.2 Scanning electron microscopy

To characterise FOD damage features and fatigue fracture surfaces, a scanning electron microscopy (SEM) study was carried out using a JEOL JSM-6100 SEM. Indents from both head-on and 45° FOD impacts were examined at various orientations, and at selected stages of the fatigue crack growth process. Specifically, characterisation was carried out for a) post FOD but prior to fatigue testing, b) after early fatigue crack growth, and c) after fatigue fracture. The latter two steps provide insight into the location and the nature of the crack initiation and early crack growth associated with the FOD damage features.

To investigate the microstructure of the material a back-scatter electron (BSE) detector within the SEM was used. Preparation of titanium is a delicate process due to its high ductility which makes it difficult to cut, grind and polish the material (Ezugwu and Wang, 1997). The material tends to 'smear', which distorts the microstructure. For BSE analysis the specimens were mounted in conductible epoxy

resin, ground and polished until a mirror finish. The grain size of the grinding paper was successively reduced until the last step of a grit size of 4000 per inch, giving a grain size of about 5μm. Subsequently the surface was polished with a diamond paste of grain sizes of 4 and 2μm. For the final polishing step a colloidal silica dioxide (SiO_2) with a particle size of 0.04μm was used. This results in a mirror finish surface, free of mechanical deformation or residual stresses due to polishing.

3.3 Finite element analysis

For this study the general purpose finite element solver ABAQUS was used to obtain the modified stress intensity factor K solutions, considering the effects of the residual stresses due to LSP and FOD.

FOD and LSP both produce residual stresses (RS) which will influence the stress field near the crack tip significantly. The current methods to modify K solutions considering RS include the FE method (Hall et al., 2008; Gallagher et al., 2001; Gandossi et al., 2001) and the weight function method (e.g Parker, 1982; Bao et al., 2010). In this work both methods were used to obtain the modified SIF. To do so, three steps were carried out: 1) determination of the nominal elastic K (initial crack dimensions must be assumed) for airfoil/notch geometry; 2) superimposition of RS due to LSP+FOD for airfoil/notch geometry; 3) calculation of modified K with the residual stresses considered.

3.4 References

ASTM-E647-08, Standard test method for measurement of fatigue crack growth rates.

Bao, R., Zhang, X., Yahaya, NA., 2010. Evaluating stress intensity factors due to weld residual stresses by the weight function and finite element methods. Engineering Fracture Mechanics 77, 2550-2566.

Bardal, E., Berge, T., Groevlen, T., Haagensen, M., Foerre, B.M., 1982. A Pulsed d.c. Method for Measuring Crack Growth. Engineering Materials Advisory Services, 139-158.

Belloni, G., Gariboldi, E., Lo Conte, A., Tono, M., Speranzoso, P., 2002. On the Experimantal Calibration of a Potential Drop System for Crack Length Measurements in a Compact Tension Specimen. Journal of Testing and Evaluation 30.

Bellows, R.S., Muju, S., Nicholas, T., 1999. Validation of the step test method for generating Haigh diagrams for Ti-6Al-4V. International Journal of Fatigue 21, 687-697.

Brown, W.F., Srawley, J.E., 1966. ASTM STP 410.

Burgess, A., 2005. Influence of surface damage on the fatigue behaviour of a shot peened nickel base superalloy at elevated temperature. PhD thesis, University of Portsmouth, UK.

Cadario, A., Alfredsson, B., 2007. Fatigue growth of short cracks in Ti-17: Experiments and simulations. Engineering Fracture Mechanics, 2293-2310.

Cerny, I., Linhart, V., Minarik, J., Hulik, P., 1992. Modification of D.C. potential Method for Short Specimens. In Vol I: Fatigue and Fracture Mechanics, by Cartwright., D.J., Nisitani., H., Aliabadi., M.H., 61-76. Southampton, Boston: Computational Mechanics Publications.

Cerny, I., 2004. The use of DCPD method for measurement of growth of cracks in large components at normal and elevated temperatures. Engineering Fracture Mechanics, 837-848.

Clark, G., Knott, J.F., 1975. Measurement of Fatigue Cracks in Nocked Specimens by Means of Theoretical Electrical Potential Calibration. Journal of the Mechanics and Physics of Solids 37, 265-276.

Ding, J., Hall, R.F., Byrne, J., Tong, J., 2007a. Fatigue crack growth from foreign object damge under combined low and high cycle loading. Part I: Experimental studies. International Journal of Fatigue 29, 1339-1349.

Donald, J.K., Ruschau, J., 1991. Direct Current Potential Difference Fatigue Crack Measurement Techniques. In Fatigue Crack Measurement: Techniques ans Applications, by Smith R.A., Ritchie R.O. Marsh K.J., 11-38. West Midlands: EMAS - Engineering Materials Advisory Services Ltd..

Ennaceur, C., Laksimi, A., Herve, C., Cherfaoui, M., 2006. Monitoring crack growth in pressure vessel steels by the acustic emission technique and the method of potential difference. International Journal of Pressure Vessels and Piping, 197-204.

European Committee for Standardisation (CEN), Metallic materials-tensile test-calibration of the force measuring systems of tensile testing machines, EN 10002-2, 1994.

European Committee for Standardisation (CEN), Metallic materials-tensile test-calibration of force proving instruments used for verifying axial testing machines, EN 10002-3, 1994.

Ezugwu, E.O., Wang, Z.M., 1997. Titanium alloys and their machinability - a review. Journal of Materials Processing Technologie 68, 262-274.

Gallagher, J.P., van Stone, R.H., de Laneuville, R.E., Gravett, P., Bellows, R.S., 2001. Improved High-Cycle Fatigue (HCF) Life Prediction. Dayton: Dayton Univ OH Rsearch Inst..

Gandossi, L., Summers, S.A., Taylor, N.G., Hurst, R.C., Hulm, B.J., Parker, P.D., 2001. The potential drop method for monitoring crack growth in real components subjected to combined fatigue and creep conditions: Application of FE techniques for deriving calibration curves. International Journal of Pressure Vessels and Piping 78, 881-891.

Gangloff, R.P., Slavik, D.C., Piascik, R.S., Van Stone, R.H., 1992. Direct Current Electrical Potential Measurement of the Growth of Small Cracks. In Small-Crack Test Methods, by Allsison J.E. Larsen J.M., 116-168. Philadelphia, Pa: American Society for Testing and Materials.

Grabowski, L., Yates, J.R., 1992. The effect of specimen geometry on short-crack growth behaviour of a nickel-based superalloy. International Journal of Fatigue, 227-232.

Hall, R., Byrne, J., Zhao, T., Tong J., 2008. Influence of foreign object damage on fatigue crack growth of gas turbine aerofoils under complex loading conditions. Fatigue & Fracture of Engineering Materials & Structures 31, 386-397.

Hicks, M.A., Pickard, A.C., 1982. A Comparison of Theoretical and Experimental Methods of Calibrating the Electrical Potential Drop Technique for Crack Length Determination. International Journal of Fracture 20, 91-101.

Klintworth, G.C., Webster, G.A., 1979. Optimization of the Electrical-Potential Methods of Measuring Crack Growth. Journal of Strain Analysis 14, 187-192.

Krupp, U., 2004. Mikrostrukturelle Aspekte der Rissinitierung und -ausbreitung in metallischen Werkstoffen.

http://dokumentix.ub.uni-siegen.de/opus/volltexte/2005/92/pdf/krupp.pdf

Mall, S., Hamrick, J.L., Nicholas, T., 2001. High cycle fatigue behavior of Ti-6Al-4V with simlated foreign object damage. Mechanics of Materials 33, 679-692.

Newman, J.A., Willard, S.A. Smith, S.W., Piascik, R.S., 2009. Replica-based crack inspection. Engineering Fracture Mechanics 76, 898-910.

Nowell, D., 2008. Ballistic simulation of foreign object damage on 20 fatigue specimens, Report, University of Oxford.

Parker, AP., 1982. Stress intensity factors, crack profiles, and fatigue crack growth rates in residual stress fields, ASTM STP 776. American Society for Testing and Materials, 13-31.

Peters, J.O., 2003. Mikrostruktur, Ermuedung und Bruch hochfester Titanlegierungen. PhD Thesis, Technical University of Hamburg-Harburg.

Peters, J.O., Ritchie, R.O., 2000. Influence of Foreign-object Damage on Crack Initiation and Early Crack Growth During High Cycle Fatigue of Ti-6Al-4V. Engineering Fracture Mechanics, 193-207.

Peters, J.O., Ritchie, R.O., 2001. Foreign-object damage and high cycle fatigue of Ti-6Al-4V. Materials Science and Engineering A 319-321, 597-601.

Read, D.T., Pfuff M., 1991. Potential Drop in the Center-Cracked Panel with Asyetric Crack Extension. International Journal of Fracture 48, 219-229.

Ritchie, R.O., Garrett, G.G., Knott, J.F., 1971. Crack-Growth Monitoring: Optimization of the Electrical Potential Technique Using an Analouge Method. International Journal of Fracture Mechanics 7, 462-467.

Rooke, D.P., Cartwright, D.J., 1976. Comprendium of Stress intensity factors. London: Ministry of Defence.

Ruschau, J.J., Reji, J., Thompson, S.R., Nicholas, T., 1999a. Fatigue crack growth rate characteristics of laser shock peened Ti-6Al-4V. Journal of Engineering Materials and Technology 121, 321-329.

Ruschau J.J., Reji, J., Thompson S.R., Nicholas T., 1999b. Fatigue crack nucleation and growth rate behaviour of laser shock peened titanium. International Journal of Fatigue, 199-209.

Ruschau, J.J., Nicholas, T., Thompson, S.R., 2001. Influence of foreign object damage (FOD) on the fatigue life of simulated Ti-6Al-4V airfoils. International Journal of Impact Engineering 25, 233-250.

Ruschau J., Thompson S.R., Nicholas T., 2003. High cycle Fatigue limit stresses for irfoils subjected to foreign object damage. International Journal of Fatigue 25, 955-962.

Tong, J., 2001. Notes on direct current potential drop calibration for crack growth in compact tension specimens. Journal of Testing and Evaluation, 402-406.

Wei, R.P., Brazill, R.L., 1981. An Assessment of A-C and D-C Potential System for Monitoring Fatigue Crack Growth. In Fatigue Crack Growth Measurement and Data Analsis, Philadelphia, Pa: American Society for Testing and Materials, 103-119.

Wilson, W.K., 1970. Stress intensity factors for deep cracks in bending and compact tension specimens. Engineering Fracture Mechanics 2, 168-171.

Zhai, T., Xu, Y.G., Martin, J.W., Wilkinson, A.J., Briggs, G.A.D., 1999. A Self-aligning Four Point Bend Testing Rig and Sample Geometry Effect in Four-point Bend Fatigue. Internatioal Journal of Fatigue, 889-894.

Chapter 4 Characterisation of LSP+FOD and early fatigue crack growth

4.1 Introduction

Optical studies to characterise the morphology of the impact damage and influence of crack initiation for spherical ballistic FOD impacts on diamond cross-sectioned specimen geometries were carried out by (e.g. Bache et al., 2002; 2003; Martinez et al., 2002). Martinez et al. (2002) characterised these FOD impact sites by measuring the notch depth, loss of material at the notch, material shear, material folding over the leading edge, embedded glass fragments and microstructural damage. However, the cubical projectile was considered to be more representative of "worst case" damage seen in service. The objectives of the following chapters are to examine the effects of FOD under complex loading conditions on the LSP treated specimens. Specifically, cubical head-on and 45° FOD impacts on laser shock peened Ti-6Al-4V aerofoil specimens were characterised. Typical damage characteristics and their role in crack initiation and early crack growth under simulated service loading conditions were examined. The results were compared to specimens without LSP treatment (Ding et al., 2007a; Hall et al., 2008) and with spherical FOD impacts (Ruschau et al., 2001; Ritchie et al., 1999; Martinez et al., 2002; Bache et al., 2002; 2003).

4.2 Results and discussion of optical FOD damage characterisation

To characterise FOD damage features and fracture surfaces post fatigue testing, a scanning electron microscopy (SEM) study was carried out using a JEOL JSM-6100 SEM. Indents from both head-on and 45° FOD impacts were examined at various orientations, and at selected stages of the fatigue crack growth process. Specifically, characterisation was carried out for a) post FOD but prior to fatigue testing, b) after early fatigue crack growth and c) after fatigue fracture. The last two steps provide insight into the location and the nature of the crack initiation and early crack growth associated with the FOD damage features.

4.2.1 Characterisation of FOD damage for 0° and 45° FOD impacts

Damage due to 0° (head-on) and 45° FOD impacts were characterised using standard optical and scanning electron microscopy with the main features identified as: notch produced by the impact, loss of materials (LOM), material shear and material folding over the leading edge, evidence of heat formation, shear bands and microcracks. Whilst material shear seems to be common in both impacts, LOM seems to be more substantial in 45° impacts as opposed to material folding/pile-up found commonly in head-on impacts. The details are discussed as follows.

Impact notch

For head-on impacts, a V-notch was obtained on the leading edge, similar to those observed in (Ding et al., 2007a). The projectile was bounced back after the impact, causing materials folding and piled up over the leading edge. A typical morphology for such an impact site is shown in Fig. 4-1a. The notch depths were measured by suitably positioning the SEM stage to achieve a profile view of the notch depth on each side. There were some small differences in the notch depths measured on the two sides.

The average notch depth of the nine notches due to FOD at an average speed of 197m/s was 1.43mm. Preferred sites for crack initiation were reported (Ruschau et

al., 2001; Martinez et al., 2002) to occur at the deeper of the two notches for spherical projectiles. This is consistent with our observation.

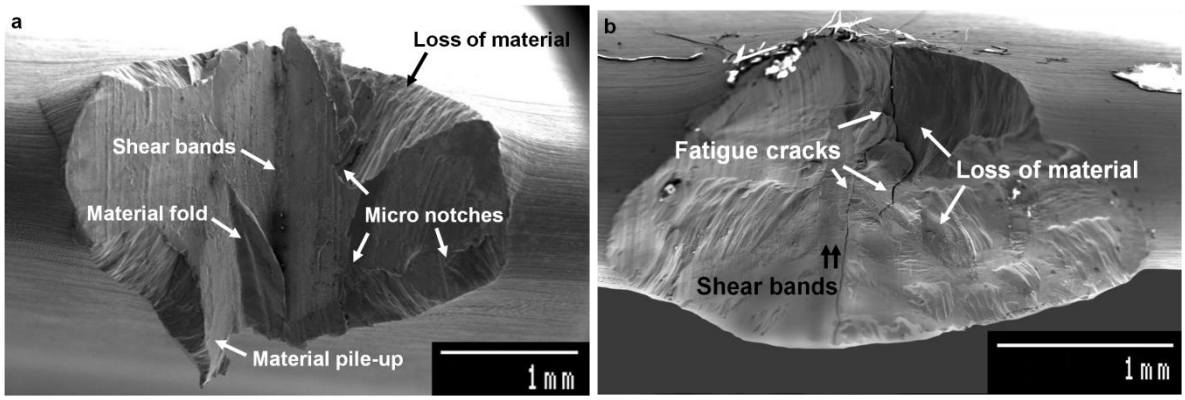

Figure 4-1 The overall morphologies of the impact site for a) head-on impact, b) 45° impact, with typical characteristics including material pile-up, loss of materials (LOM) with material shear, folding and micronotches.

For 45° impacts, however, the projectile "sheared" off part of the leading edge during the impact, creating a notch with the depths vary significantly at the entrance and the exit of the projectile (Fig. 4-1b). The notch depths were measured again on both sides using an optical microscope. The average notch depth of 9 specimens shot at an average impact velocity of 245m/s was 1.69mm for the deeper notch and 0.62mm for the shallower notch, respectively. An average notch depth might also be estimated by the distance from the leading edge to the centre of the notch root, this gives an average value of 0.78mm. The exact values of impact velocity and notch depth for each impact can be found in the Appendix B. The notch angle was measured after the FOD impact also, and an average impact angle of 40° was obtained, a deviation of 5° from the nominal impact angle of 45°.

Loss of material (LOM) and material shear

LOM and material shear from the surface of the notch are evident in all FODed specimens (Figs. 4-1a, 4-2b). Fig. 4-1a shows an overview of the impact site of a head-on impact. Material shear appears to be present in the form of shear dimples and shear lips (Fig. 4-2b). LOM is mostly found near the edges of the notch (Fig. 4-1a). A quantitative measure of LOM might be carried out by weighing the specimen before and after the FOD impact, but this was not attempted in the present study. LOM

may be associated with microcracking (Fig. 4-2a), although LOM alone did not appear to affect the fatigue strength (Martinez et al., 2002). The area near LOM may be favourable for crack initiation, as a result of sharp edges and irregularities associated with LOM.LOM is more severe in 45° impacts mostly through material shearing. Fig. 4-1b shows an overview of such an impact site. LOM and shear bands were evident on all notch edges as well as on the notch surface and the notch root (Figs. 4-1b, 4-3c). The direction of the shearing is indicated by the shear bands and shear lips, as shown (Figs. 4-1b, 4-2b, 4-3c).

Material folding and heat formation

For head-on impacts, LOM is often associated with material folding over the leading edge (Fig. 4-1a), as opposed to 45° impacts, where LOM is often associated with material shearing (Fig. 4-1b). Material folding occurred in all head-on FODed specimens, and this can be seen in the Figs. 4-1a, 4-3a and 4.4a-d. Material folding is a result of material pile-ups due to the cubical impact, where the material was forced ahead of the impacting cubical edge. The forced material was partly sheared off at the beginning of the impact, or piled-up preferably along the edges (Figs. 4-1a, 4-3a) or near the root of the notch (Figs. 4-1a, 4-4a, b). The folded and piled-up material often created sharp notches, as shown in Figs. 4-1a and 4-4a, b, giving rise to stress concentrations.

The folded materials appear to be smooth, suggesting "fused" layers of materials due to the heat associated with the high speed FOD. In Fig. 4-2c, some "droplet" structures (Engel and Klingele, 1974) can be observed adjacent to the area of incipient melting around the 'cleavage' surface, an observation consistent with that reported in (Engel and Klingele, 1974). Material folding in 45° impacts was not as evident as that in the 0° impact, although folding over the leading edge at the exit location of the projectile can sometimes be seen. An analysis of a 45° FOD impact via a high-speed camera suggests that this folding is a result of the rotational movement of the projectile occurred in the sample during the impact. No folding or material pile-up was found in the notch root.

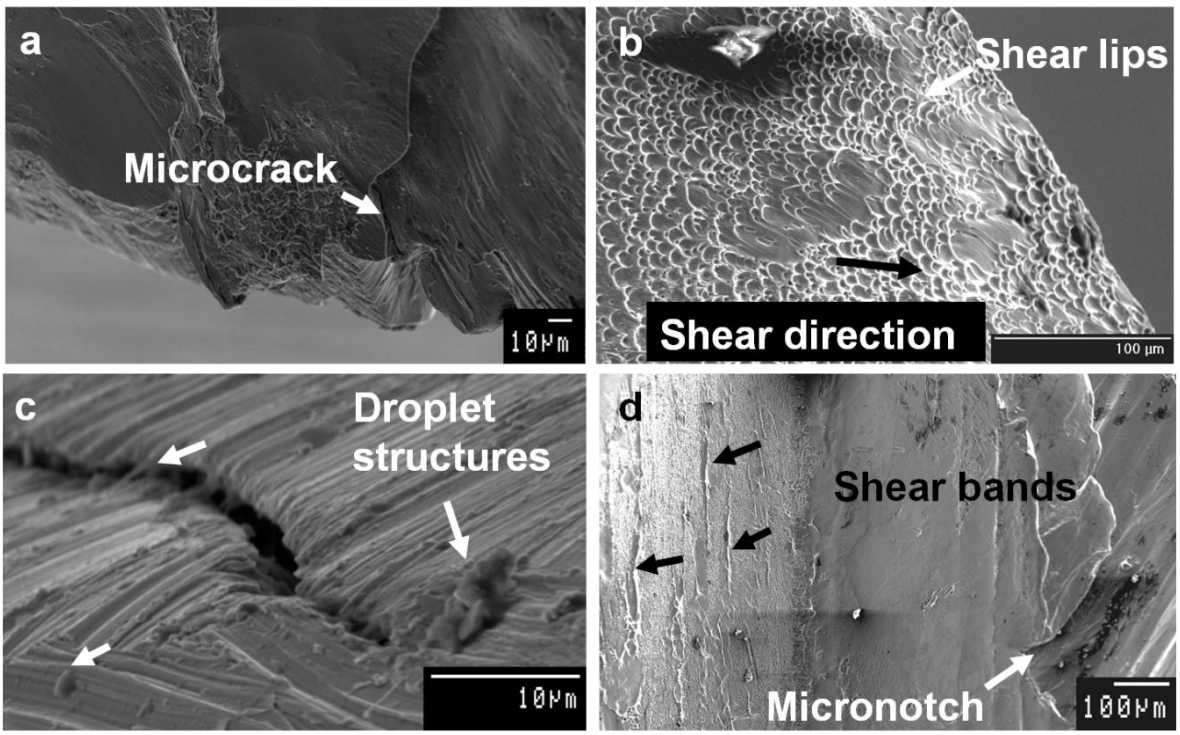

Figure 4-2 Scanning electron micrographs of a "head-on" impact site, details of the deformation, a) a microcrack formed at the crater rim after the FOD impact, b) shear dimples as a result of material shear associated with the loss of materials, c) "droplet" structures due to the heat generated during the impact, d) Intense shear bands and micronotches at the root of a head-on impact notch.

Shear bands and microcracks

Shear bands are often observed on the notch surfaces (Figs. 4-1a, b), as a result of high shear stresses generated during impacts. As shown earlier, FOD impacts elevated the local temperature on the notch surface, which lead to plastic instability, and may introduce local strain mismatches, leading to shear deformation, shear bands and microcracks on the surfaces of the FOD notch (Fig. 4-2d). A shear band is the result of strain localization attributed to plastic instability arising from thermal softening during adiabatic or quasi-adiabatic deformation (Meyers and Pak, 1986), as is the case here. Micro-notches, as identified in (Peters and Ritchie, 2000), are observed due to plastic flow and LOM (Figs. 4-1a, 4-2d, 4-6a, b). Material pile-ups and foldings near the crater rim can also result in sharp notches (Figs. 4-1a, 4-4a, b) and microcracks (Figs. 4-2a, 4-4a). A typical microcrack length (as shown in Fig. 4-2a) is about 40μm.

The edge of the impacting cube created a groove in the FOD notch. Within this groove a high density of multiple and textured shear bands along the impact direction can be found, as shown in Figs. 4-1b, 4-3c, d. These shear bands, termed as adiabatic shear bands (ASB) (Peters and Ritchie, 2000; Peters and Ritchie, 2001; Martinez et al., 2002; Murr et al., 2009; Meyers and Pak, 1986), are characterized by localized shear deformation. Previous investigations on Ti-6Al-4V alloy showed that in the vicinity of the shear bands a high density of dislocations and deformation twins were observed (Peters and Ritchie, 2000; Meyers and Pak, 1986). Shear bands seem to be associated with the microcracks along the groove created by the impacting edge of the cube (Figs. 4-3c, d).

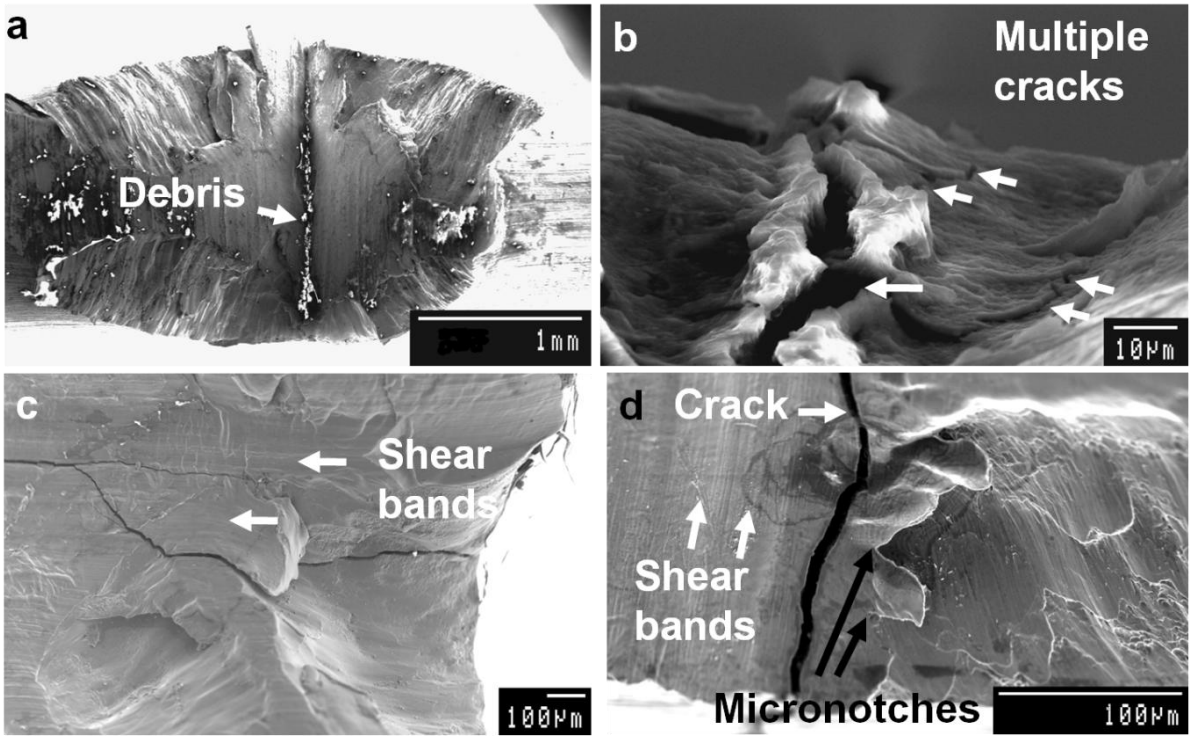

Figure 4-3 Scanning electron micrographs of the impact site post FOD and fatigue testing, a) debris near the root of the head-on impact notch, possibly due to fretting fatigue, b) multiple fatigue cracks under the debris in the notch root of a head-on impact sample shown in a), c) Material shear and multiple fatigue crack growth on different planes in a 45° impact notch, d) Micro-notches due to material shear and LOM, as well as multiple, textured shear bands in a 45° FOD notch.

In summary, typical features due to FOD impacts are listed in Table 1 (Page 82). The direction of the incident may be mainly responsible for the occurrence of a particular

damage feature, although the difference in the average impact speeds might also contribute. Generally, shear bands are common to both types of impacts, which may be mainly responsible for the multiple crack initiations. Material folding and pile-up are predominantly observed for head-on impacts, as opposed to LOM due to shearing, typically found in 45° impacts.

The head-on impact with an average velocity of 197m/s created an average notch depth about 1.43mm, whilst an average of notch depth of 0.78mm was found for 45° impacts at 245m/s. A direct comparison of these values may not be appropriate due to the different sizes of the cube used (3.2mm for head-on; 4.8mm for 45°) and, perhaps more critically, the impact angle in which the impact was executed (Ruschau et al., 2001; Thompson et al., 2001; Martinez et al., 2002; Bache et al., 2003). The deformation and notch depth are related to the contact surface between the projectile and the leading edge of the specimen. As the leading edge of this specimen is an elliptical-shaped, the contact surface between the projectile and the specimen is path-dependent. Specifically, in 45° impacts, the notch depth may be controlled by adjusting the overlap of the projectile edge relative to the leading edge to achieve a desired notch depth.

4.2.2 Characterisation of early crack growth due to FOD of 0° and 45° impacts

The specimens were fatigue tested post FOD characterisation, and some were examined using the SEM after the crack initiation detected but before the fatigue fracture, then fatigue tested until fracture. Evidence of fretting fatigue was observed (Fig. 4-3a) for samples experienced head-on impacts, but not in samples impacted at 45°. Some of the samples were broken open post testing and the fracture surfaces were examined under the SEM, where the micrographs of the same areas obtained prior to fatigue testing (Figs. 4-4a, b) are compared with those taken post fatigue testing (Figs. 4-4c, d). Possible crack growth patterns are also drawn (Fig. 4-5), based on fractography and surface replica measurement at regular intervals during testing.

Crack initiation sites

Crack initiation usually occurred at the deeper of the two impact notches for most of the samples, for both 0° and 45° impacts. Micro-notches due to the material pile-up/folds appear to the preferred crack initiation sites for samples impacted head-on (Fig. 4-4); whilst material shear and shear bands (Figs. 4-1b, 4-3c, d) seem to be more relevant in crack initiation and growth post 45° impacts.

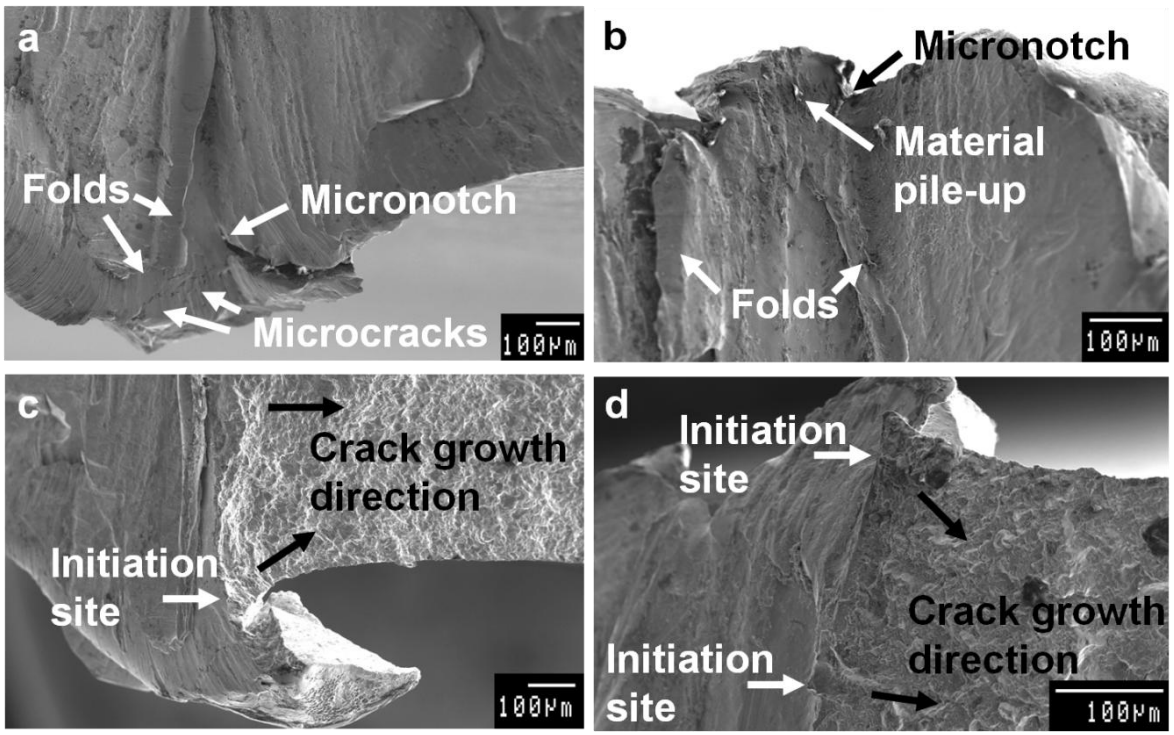

Figures 4-4 The fracture surface of a sample post a head-on impact pre- (a, b) and post- (c, d) fatigue testing, a) Material pile-up and folding over the leading edge created a sharp micronotch and microcracks, b) Material folds and pile-ups occurred near the rim of the FOD notch creating a micronotch, c) The sharp notch due to FOD (a) served as a crack initiation site from which crack growth detected (post testing); black arrows indicate crack growth direction, d) Two crack initiation sites due to material pile-ups and material folds identified (post testing); black arrows indicate crack growth direction.

For both cases, multiple crack initiations were observed, nucleating from the impact rims and near the root of the impact notch. For head-on impacts, damage features such as LOM, pile-up and folding resulted in stress concentrations where crack initiations usually occurred. Crack initiation also occurred in the notch root near the mid-plane, where a decreasing compressive residual stress field due to LSP together

with high constraint near the notch root provide favourable conditions for crack initiation (Greenacre et al., 2005). The evidence of fretting fatigue and multiple crack initiation and growth may be observed in Figs. 4-3a and b, where fretting debris accumulated mainly near the notch root. Multiple crack growth can be observed through the debris, which was confirmed by post testing fractography. It appears that the particles are loose, a result possibly due to fretting fatigue under the cyclic loads and increased crack closure effects due to the residual stresses under a combined action of LSP treatment and FOD impact. The distribution of the debris at the notch root seems to be uneven, with more debris found on the side where the cracks initiated.

Crack initiations for 45° impacts generally occurred near the edges of the FOD notch, and tended to grow, in the early stages, on multiple planes in the gauge area of the specimen (Figs. 4-1b, 4-3c). However, surface damages such as LOM, folding or micro-notches do not appear to affect the crack initiation as much as in the cases of head-on impact. It seems that, for 45° impacts, shear bands along the root of the notch created by the cubical edge are mainly responsible for crack initiation and growth (Figs. 4-1b, 4-3c, d).

Crack growth pattern

Figure 4-5a shows the fracture surface of a sample with the FOD notch (head-on impact) to the left and fatigue crack growth to the right. It is possible that the micro-notches due to the material pile-up (Figs. 4-4a, b) as well as fretting fatigue in the notch root (Figs. 4-3a, b) gave rise to crack initiation sites (as indicated) and subsequent crack propagation.

Figure 4-5b shows the fracture surface of a failed specimen post 45° impact and fatigue loading. For 45° impacts, multiple crack initiation and growth are mostly from shear bands. Figure 4-1b shows two main cracks in the notch root region, initiating possibly from the notch rim where material shearing occurred. Figure 4-3c shows the coalescence of two cracks in the middle of the notch root, seemingly growing on two separate planes. The crack on the left side (Fig. 4-3c) seems to grow along the groove in the presence of a high density of multiple shear bands (Figs. 4-

1b, 4-3c). The micro-notches (Fig. 4.3d) due to LOM at the crater rim seem less damaging for crack initiation than the shear-bands for samples impacted at 45°.

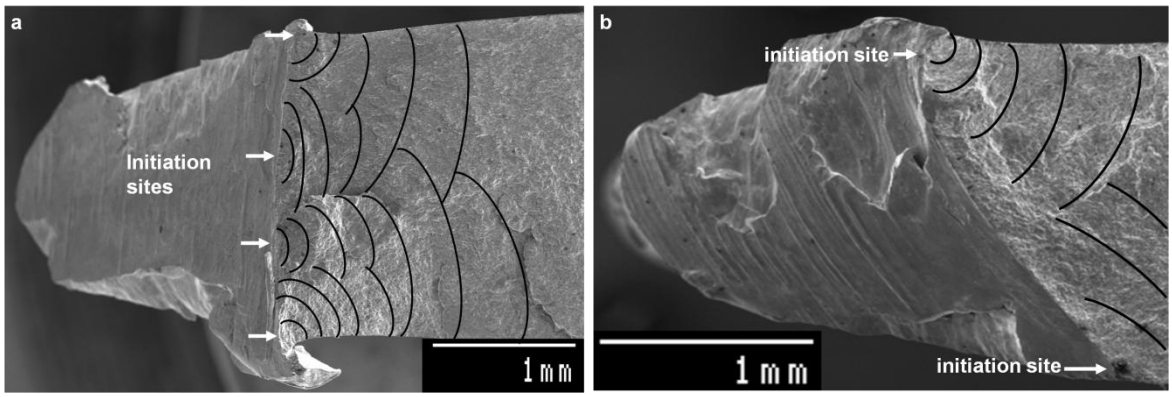

Figure 4-5 Possible crack initiation sites and estimated crack growth paths post FOD. a) For a head-on impact (FOD crater, left; fracture surface, right), arrows indicate the possible crack initiation sites; crack fronts are also estimated based on the fatigue striation patterns and surface replica measurements, b) for a 45° impact (FOD crater, left; fracture surface, right), crack initiation sites are indicated with possible crack growth patterns.

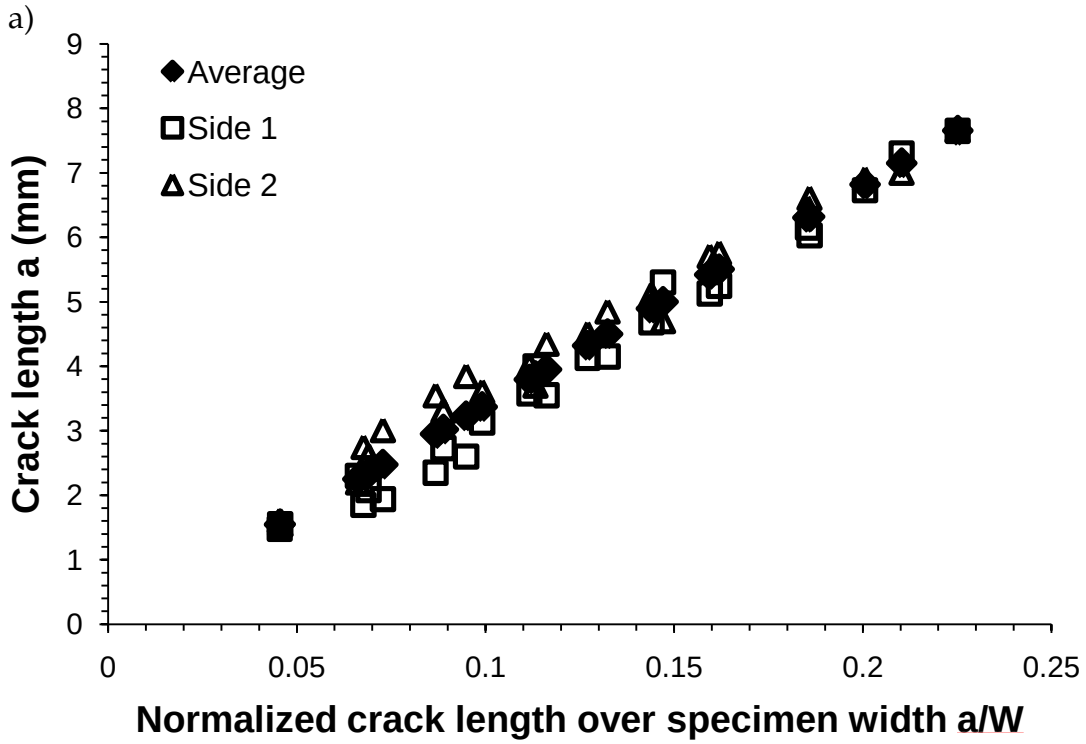

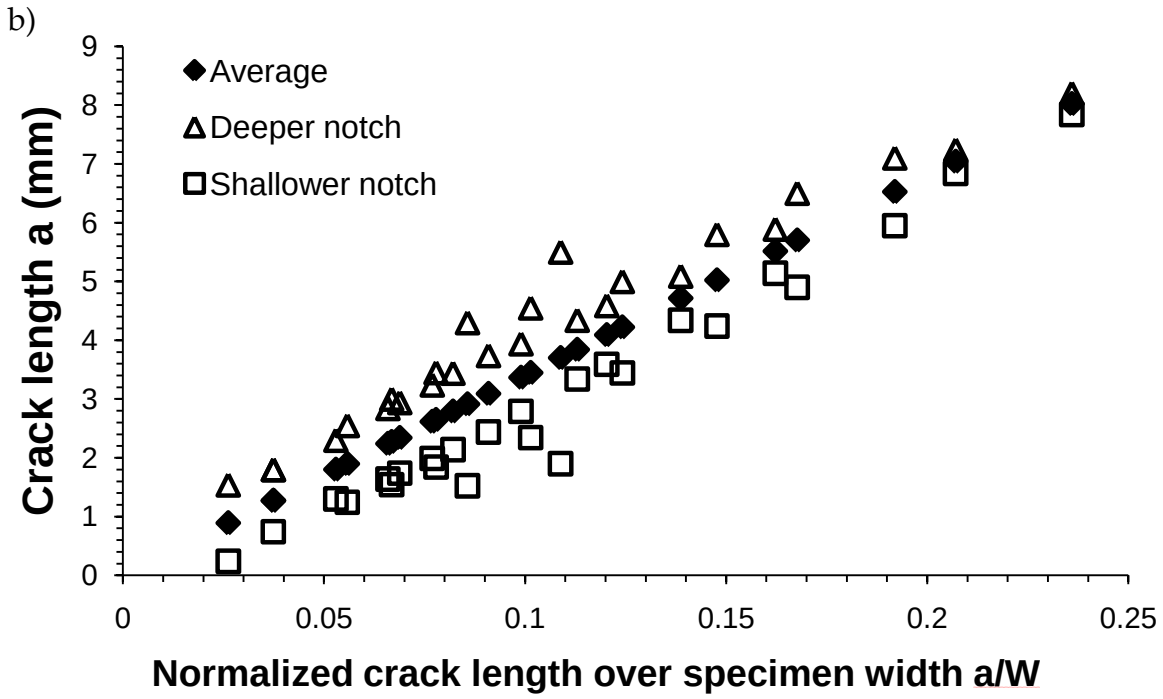

Figure 4-6 Fatigue crack growth patterns as measured by surface replicas, showing the development of surface cracks, a) for a 0° FOD impact, b) for a 45° FOD impact.

Figure 4-6 presents the projected crack growth patterns as measured by surface replicas during testing for two samples, impacted head-on and at 45 degree, respectively. It seems that, whilst uneven crack growths are common for both cases, possibly due to the preferential crack initiation and growth at one of the notch edges, the crack front in the sample post 45° impact experienced more uneven crack growth due to the FOD notch shape that gave rise to a higher crack driving force at the deeper notch than that at the shallower notch. The scatter band in 45° samples is also significantly larger than that in head-on samples.

Table 1 summarises the key FOD and subsequent cracking features in both head-on and 45° impacted samples. It seems that loss of materials, material folding and pile-up is more typical for head-on impacts and these FOD features, together with fretting fatigue, may be responsible for crack initiation and growth post FOD; whilst for 45° impacts, shear bands associated with the shearing action and LOM during impact are more relevant to crack initiation and growth.

Table 1 Comparison of the FOD features for 0° and 45° FOD impacts observed using SEM

	0 impact	**45 impact**
LOM	Predominantly at rims of notch surface	All over notch surface and notch root
Folding over LE	Significant	Insignificant
Material pile-up	Yes	No
Shear-bands	Yes	Yes
Microcracks	Yes	Yes
Multiple crack initiation	Notch root	Notch root
Fretting fatigue	Yes	No
Crack growth	Multiple crack growth from the notch root	Multiple crack growth from the edges of the notch

4.2.3 Comparison of head-on FOD damage to samples with and without LSP treatment

In our previous work (Hall et al., 2008) a simplified aerofoil specimen of Ti-6Al-4V alloy untreated with LSP was used to study the fatigue crack growth behaviour post FOD impacts. FOD was simulated by firing a 3mm cube head-on the aerofoil specimens at a velocity of 200m/s, and then tested under a combined LCF and HCF as well as LCF only and HCF only loading conditions. More severe deformation during FOD impact was experienced in the form of material pile-up at the crater rims but less LOM was observed. Although a direct comparison between the specimens with and without LSP treatment could not be carried out due to the slight difference in the geometry of the leading edge and the projectile dimension, it seems

that the untreated material is more ductile compared to the LSPed material. The LSPed material seems to be stiffer and more resistant to deformation upon FOD impact than that untreated material, resulting in less extensive overall deformation. This observation is supported by investigations of Nalla et al. (2003) and Zhang et al. (2010), both found that LSP can increase the hardness near the surface by more than 10%. This may explain the more pronounced distortion of the leading edge with material pile-up and folding in the untreated specimen, compared to more LOM in the LSPed samples.

Although microstructural changes due to LSP treatment could not be revealed by standard optical and SEM methods, TEM observation (Ruschau et al., 1999) showed high dislocation densities in the LSP-processed region, suggesting that a LSP process does produce microstructural changes at sub-gain level. Nevertheless there seems to be evidence of smeared surface features close to the crack tip, possibly due to the high compressive stresses generated through the LSP treatment. It was argued (Ruschau et al., 1999) that such an advantage diminishes at a higher R, this seems to be consistent with the current results.

4.2.4 Comparison of cubical and spherical impacts

For spherical projectiles, the forms of the FOD damage were found to depend on the impact velocity (Peters and Ritchie, 2000, Peters and Ritchie, 2001). At velocities above 250m/s, a pronounced pile-up of materials was evident near the crater rim; additionally, circumferentially orientated shear bands were also seen emanating on the surface of the impact crater; whilst these were not apparent for impacts at 200m/s. For an impact velocity of 300m/s, plastic flow in materials near the crater rim resulted in multiple micro-notches and microcracking, features unseen for impacts at velocities below ~250m/s. Similarly damage features attributed to the impact energy were also reported by Bache et al. (Bache et al., 2003; Bache et al., 2002).

Microcracks of sizes between 2-25μm were found (Peters and Ritchie, 2000) in samples subjected to spherical impacts at a velocity of 300m/s, whilst none at a velocity below 250m/s. In the current study microcracks of ~40μm were found in samples shot at an impact speed of 200m/s, indicating that cubical impacts are more damaging than spherical impacts. In addition, damage characteristics such as intense shear bands and microcracking were found only at higher impact velocities (>250m/s) for spherical impacts, whilst these features were observed at a lower velocity (200m/s) for cubical impacts. This seems to suggest that the damage characteristics depend not only on velocity (Peters and Ritchie, 2000; Bache et al., 2002) but also on the projectile shapes. To illustrate the elevated stress due to the presence of a notch, the stress concentration factor K_t may be used. K_t is the ratio of the peak stress at the notch and the nominal average stress in the body. For a v-notch created by a cubical projectile, the stress concentration at the root of the notch is greater than that under a spherical impact for an impact speed of 200m/s (K_t=5.7 for cubical impact vs. K_t=1.2 for spherical impact (Leven and Frocht, 1953)). Micro-notches created due to the material pile-up and folding are potential sources of crack initiation and growth upon subsequent fatigue loading, particularly if they are favourably orientated with respect to the applied load axis. In the current cases, most of the microcracks and shear bands near the root of the notch served as the sources for multiple crack initiation and growth.

Although crack growth behaviour under impact of different orientations has not been reported previously, impact at an angle other than head-on was demonstrated to be more damaging (Ruschau et al., 2003; Martinez et al., 2002). Impacts that result in the formation of craters are found to absorb more energy than those that produce chipped or fractured notches of the same geometry, while chipping, as a result of angled impacts, was found to be more detrimental to high cycle fatigue strength (Ruschau et al., 2003). This seems to be consistent with the present observation, in that the early onset of crack growth observed in 45° samples seems to be associated with the more severe damage sustained during this type of impacts.

4.3 Conclusions

Experimental studies on damage of generic LSPed aerofoil specimens subjected to high speed head-on and 45° impacts, and subsequent fatigue testing under low cycle, high cycle and a combined low and high cycle fatigue loading seem to suggest:

1. For head-on impact, multiple crack initiation and growth seem to be attributed to micro-notches due to material pile-up/folding and fretting fatigue.
2. For 45° impact, damage is characterised primarily by material shear and shear bands, which seem to be responsible for early multiple crack initiations, often on multiple planes with respect to the loading axis.
3. The FOD damage due to cubical impacts is more severe and more detrimental to the subsequent fatigue crack initiation and growth than that sustained in spherical FOD impacts at a given speed.

4.4 References

Bache, M.R., Bradshaw, C., Voice, W., 2003. Characterisation of foreign object damage and fatigue strength in titanium based aerofoil alloys. Material Science and Engineering A354, 199-206.

Bache, M.R., Evans, W.J., Voice, W., 2002. The resistance to impact damage and subsequent fatigue response of two titanium alloys. Material Science and Engineering A333, 287-294.

Ding, J., Hall, R.F., Byrne, J., Tong, J., 2007a. Fatigue crack growth from foreign object damge under combined low and high cycle loading. Part I: Experimental studies. International Journal of Fatigue 29, 1339-1349.

Engel, Klingele, 1974. Rasterelektronenmikroskopische Untersuchungen von Metallschäden, Köln, Gerling Institut für Schadenforschung und Schadenverhütung, p. 141.

Greenacre, P., Schofield, J., McElhone, M., Rugg, D., Lawson, M., 2005. Evaluation, Control and Prevention of High Cycle Fatigue in Gas Turbine Engines for Land, Sea and Air Vehicles (pp. 35-1 – 35-14). Meeting Proceedings RTO-MP-AVT-121, Paper 35. Neuilly-sur-Seine, France.

Hall, R., Byrne, J., Zhao, T., Tong, J., 2008. Influence of foreign object damage on fatigue crack growth of gas turbine aerofoils under complex loading conditions. Fatigue & Fracture of Engineering Materials & Structures 31, 386-397.

Leven, M. M., Frocht, M. M., 1953. Proc. Soc. Exp. Stress Anal., vol. 11, no. 2.

Martinez, C.M., Eylon, D., Nicholas, T., Thompson, S.R., Ruschau, J.J., Birkbeck, J., Porter, W.J., 2002. Effects of ballistic impact damage on fatigue crack initiation in Ti-6Al-4V simulated engine blades. Material Science and Engineering A325, 465–477.

Meyers, M.A., Pak, Han-Ryong, 1986. Observation of an adiabatic shear band in titanium by high-voltage transmission electron microscopy. Acta Metallurgica 34, 2493-2499.

Murr, L.E., Ramirez, A.C., Gaytan, S.M., Lopez M.I., Martinez, E.Y., Hernandez, D.H., Martinez, E., 2009. Microstructure evolution associated with adiabatic shear bands and shear band failure in ballistic plug formation in Ti-6Al-4V targets. Material Science and Engineering A516, 205-216.

Nalla, R.K., Altenberger, I., Noster, U., Liu, G.Y., Scholtes, B., Ritchie, R.O., 2003. On the influence of mechanical surface treatments – deep rolling and laser shock peening – on the fatigue behaviour of Ti-6Al-4V at ambient and elevated temperatures. Materials Science and Engineering A355, 216-230.

Peters, J.O., Ritchie, R.O., 2000. Influence of Foreign-object Damage on Crack Initiation and Early Crack Growth During High Cycle Fatigue of Ti-6Al-4V. Engineering Fracture Mechanics, 193-207.

Peters, J.O., Ritchie, R.O., 2001. Foreign-object damage and high cycle fatigue of Ti-6Al-4V. Materials Science and Engineering A319-321, 597-601.

Ruschau, J.J., John, R., Thompson, S.R., Nicholas, T., 1999. Fatigue crack nucleation and growth rate behaviour of laser shock peened titanium. International Journal of Fatigue, 199-209.

Ruschau, J.J., Nicholas, T., Thompson, S.R., 2001. Influence of foreign object damage (FOD) on the fatigue life of simulated Ti-6Al-4V airfoils. International Journal of Impact Engineering 25, 233-250.

Ruschau, J.J., Thompson, S.R., Nicholas, T., 2003. High cycle Fatigue limit stresses for irfoils subjected to foreign object damage. International Journal of Fatigue 25, 955-962.

Thompson, S.R., Ruschau, J.J., Nicholas, T., 2001. Influence of residual stresses on high cycle faigue strength of Ti-6Al-4V subjected to foreign object damage. International Journal of Fatigue 23, 405-412.

Zhang, X.C., Zhang, Y.K., Lu, J.Z., Xuan, F.Z., Wang, Z.D., Tu, S.T., 2010. Improvement of fatigue life of Ti-6Al-4V alloy by laser shock peening. Material Science and Engineering A527, 3411-3415.

Chapter 5 Evaluation of stress intensity factor (SIF) in a residual stress field

This section presents a study on the application of the weight function method and the finite element method to evaluate the stress intensity factor (SIF) K in the presence of residual stresses due to LSP and FOD. Experimentally measured primary one-dimensional residual stress distributions (Zabeen et al., 2010) were used in the analyses. The objective is to provide a modified SIF to consider the effects of residual stresses on SIF, and to utilise the modified SIF in the correlation of the fatigue crack growth data obtained from the present experiments. To evaluate the modified SIF, the results from the weight function and the finite element approaches were compared. A schematic flowchart is shown in Figure 5-1.

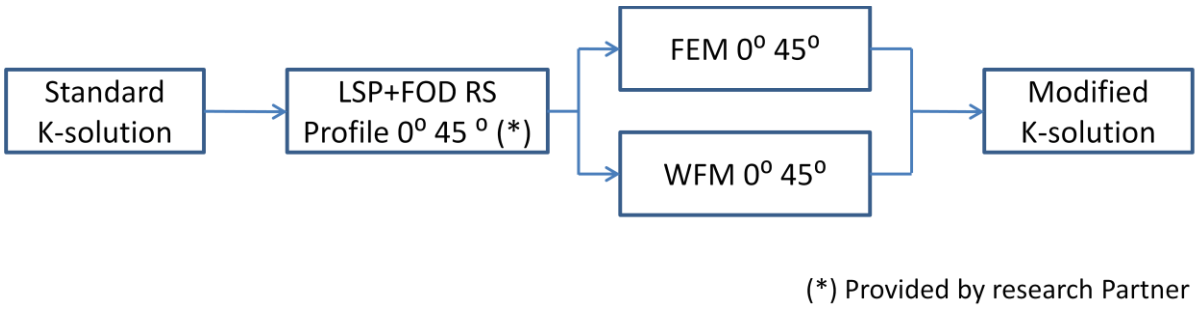

Figure 5-1 Schematic outline of Chapter 5 (* Zabeen et al., 2010).

5.1 Residual stress profiles

The residual stress profiles were obtained by our research partner, the Materials Science Centre at the University of Manchester, using X-ray diffraction (XRD) (Zabeen et al., 2010). Due to the differences in impact angles and notch depths, the residual stress distribution for each impact case was analysed separately. The longitudinal residual stress distributions resulting from the FOD 0° and 45° impacts along the perceived crack growth path are shown in Figure 5-2. The profiles were measured on the mid-plane of the uncracked specimen. About 900 individual measurement points were collected for each specimen at a step-size of 0.2mm and 0.1mm parallel and perpendicular to the leading edge, respectively, resulting in a gauge volume of $0.1\times0.2\times2mm^3$ (Zabeen et al. 2010).

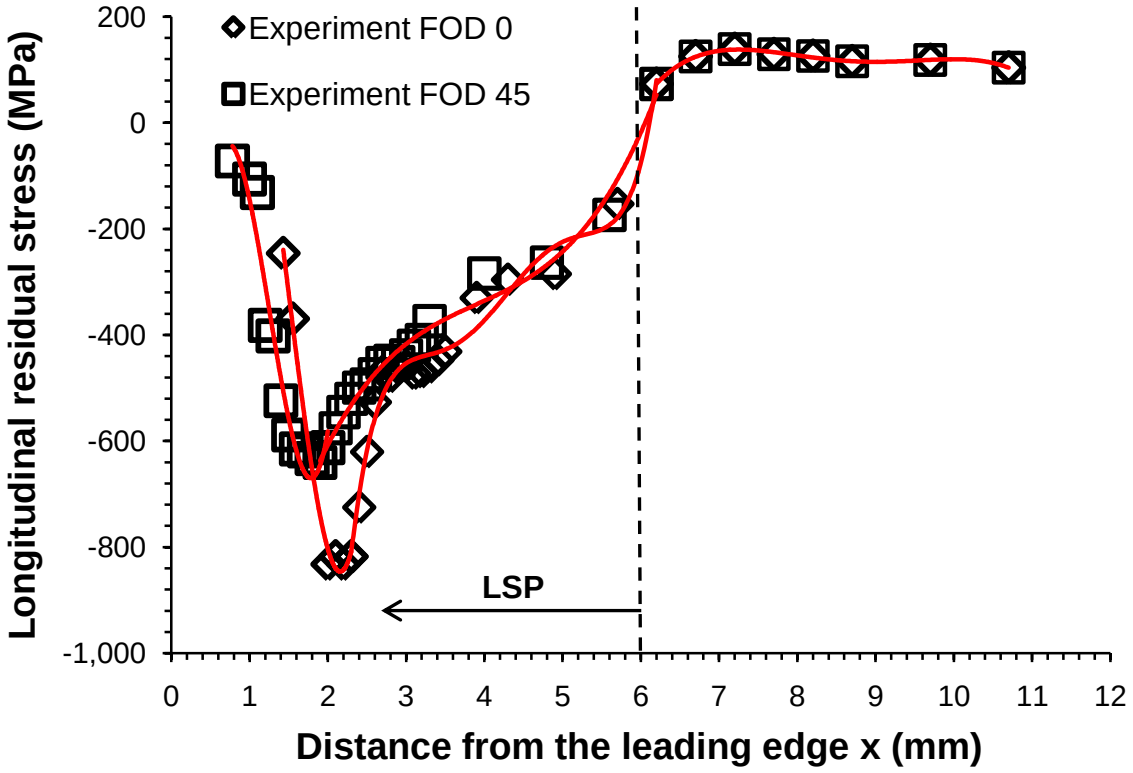

Figure 5-2 Longitudinal residual stress distributions for 0° and 45° LSP+FOD impacts.

The residual stress distribution in 0° impacts is overall more compressive compared to that in 45° impacts, especially near the notch tip where maximum compression is reached. After a distance of about 6mm from the leading edge, the residual stresses

for both cases return to the tensile zone and follow the same trend thereafter. It is noted that the residual stress distributions are not self-balanced over the distance considered.

To modify the SIF considering the residual stresses, the measured residual stresses are fitted (Bao et al., 2010) using polynomial forms. A high accuracy curve fitting, measured by the least square method R^2, for the residual stress profiles of each impact case was achieved by dividing each distribution into 3 sections. These segments were then fitted using high-order polynomial formulas, as shown in Figure 5-2. The basic form of the equations is:

$$\sigma_{res}(a) = A + B_1 \cdot a + B_2 \cdot a^2 + B_3 \cdot a^3 + B_4 \cdot a^4 + B_5 \cdot a^5 \tag{5-1}$$

where the polynomial parameters for each impact condition were fitted in segments and are presented in Table 5-1. The unit of length is in millimetres.

Table 5-1 The parameters of the polynomial curves fitted in segments for longitudinal residual stress distributions for 0° and 45° impacts.

		Parameters						
Impact	Segment	A	B_1	B_2	B_3	B_4	B_5	R^2
FOD 0°	$1.43 \le x \le 2.3$	1.753E03	5.192E03	-4.224E03	933.0	/	/	0.99
	$2.3 < x \le 6.2$	-34.27E03	42.36E03	-20.90E03	5.07E03	-602.6	28.14	0.98
	$6.2 < x \le 10.7$	-18.89E03	8.939E03	-1.560E03	119.8	-3.423	/	0.99
FOD 45°	$0.78 \le x < 1.9$	-1.926E03	5.659E03	-5.260E03	1.394E03			0.96
	$1.9 \le x \le 6.2$	-5.266E03	6.438E03	-3.520E03	966.0E03	-130.1	6.852	0.99
	$6.2 < x \le 10.7$	-18.89E03	8.939E03	-1.560E03	119.8	-3.423	/	0.99

5.2 Weight Function Method (WFM)

For an edge crack in an infinite plate, Kaya and Erogan (1980) and Wu and Carlsson (1991) provided weight function solutions for SIF. Wu and Carlsson (1991) provided discrete values for selected non-dimensional a/W values; whilst a closed-formed SIF solution was given by Kaya and Erdogan (1980). In this study, the closed-form SIF solution of Kaya and Erdogan (1980) was adopted. The weight function is difficult to solve due to its complex integral equations, hence MATLAB was used to calculate the weight function. In the edge-cracked 2D model, a residual SIF (K_{res}) may be calculated by integrating the weight function m(x,a) and the residual stress distribution $\sigma_{res}(x)$ acting on the crack length a, which is expressed as:

$$K_{res} = \int_0^a \sigma_{res}(x) \bullet m(x,a)dx \tag{5-2}$$

where

$$m(x,a) = \frac{2}{\sqrt{\pi a}} \bullet \frac{G\left(\frac{x}{a},\frac{a}{W}\right)}{\left(1-\frac{a}{W}\right)^{3/2}\sqrt{1-\left(\frac{x}{a}\right)^2}} \tag{5-3}$$

and

$$G\left(\frac{x}{a},\frac{a}{W}\right) = g_1\left(\frac{a}{W}\right) + g_2\left(\frac{a}{W}\right)\bullet\left(\frac{x}{a}\right) + g_3\left(\frac{a}{W}\right)\bullet\left(\frac{x}{a}\right)^2 + g_4\left(\frac{a}{W}\right)\bullet\left(\frac{x}{a}\right)^3 \tag{5-4}$$

$$g_1\left(\frac{a}{W}\right) = 0.46 + 3.06\cdot\frac{a}{W} + 0.84\left(1-\frac{a}{W}\right)^5 + 0.66\left(\frac{a}{W}\right)\left(1-\frac{a}{W}\right)^2 \tag{5-5}$$

$$g_2\left(\frac{a}{W}\right) = -3.52\left(\frac{a}{W}\right)^2 \tag{5-6}$$

$$g_3\left(\frac{a}{W}\right) = 6.17 - 28.22\left(\frac{a}{W}\right) + 34.54\left(\frac{a}{W}\right)^2 - 14.39\left(\frac{a}{W}\right)^3 - \left(1-\frac{a}{W}\right)^{3/2} - 5.88\left(1-\frac{a}{W}\right)^5 - 2.64\left(\frac{a}{W}\right)^2\left(1-\frac{a}{W}\right)^2 \tag{5-7}$$

$$g_4\left(\frac{a}{W}\right) = -6.63 + 25.16\frac{a}{W} - 31.04\left(\frac{a}{W}\right)^2 + 14.41\left(\frac{a}{W}\right)^3 + 2\left(1-\frac{a}{W}\right)^{3/2} + 5.04\left(1-\frac{a}{W}\right)^5 + 1.98\left(\frac{a}{W}\right)^2\left(1-\frac{a}{W}\right)^2 \quad (5\text{-}8)$$

The K_{res} solutions were calculated for both 0° and 45° cases and compared with those obtained from the finite element method.

5.3 Finite Element Method (FEM)

3D FE analysis requires detailed 3D residual stress distributions (Sansoz et al., 2001) as well as notch geometries, which was not considered in the current study due to the lack of 3D residual stress data and time constraint. A simplified 2D FE model was employed in the current study to calculate the stress intensity factors instead. A two-dimensional plane stress finite element model representative of the mid-section of the specimen was constructed, where the idealised geometry of the FOD notch was considered. Because of symmetry, only half of the aerofoil specimen was modelled and subjected to 4 point-bending, as shown in Figure 5-3a. Two FE models considering the two average notch depths (Chapter 4) for each impact angle were developed.

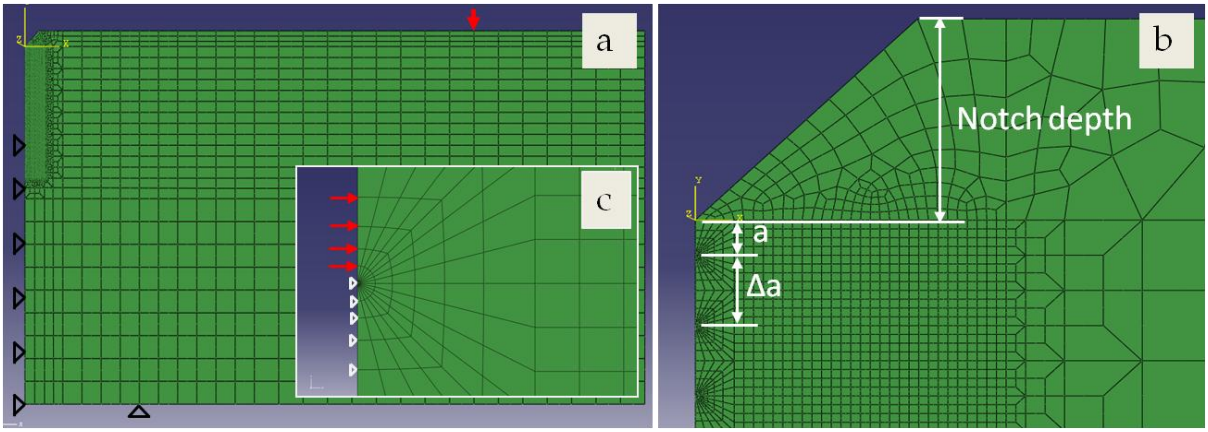

Figure 5-3 FE model in ABAQUS. a) 2D model, b) notch tip and refined mesh at the crack face, c) refined mesh showing singularity elements and DLOAD method.

Analyses were performed using the commercial FE code ABAQUS (6.8.2). 8-noded biquadratic elements were used and plane stress condition was assumed. The Young's modulus and Poisson's ratio are 103GPa and 0.34, respectively. The FE model was subjected to a remote longitudinal stress of 435MPa. A node-release technique, similar to that presented by Lei et al. (2000) and Bao and Zhang (2010), was used to simulate the growth of a crack. Crack propagation was simulated starting at a crack length from the notch tip of a=0.25mm and extended by an increment of Δa=0.5mm, as illustrated in Figure 5-3b. For each crack length the J-Integral with 5 different paths was obtained (Appendix 5.8). The SIF was then computed from the average J-integral value (excluding the first two contour integrals due to the singularity effects at the notch tip (ABAQUS, 2008)). This process was repeated until a final crack length of a=10.68mm for FOD 0º, and a=10.53mm for FOD 45º, was achieved.

To obtain an accurate SIF solution the mesh at the crack tip was refined using singularity elements at predetermined crack tips, with a typical element size of about 25μm, as shown in Figure 5-3c (Bao et al., 2010; Bao and Zhang, 2010; Sansoz et al., 2001). This element size was selected after conducting a convergence study with square elements at the crack tip, where the crack was extended incrementally by releasing nodes. The K values from the FE model without the consideration of the residual stresses were compared to those from the standard K solution (Rooke and Cartwright, 1976) (Chapter 2), with an error of 0.39% and 0.27% found for a model with crack tip element size of 0.01mm and 76E-06mm, respectively. The final crack tip element was chosen to be 0.01mm.

5.4 The FE model with residual stresses

Initial stress facility in the ABAQUS code is one method that is able to apply the residual stress as an initial condition prior to the analysis. This technique was used to modify a J-integral (Lei et al., 2000; Servetti and Zhang, 2009). Initial stresses can be applied by defining the relevant stress components at each integration point of the model. These stresses must be self-equilibrating, which usually requires an equilibrium step after the residual stress is applied. Cook et al. (2002) used the principle of superposition to apply the residual stress only on the surface of a crack face by using ABAQUS DLOAD subroutine. In this work, the experimentally measured residual stress field provided by our research partner was unbalanced (Figure 5-2). Thus the residual stress distribution was introduced using the ABAQUS DLOAD subroutine. The subroutine program introduced the residual stress field along the nodes of the crack face, which is illustrated in Figure 5-3c. Using this method, the residual stresses do not need to be balanced. Once the residual stress profile was introduced, the crack was grown by releasing the nodes along the crack path until a desired crack length was achieved.

5.5 Results and discussion

The results in SIF as obtained by the WFM and FEM for FOD 0° and 45° residual stress fields are presented here. The results of the two methods were compared and discussed. Polynomial fittings of the normalised K_{eff} for both impact conditions were also presented.

5.5.1 Comparison of SIF for FOD 0° and 45° impact conditions

The results of the effective SIF (K_{eff}) calculated from a superposition of the SIF for the initial residual stresses (K_{res}) and SIF for the applied stresses (K_{app}) are shown for FOD 0° in Figure 5-4 and for FOD 45° in Figure 5-5. The K_{app} were calculated by standard solutions presented early and the residual SIFs were obtained by the FE and the WF methods. The effective SIF was then taken as $K_{eff}=K_{res}+K_{app}$. The superposition principle was proposed by Nelson (1982) and Parker (1982), and subsequently used by Bao et al. (2010), Beghini and Bertini (1990) and Beghini et al., (1994). The SIF due to residual stresses, K_{res} is expressed as a negative qunatity and it is argued that, if the net SIF under a applied loading is negative, no stress singularity occurs. Unfortunately the principle of superpostion fails to take into account the possibility of crack mouth closure as expalined in (Wilks et al., 1993). However, if the applied loading is sufficient to render the crack fully open under the combined and residual stresses then the method of superposition is satisfactory.

The effective SIFs for both impact conditions follow overall the same trend and start well below the applied SIF, as the residual stress fields near the crack tip are in compression for both cases (Figure 5-2). With the decrease of the residual stresses towards their compressive minimum the effective SIFs decrease also towards their minimums, but without being negative. From this minimum the effective SIFs increase, following the trend of the residual stresses towards tensile (Figure 5-2). However, the effective SIFs do not merge with the applied SIF eventually. This may be due to the neglected 3-dimensional effects of the residual stresses by considering only the longitudinal residual stress. Previous studies also neglected residual stresses in dimensions other than that normal to the plane of potential crack growth

(Bao et al., 2010), although the magnitudes of the current longitudinal residual stresses are much higher than those from the previous studies. It is possible that the high magnitude tensile transverse residual stresses may have affected the overall equilibrium of the resultant stress distribution in the specimen, hence the accuracy of the K solution.

The general trends of the residual and the effective SIFs seem to be consistent with the theoretical concepts proposed by Parker (1982), Nelson (1982), Bouchard and Whiters (2006) for a given residual stress distribution. Recent studies on the evaluation of residual stress intensity factors in surface treated components also revealed similar trends (e.g. Bao et al., 2010; Servettti and Zhang; 2009; Krug et al., 2007; Reji et al., 2001). For both impact cases the normalized SIFs are valid for $0.03 < a/W < 0.32$ and their values are throughout positive. Compared to the applied SIF, for both impact cases, the onsets of early crack growth are mostly affected resulting in crack growth retardation due to the decrease of the effective K.

The initial SIF for FOD 45º impacts is higher than that for FOD 0º impacts, due to the slight difference in the longitudinal residual stress distributions (Figure 5-2). For a given applied stress, this might lead to an earlier onset for cracking in samples impacted at 45º than those impacted at 0º. Further, the normalized SIF for the FOD 0º reaches a greater minimum than that in the case of FOD 45º, due to the more compressive residual stress distribution of the former (Figure 5-2). This difference might affect the crack retardation during early crack growth period.

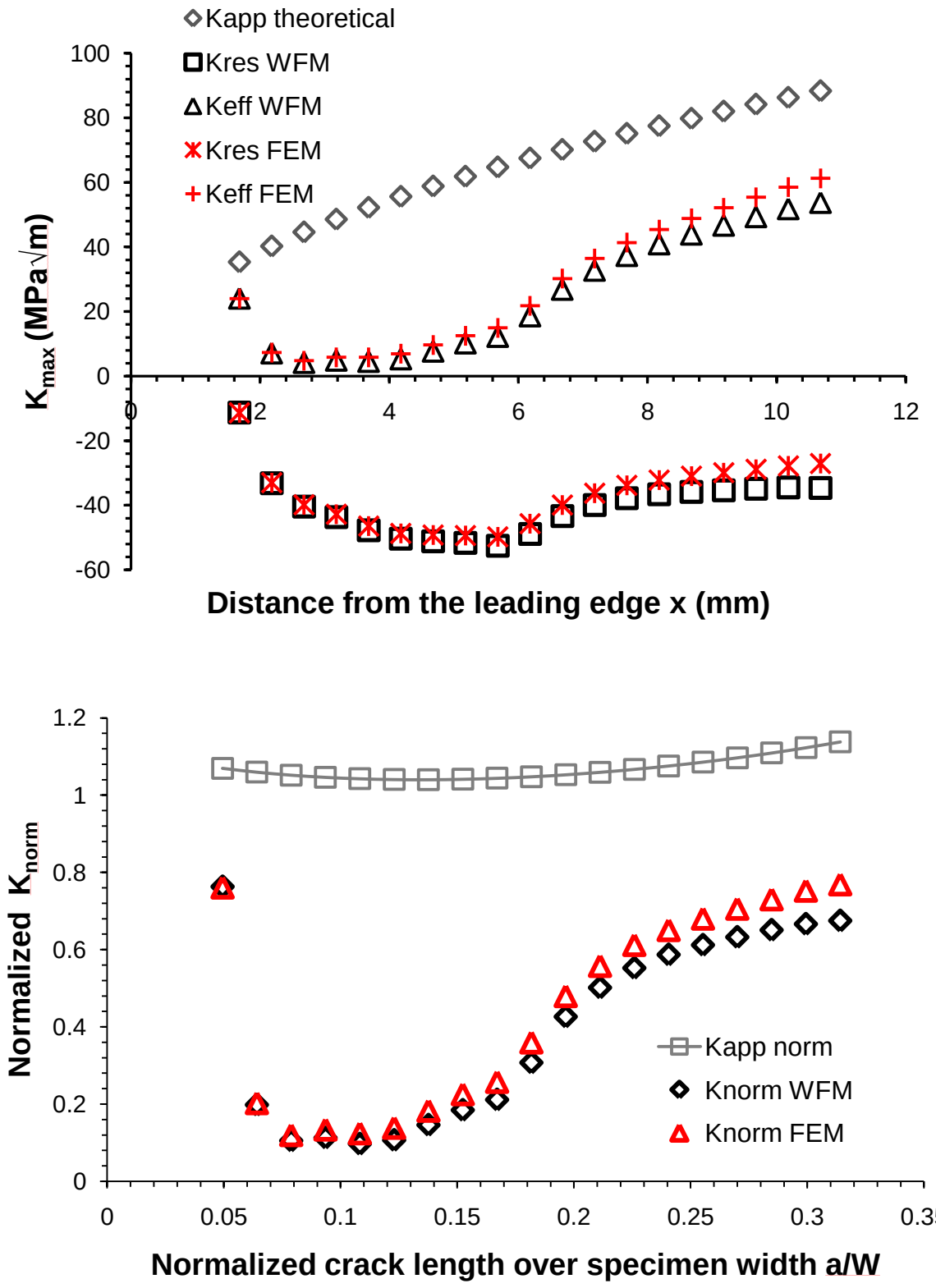

Figure 5-4 Comparison of SIFs for FOD 0° using the FE and the WF methods, a) The respective SIFs for the residual stress, the applied stress and the effective due to a superposition of the two, and b) the corresponding normalised SIFs.

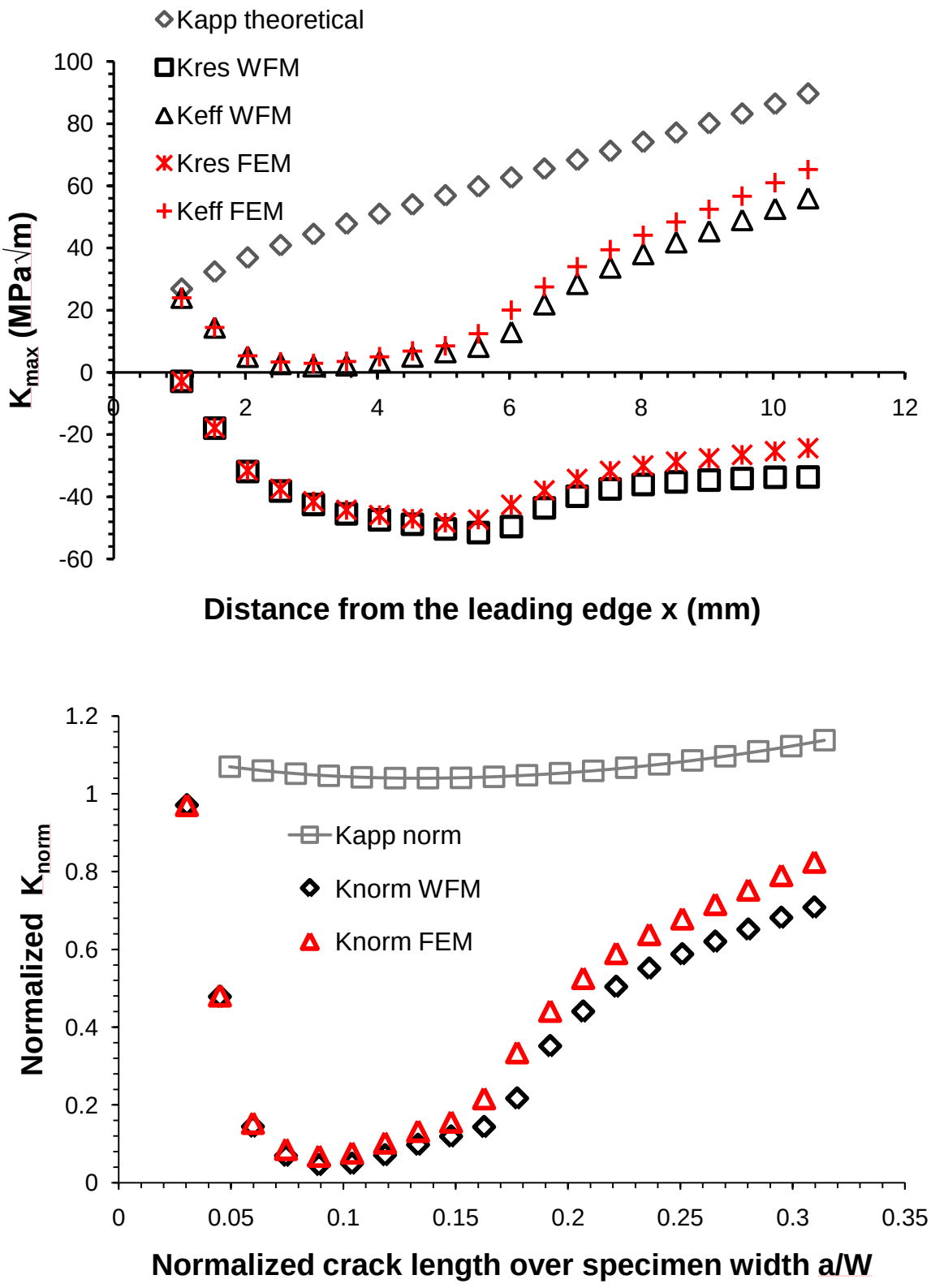

Figure 5-5 Comparison of SIFs for FOD 45° using the FE and the WF methods, a) The respective SIFs for the residual stress, the applied stress and the effective SIF due to a superposition of the two, and b) the corresponding normalised SIFs.

5.5.2 Comparison of WFM and FEM

Figures 5-4a and 5-5a show that the results of the K_{res} calculated by the FEM and WFM agree very well within a crack length of about 5mm from the leading edge. Above this crack length higher K_{res} values are obtained using the FE method than those obtained by the WFM. A similar trend in K_{res} solutions was reported in Bao et al. (2010) and in Liljedahl et al. (2010). Figures 5-4b and 5-5b show the comparison of the two approaches for both cases as a normalized K value.

Figure 5-6 shows the evolution of the percentage difference δ between the two methods and the normalized crack length over the specimen width (a/W) for both impact cases. For $a/W \leq 0.15$, the WFM and FEM results agree very well and the difference is within 5% for both cases. For $a/W \geq 0.15$ the difference between the two methods gradually increases with the extension of a/W. For a/W=0.31, the difference between the two methods reaches 21% for the FOD 0° case and 27% for the FOD 45° case.

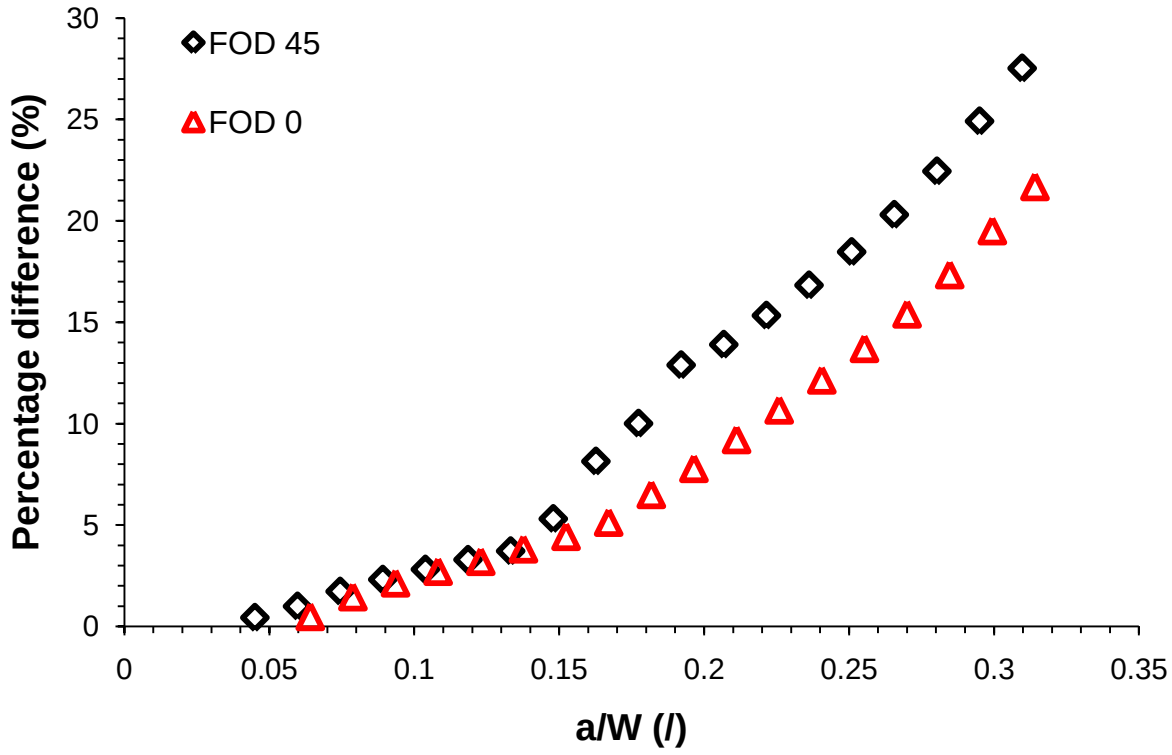

Figure 5-6 Comparison of percentage difference δ between the WFM and FEM of K_{res}.

Bao et al. (2010) and Liljedahl et al. (2010) compared K_{res} results obtained by both WFM and FEM methods for weld residual stresses and found that the results of both methods agree within 17% - 50% and 21% for $a/W \leq 0.6$, respectively. Their residual stresses were of much lower magnitudes than those of the current study. The range between σ_{max} and σ_{min} in Bao et al. (2010) was about 250MPa, whilst 340MPa in the case of Liljedahl et al. (2010). Both studies concluded that the FEM gives a more accurate evaluation when the crack length is longer ($a/W>0.6$). In the current study the difference between the two methods is within the range found in the literature for $a/W=0.3$. It should be noted that the residual stress range in this study is about 971MPa for the FOD 0º case and about 780MPa for the FOD 45º case, more than double the magnitudes from the previous studies. Both studies (Bao et al., 2010; Liljedahl et al. 2010) balanced their longitudinal residual stress artificially. The residual stress field in the current study was not artificially balanced though.

5.5.3 Shape function

For processing the experimental fatigue crack growth data, a modified shape function is needed incorporating the residual stress effects for each impact condition. The weight function was used to calculate such a function. This dimensionless shape function, Y (a/W), is related to ΔK as follows:

$$\Delta K = \Delta\sigma \times \sqrt{\pi \times a} \times Y\left({}^{a}/_{W}\right) \tag{5-9}$$

where ΔK is the range of the stress intensity factor, Δσ is the stress range, a is the crack length and Y (a/W) is the shape function which corresponds to the normalised SIF K_{norm} and is a function of the crack length over the specimen width.

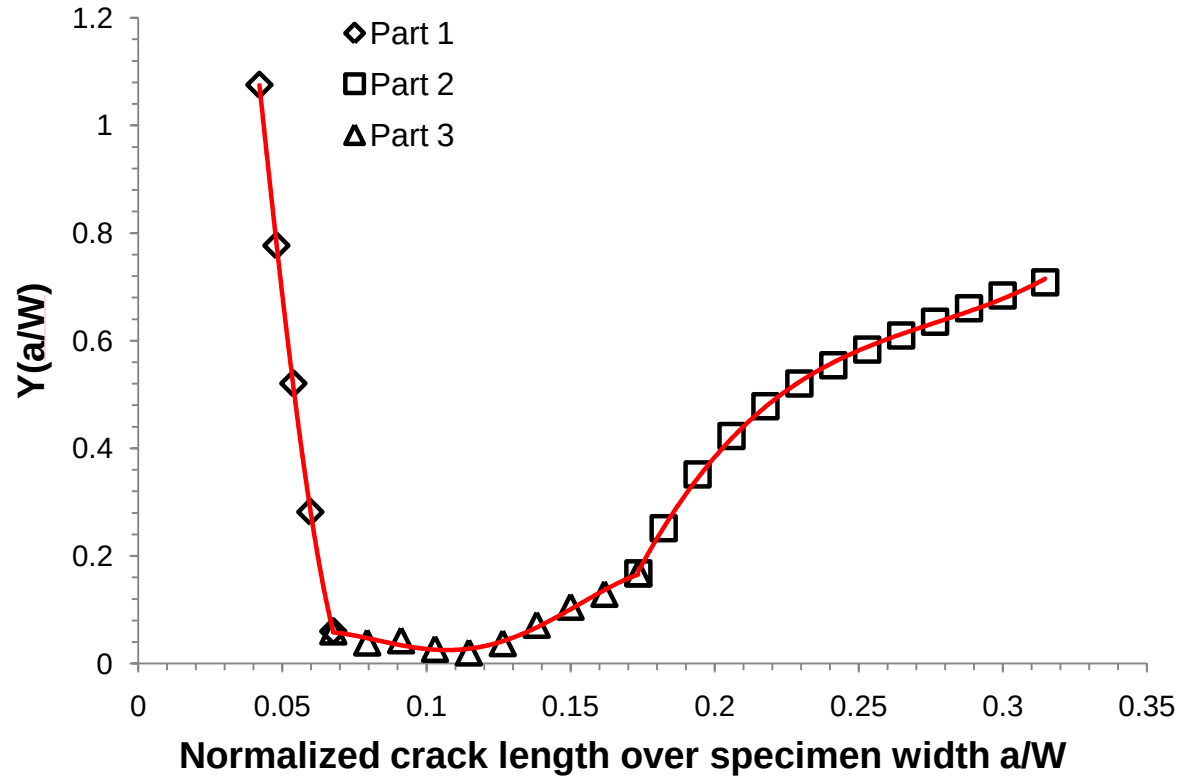

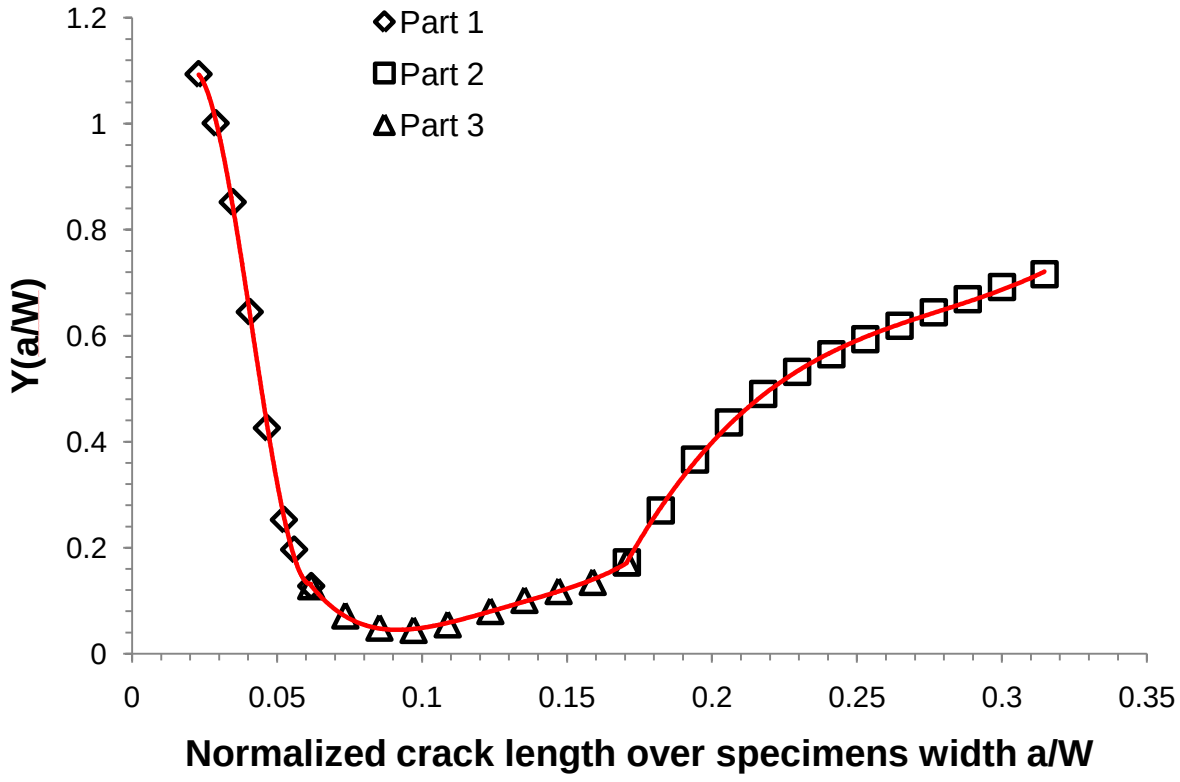

Figure 5-7 Results of shape function for normalized SIFs and distribution for a) FOD 0° impacts, and b) for FOD 45° impacts.

To obtain a high accuracy curve fitting, each curve was divided into 3 sections (Figure 5-7). These segments were fitted using a high-order polynomial form. The equation of Y (a/W) is determined as:

$$Y(a/W) = \mathrm{A} + \mathrm{B}_1 \cdot \left(a/W\right) + \mathrm{B}_2 \cdot \left(a/W\right)^2 + \mathrm{B}_3 \cdot \left(a/W\right)^3 + \mathrm{B}_4 \cdot \left(a/W\right)^4 \quad (5\text{-}10)$$

where the polynomial parameters for each impact condition are presented in Table 5-2. Important to note is that the mid part of both sections was fitted with a curve to reach a high R^2 but also to limit the order of polynomial so that just one minimum exists within the range. This minimum gives the reversal point at the minimum of the effective stress intensity factor.

Table 5-2 Constants in the polynomial curve fitting for the corresponding segments.

		Parameters					
Impact	Segment	A	B_1	B_2	B_3	B_4	R^2
FOD 0°	$0.042 \le a/W < 0.068$	2.818	-13.60	-1091	1018E01	/	0.99
	$0.068 \le a/W < 0.17$	-0.629	30.15	-461.5	2862	-6060	0.98
	$0.17 \le a/W < 0.315$	-5.269	60.50	-212.4	256.0	/	0.99
FOD 45°	$0.023 \le a/W < 0.062$	2.170E-02	114.9	-3647	2.940E04	/	0.99
	$0.062 \le a/W < 0.17$	1.741	-55.00	647.4	-3.295E03	6.295E03	0.99
	$0.17 \le a/W < 0.315$	-4.703	54.05	-187.6	224.3	/	0.99

5.5 Conclusions

This chapter has presented two methods for evaluating stress intensity factors in the presence of residual stress fields due to LSP and FOD. The following conclusions can be made:

1. Weight function integrals can be accurately solved using MATLAB.
2. DLOAD subroutine needs no self-equilibrium condition and is able to introduce residual stresses into a FE model.
3. Singularity elements along the crack growth path produce a good convergence of contour integrals.
4. A comparison of the WFM and FEM suggests:
    - A very good agreement between the two methods for $a/W<0.15$ ($\delta<5\%$);
    - An acceptable agreement between the two methods for $0.15<a/W<0.3$;
    - Higher FEM results than those obtained by the WFM for $a/W>0.3$.

5.7 References

ABAQUS, 2008. ABAQUS MANUAL: Analysis users manual, Abaqus Inc. 2008 Vol. 6.8.

Bao, R., Zhang, X., 2010. An inverse method for evaluating weld residual stress via fatigue crack growth test data. Engineering Fracture Mechanics 77, 3143-3156.

Bao, R., Zhang, X., Yahaya, N.A., 2010. Evaluating stress intensity factors due to weld residual stresses by the weight function and finite element methods. Engineering Fracture Mechanics 77, 2550-2566.

Beghini, M., Bertini, L., 1990. Fatigue crack propagation through residual stress fields with closure phenomena. Engineering Fracture Mechanics 36, 379-387.

Beghini, M., Bertini, L., Vitale, E., 1994. Fatigue crack growth in residual stress fields: experimental results and modelling. Fatigue & Fracture of Engineering Materials & Structures 17, 433-444.

Bouchard, P.J., Whiters, P.J., 2006. Identification of residual stress length scales in welds for fracture assessment. Residual stresses and its effects on fatigue and fracture, AG. Youtus (ed.) Springer, 163-176.

Cook, G., Timbrell, C.M, Wiehahn, M., 2002. Using ABAQUS to analysis fatigue crack growth under the combined influence of residual stress and cyclic external load, UK ABAQUS User GROUP Conference.

Kaya, A.C., Erogan, F., 1980. Stress intensity factors and COD in an orthotropic strip. International Journal of Fracture 16, 171-190.

Krug, T., Lang, K.H., Fett, T., Loehe, D., 2007. Influence of residual stresses and mean load on the fatigue strength of case-hardened notched specimens. Materials Science and Engineering A 468-470, 158-163.

Lei, Y., O'Dwod, Webster, G.A., 2000. Fracture analysis of a crack in a residual stress field. International Journal of Fracture 106, 195-216.

Liljedahl, C.D.M., Zanellato, O., Fitzpatrick, M.E., Lin, J., Edwards, L., 2010. The effect of weld residual stresses and their re-distribution with crack growth

during fatigue under constant amplitude loading. International Journal of Fatigue 32, 735-743.

Nelson, D.V., 1982. Effects of residual stress on fatigue crack propagation, residual stress effects in fatigue, ASTM STP 776, American Society for Testing and Materials, 172-194.

Parker, A.P., 1982. Stress intensity factors, crack profiles, and fatigue crack growth rates in residual stress fields, ASTM STP 776, American Society for Testing and Materials, 13-31.

Reji, J., Larsen, J.M., Buchanan, D.J., Ashbaugh, N.E., 2001. Incorporating residual stresses in life prediction of turbine engine disks. Proceddings: RTO AVT "Ageing Mechanisms and Control: Part B – Monitoring and Management of Gas Turbine Fleets for Extended Life and Reduced Costs". Manchester, UK.

Rooke, D.P., Cartwright, D.J., 1976. Compendium of stress intensity factors. London: Ministry of Defence.

Sansoz, F., Brethes, B., Pineau, A., 2001. Propagation of short fatigue cracks from notches in a Ni base superalloy: experiments and modelling. Fatigue & Fracture of Engineering Materials & Structures 25, 41-53.

Servetti, G., Zhang, X., 2009. Predicting fatigue crack growth rate in a welded butt joint: the role of effective R ratio in accounting for residual stress effect. Engineering Fracture Mechanics 76, 1589-1602.

Wilks, M.D.B, Nowell, D., Hills, D.A., 1993. The evaluation of stress intensity factors for plane cracks in residual stress fields. Journal of Strain Analysis 28, 145-152.

Wu, X.R., Carlsson, A.J., 1991. Weight functions and stress intensity factor solutions. 1st ed. Oxford: Pergamon Press.

Zabeen, S., Preuss, M., Withers, P.J., Spanrad, S., Tong, J., Schofield, J., 2010. Synchrotron strain mapping of the residual strain distribution around foreign object damage in laser shock peened Ti-6AL-4V alloy. Materials Science Forum 652, 19-24.

Chapter 6 Fatigue crack growth in a residual stress field

6.1 Introduction

This chapter presents first the calibration results of the DCPD system used for crack length monitoring. Fatigue crack growth in LSP+FODed aerofoil specimens has been investigated under LCF, HCF and combined LCF+HCF loading conditions. The crack growth rates are correlated with the stress intensity factor for a standard single edge crack and a modified stress intensity factor considering the longitudinal residual stresses, as obtained in Chapter 5. The results are discussed with regard to the role of residual stresses in the characterisation of fatigue crack growth due to head-on and 45º impact under LCF, HCF and combined LCF and HCF loading conditions. Results of the present specimens (LSP+FODed) are also compared with those from unpeened FODed specimens of the same alloy from a previous study (Hall et al., 2008).

6.2 Results and discussion

6.2.1 DCPD calibration

Accurate measurement of crack length during fatigue testing is of vital importance to the evaluation of crack growth behaviour under selected loading waveforms. To this end, a relationship between the voltage ratio and the crack length was sought for an effective DCPD method in detecting and monitoring early crack growth, using the calibration experiments as described in Chapter 3. DCPD reference probe wires were welded at the bulk part of the specimen, where the readings will be least disturbed by a growing crack. The distance between the probe wires was 5mm. The

active probe wires were placed at 2.5mm on either side of the centre of the FOD indent to achieve the sensitivity required while avoiding tensile stress regions around the FOD notch based on the evaluation of the residual stress distribution. A summary of the DCPD arrangement can be found in Chapter 3 and the procedure follows the previous study (Hall et al., 2008).

The DCPD voltage ratio, the ratio of the active and the reference voltage readings, was recorded during the experiment. Periodically, the crack length was also measured using the acetate replication. Figure 6-1 shows two sets of the experimental results for each notch type. A polynomial relationship between crack length, a, and voltage ratio, V_R, was also included.

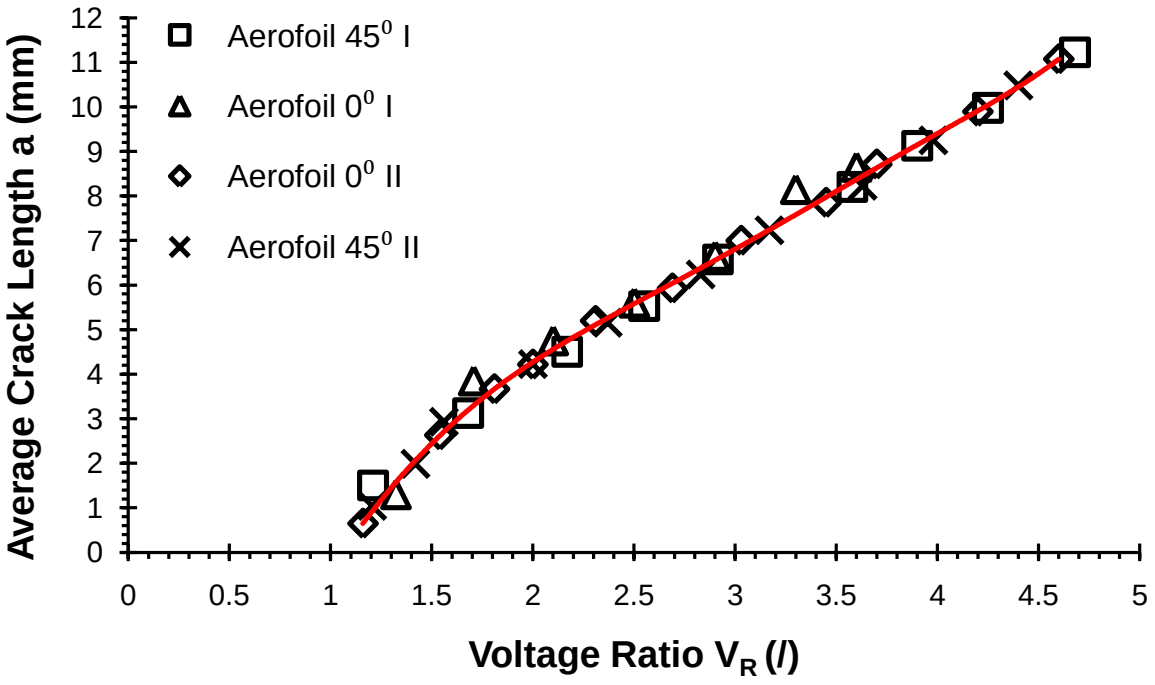

$a = 0.028V_R^6 - 0.452V_R^5 + 2.781V_R^4 - 7.935V_R^3 + 9.238V_R^2 + 2.995V_R - 7.021$ $R^2 = 0.992$

Figure 6-1 The relationship between voltage ratio and crack length; the crack lengths were obtained by the replica method and direct surface measurements post experiments.

A polynomial curve was used to fit the experimental data in Figure 6-1. The calibration curve with an R^2 distribution better than 0.99 may be expressed as:

$$a = 0.028V_R^6 - 0.452V_R^5 + 2.781V_R^4 - 7.935V_R^3 + 9.238V_R^2 + 2.995V_R - 7.021 \quad (6\text{-}1)$$

where a is the crack length (mm) from the leading edge (including the FOD notch depth) and V_R is the voltage ratio.

6.2.2 Crack extension with cycles

The voltage ratios were recorded as a function of the number of cycles for all experiments, converted into crack length versus the number of cycles using the calibration curve (Fig. 6-1) as well as the measured crack lengths at the beginning and the end of each experiment. Given a constant load, the fatigue crack growth (FCG) rate is dependent on the crack length measured from the edge of the specimen, including the depth of the FOD notch. For this reason, the indent depth has been included in the value of crack length in the following diagrams. The indent depths vary, depending on the impact angle and velocity, hence the initial crack lengths may vary, as shown in Figure 6-2.

The evolution of the crack length as a function of the number of cycles is shown in Figure 6-2 for the LSP+FODed specimens (head-on and 45° impacts) and an untreated specimen (FOD, head-on), for a) LCF, b) HCF, and c) combined LCF+HCF loading conditions. The crack growth under HCF only and combined LCF+HCF fatigue loading conditions show similar trends, as shown in Figure 6-2b and c. The crack in samples subjected to 45° impacts clearly grew earlier and faster than that in the samples impacted head-on. This seems to be consistent with the more severe damage sustained during a 45° impact, despite the smaller notch depth in a 45° impact than that produced in a head-on impact.

a)

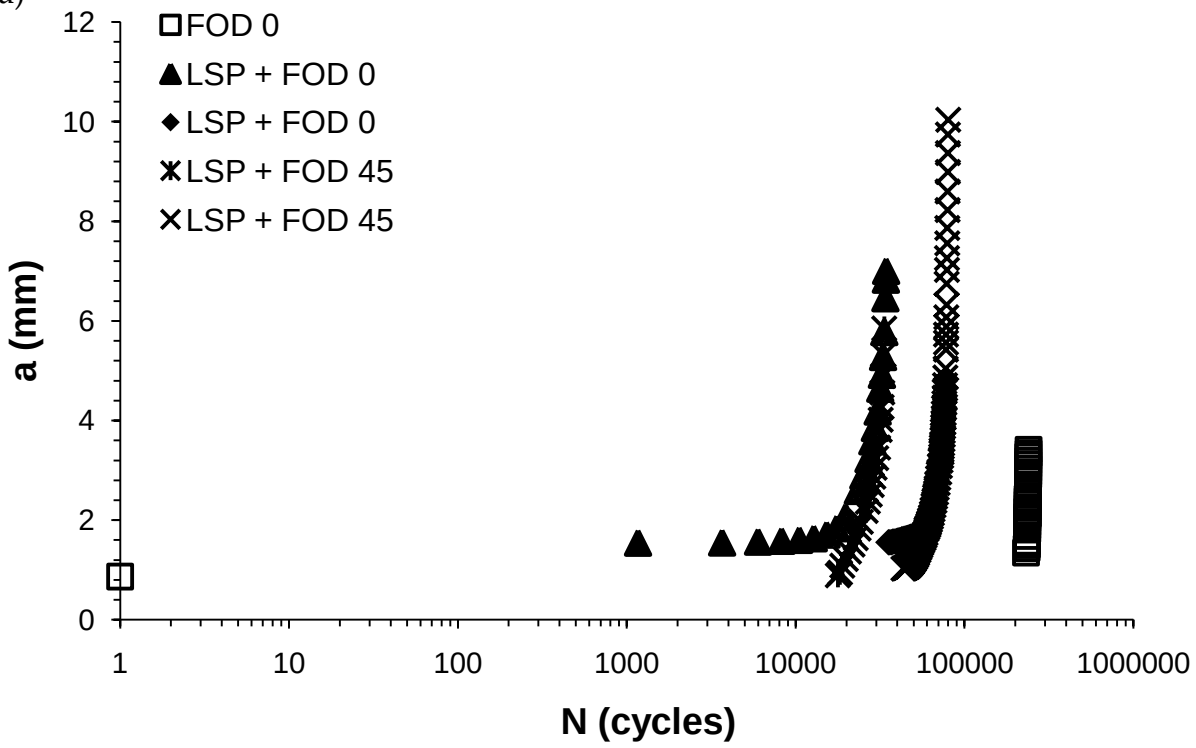
FOD 0
LSP + FOD 0
LSP + FOD 0
LSP + FOD 45
LSP + FOD 45
a (mm)
N (cycles)
0
2
4
6
8
10
12
1
10
100
1000
10000
100000
1000000

b)

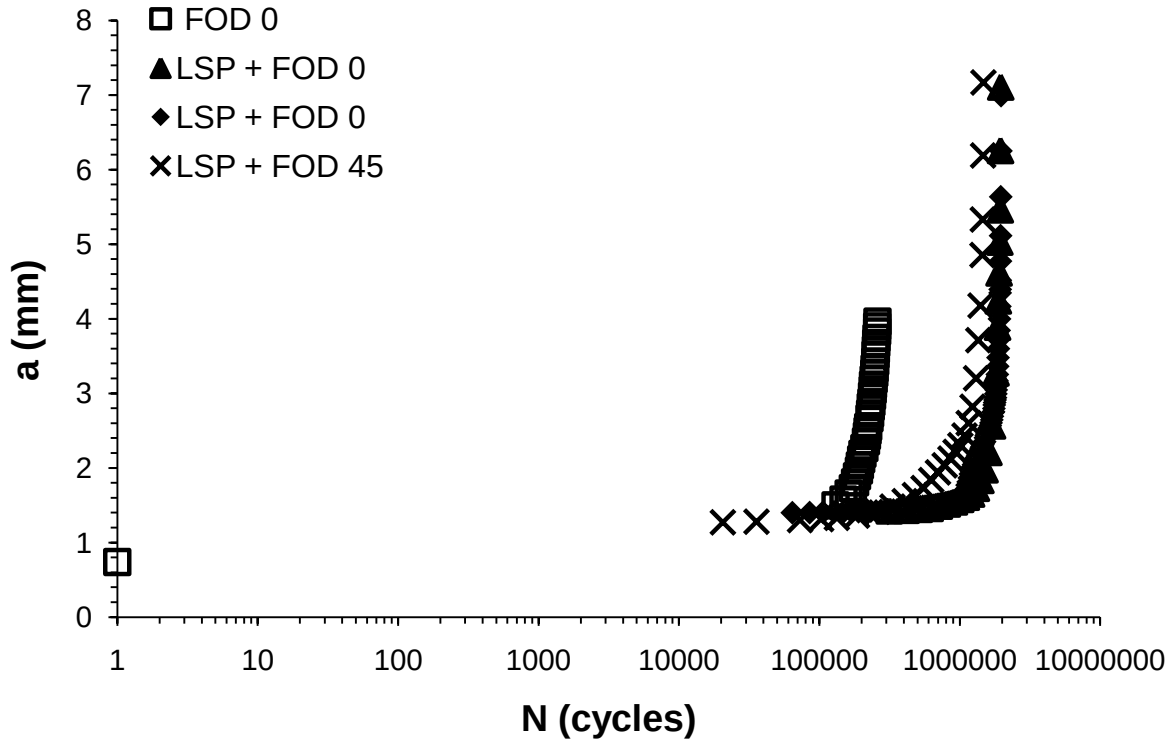
FOD 0
LSP + FOD 0
LSP + FOD 0
LSP + FOD 45
a (mm)
N (cycles)
0
1
2
3
4
5
6
7
8
1
10
100
1000
10000
100000
1000000
10000000

c)

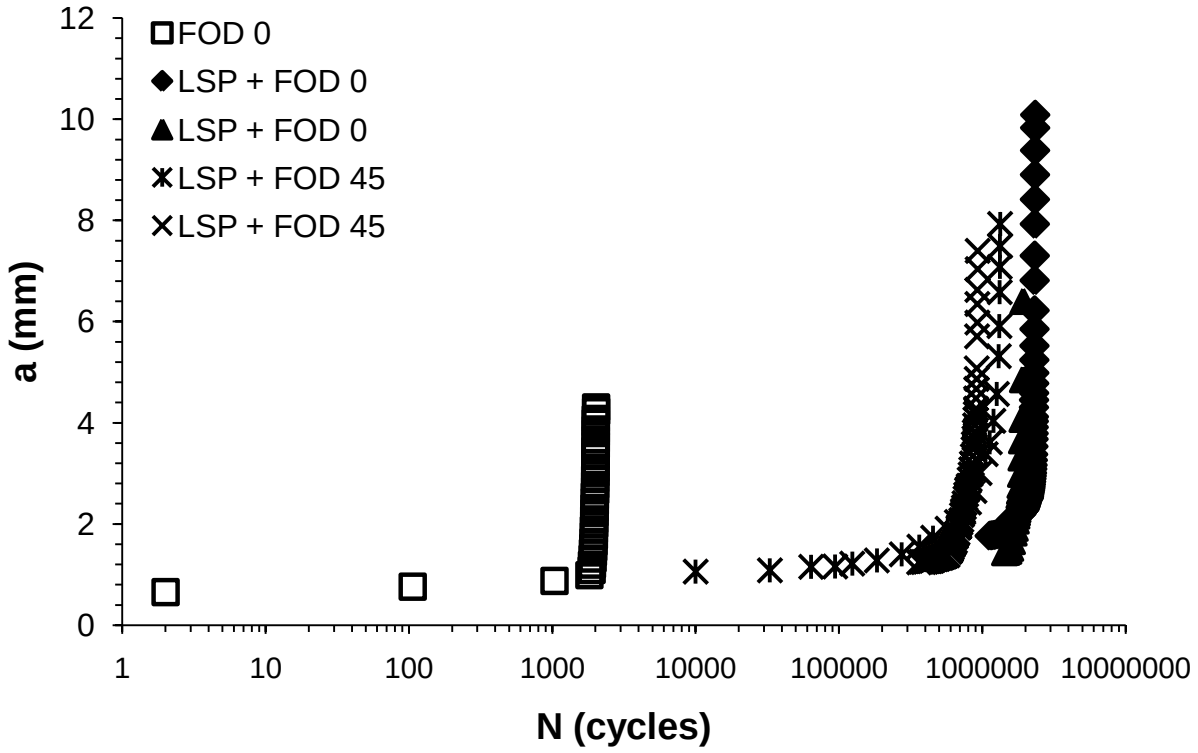

Figure 6-2 The evolution of the crack length as a function of the number of cycles for samples subjected to 0° and 45° impacts, comparison of results from the LSP+FOD and FOD only specimens (0° impacts) under, a) LCF loading condition, b) HCF loading condition, and c) combined LCF and HCF loading blocks.

The secondary Y-axis (framed symbols) in Figure 6-3 shows the notch depths for head-on impacts with an average value of 1.5mm, whilst the average depth for 45º impacts is 0.78mm. Mall et al. (2001), Thompson et al. (2001) and Ruschau et al. (2003) found that fatigue life decreases with increasing notch depth for spherical impacts. The current results seem to suggest that the impact angle has more influence on the fatigue strength than the notch depth, as also observed by Nowell et al. (2003a) for cubical, and Ruschau et al. (2001) for spherical impacts. Samples impacted at close to 0º have higher fatigue strength, due to higher compressive residual stresses generated from 0º impacts when compared to 45º impacts, even for LSPed materials (Chapter 5). This seems to indicate that the fatigue limit stress is more influenced by the impact angle than the notch depth. In addition, this effect appears to be independent of the 'pre-residual stress' state of the material, LSP in this case.

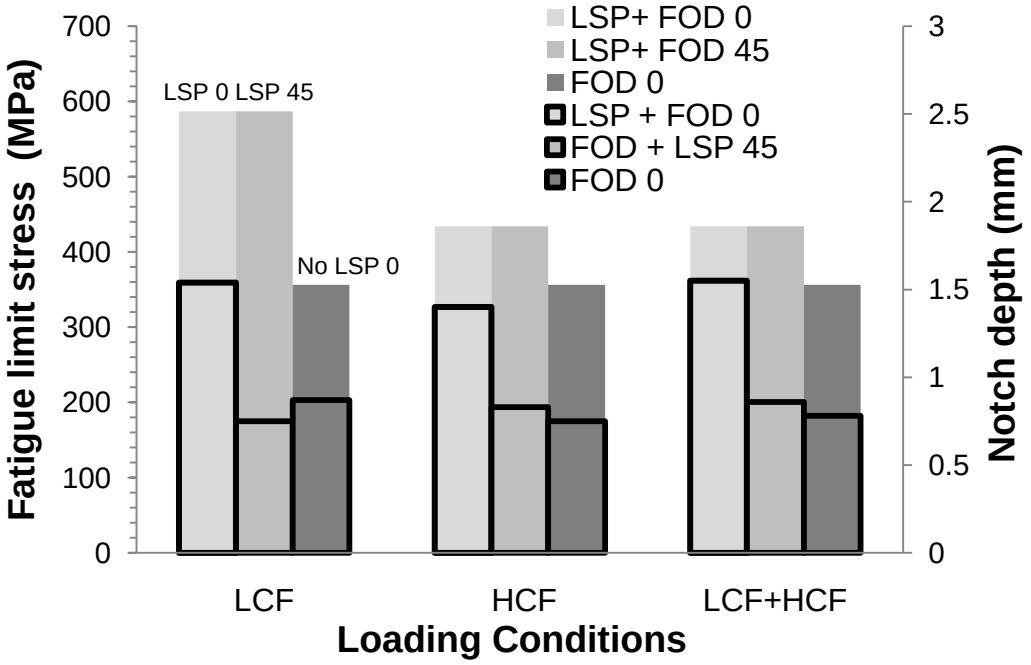

Figure 6-3 Comparison of the fatigue limit stresses for the three loading conditions. The samples are marked for their impact conditions (0° or 45°) and specimen conditions (FOD; LSP+FOD). The notch depths are also presented on the secondary Y-axis with the framed symbols.

Figure 6-2a shows two data sets for LSP + LSPed specimens for each impact condition, tested under LCF loading. The notch depths for head-on impacts are a=1.47mm for a longer and a=1.54mm for a shorter fatigue life. The same trend can be seen for 45° impact notches, where the shallower notch (a=0.63mm) has a longer life than that from the deeper notch (a=0.75mm). For a given impact angle, the crack seems to initiate first at the deeper notch, indicating that notch depth may be important for crack initiation. This was also observed for untreated FODed specimens (Ruschau et al., 2001; Nowell et al., 2003a).

Figure 6-3 shows the fatigue limit stresses for FOD + LSPed and FODed only specimens. The influence of LSP on the fatigue life improvement over that in non-peened specimens has been demonstrated (Ruschau et al., 1999a; 1999b). The fatigue limit stress for the LSP+FODed specimens was 434MPa for head-on and 45° impacts compared with 356MPa for FODed only specimens, under a combined LCF+HCF and HCF loading. Clearly, even with a similar notch depth for 45° impacts and twice

as deep notch for 0º impacts compared to unpeened FOD notches, significantly delayed onsets of crack growth were observed for the LSP+FODed samples. This is consistent with the previous work from Ruschau et al. (1999a; 1999b) and Nalla et al. (2003) for Ti-6Al-4V, as well as studies from Rubio-Gonzalez et al. (2004; 2011), Hatamleh (2009) and Hatamleh et al. (2007; 2009) for aluminium alloy, where increased fatigue lives and reduced fatigue crack growth rates in LSP-treated material compared to untreated material, were obtained. Prevey et al. (2004a; 2004b) studied Low Plasticity Burnishing treated titanium with simulated FOD notch using EDM, and found similar results of enhanced fatigue life. Under LCF conditions, the LSPed specimens show earlier crack onsets of crack growth for both impact cases under LCF loading conditions compared to untreated FODed specimens. However, the applied stress level for LSP+FODed specimens was 64% higher than that in the untreated FODed specimens.

Using the load increment loading scheme, no growth at all was detected in samples tested under LCF only cycles until the stress level was increased significantly to 587MPa (35% higher than that used in HCF and LCF+HCF cases), as shown in Figure 6-3. This suggests that compressive residual stresses have a more significant effect at low R ratios, which was also observed from Ruschau et al. (1999a; 1999b) and Nalla et al. (2003). SEM investigation (Ruschau et al., 1999a; 1999b) found evidence of smeared surface features close to the crack tip, possibly due to the high compressive stresses generated through the LSP treatment. It was argued that such an advantage diminishes at a higher R-ratio, which seems to be consistent with the current results.

Comparing the LCF+HCF data against the HCF data for LSP+FODed specimens, it can be readily seen in Figure 6-4 that the fatigue lives are very similar for these impact conditions. It can be concluded that the crack growth rate under spectrum loading may be dominated by the minor HCF cycles (R=0.7), whilst the major cycles (R=0.1) appear to have no substantial influence on the growth rate. This is consistent with results from Ruschau et al. (1999a; 1999b).

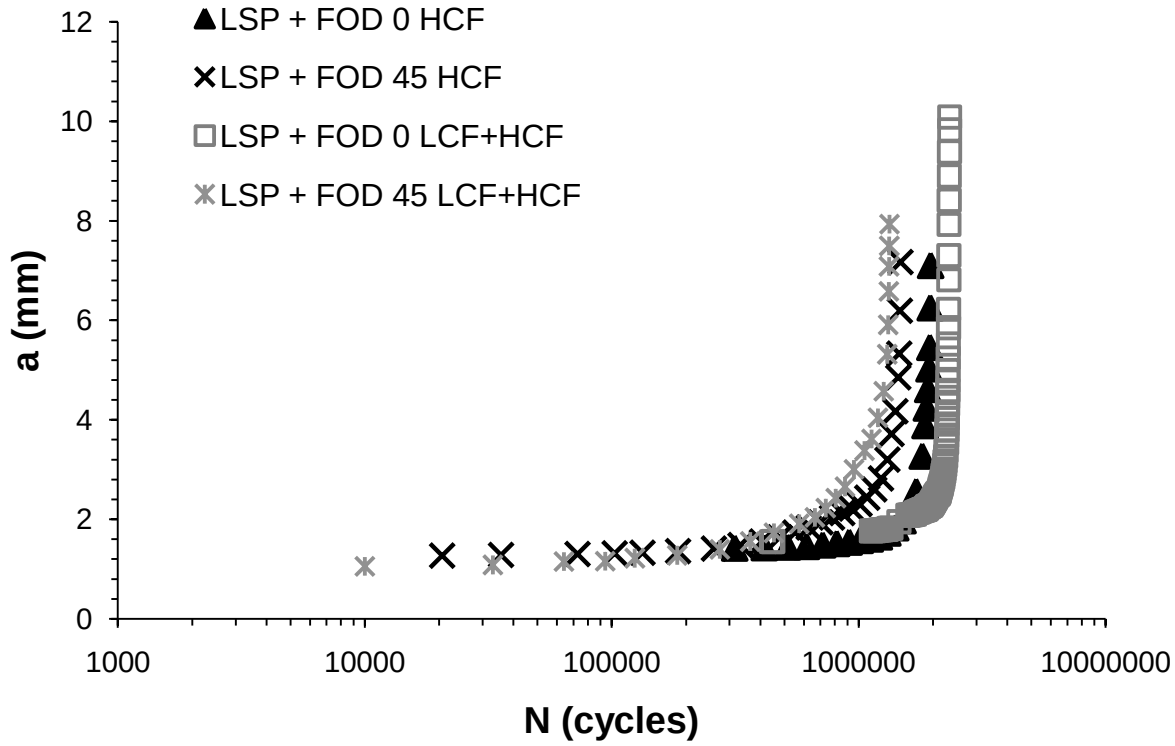

Figure 6-4 Comparison of crack length versus number of cycles for HCF and LCF+HCF loading conditions.

6.2.3 Fatigue crack growth rate versus crack length

Figures 6-5a-c show the fatigue crack growth rates as a function of crack length, with the LSP boundary also indicated. It is immediately clear that all FCG rates from LSP+FODed specimens are below the FCG rates from the FOD only specimen, despite of the higher applied stresses for the former (Fig. 6-3).

Early fast increasing crack growth rates turn into steady crack growth at a crack length of about 2mm. For LCF and HCF only loading condition, the crack growth rates in specimens experienced LSP+FOD seem to have a similar slope to that obtained from unpeened FODed specimen in da/dN vs. a plots. A larger scatter band is observed, especially for the 45° impacted samples, which might be a result of the uneven multiple crack initiation of both sides from the FOD notch (Chapter 4). Also indicated is the LSPed area, which is about 6mm from the leading edge. Above this area, the crack growth behaviour in LSP+FODed and FODed specimens

becomes similar. The crack growth rates under HCF or LCF only conditions seem to be similar in this regard. For all loading conditions, the data from different specimens under LCF+HCF conditions seem to differ the least, compared to data of FOD only specimens.

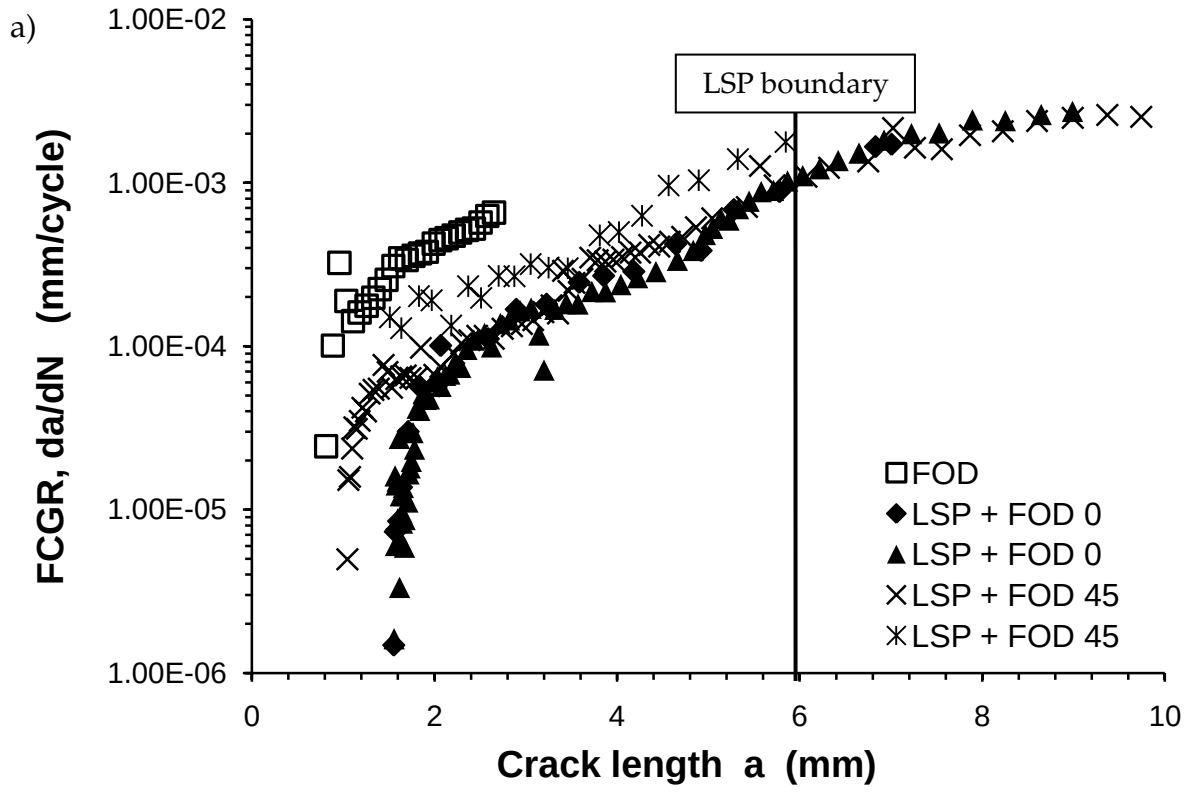

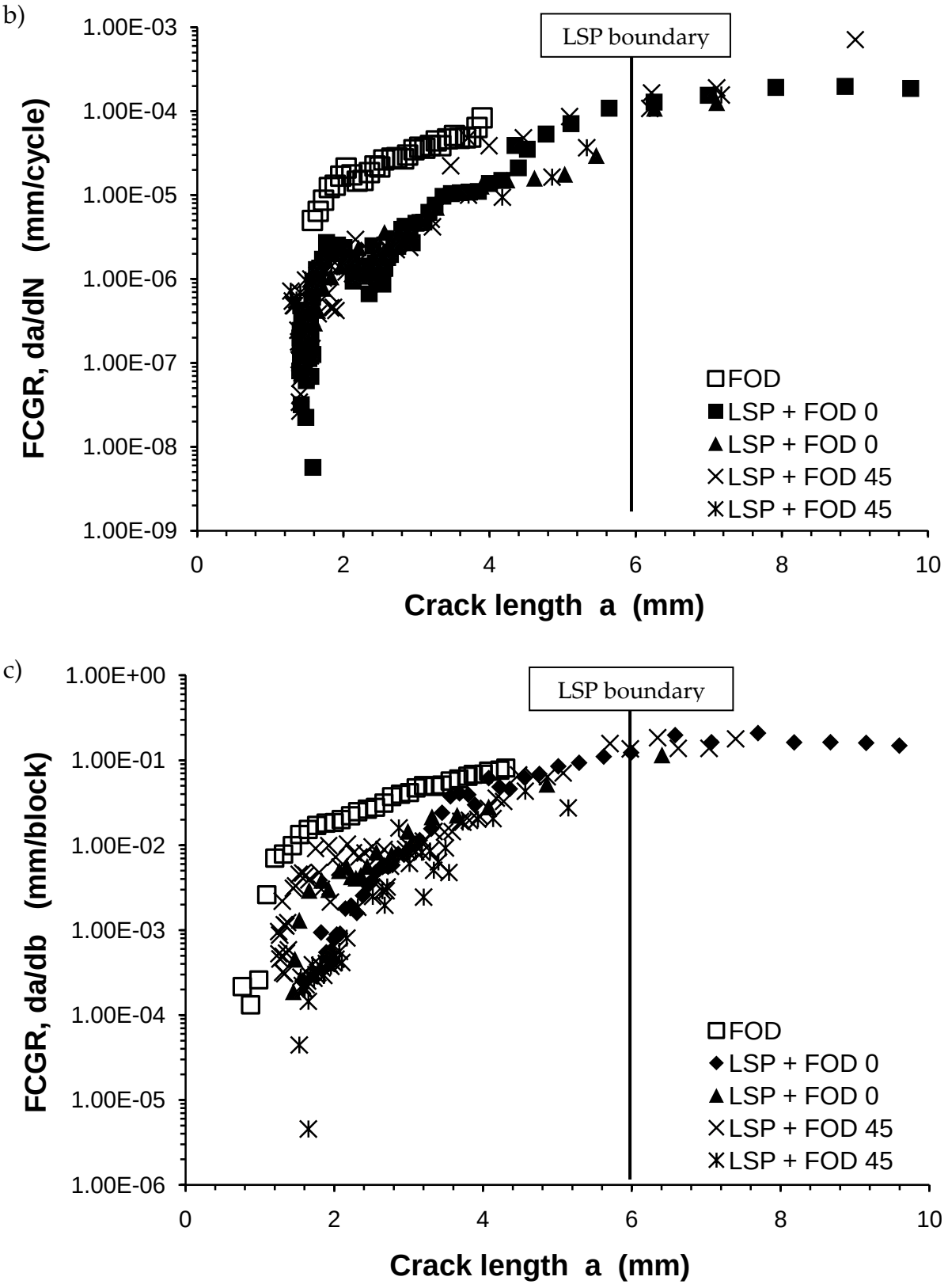

Figure 6-5 Fatigue crack growth versus crack length from specimens FODed 0°, LSP + FODed impacted 0° and 45^0 for a) LCF cycles only, R=0.1, b) HCF cycles only, R=0.7, and c) LCF+HCF, R=0.1 and R=0.7, n=1:1000.

6.2.4 Fatigue crack growth correlation with a standard SIF

Fatigue crack growth rates are correlated, in the first instance, with the standard stress intensity factor (SIF) range for a single edge crack in a rectangular cross-section specimen (Rooke and Cartwright, 1976). This standard SIF solution is a 2D solution (Chapter 3), while the variation of the thickness of the actual samples could not be considered, neither the residual stresses. The slight variation in the aerofoil shape between the current and the previous specimens was also not considered.

For the LSP+FODed specimens (head-on and 45° impact) and FODed only (head-on), Figure 6-6 shows the correlations under a) LCF, b) HCF and, c) combined LCF+HCF loading conditions. For all loading conditions, reduced FCG rates at higher ΔK values are evident for LSP+FODed specimens compared with those from untreated FODed, suggesting retarded crack growth due to LSP.

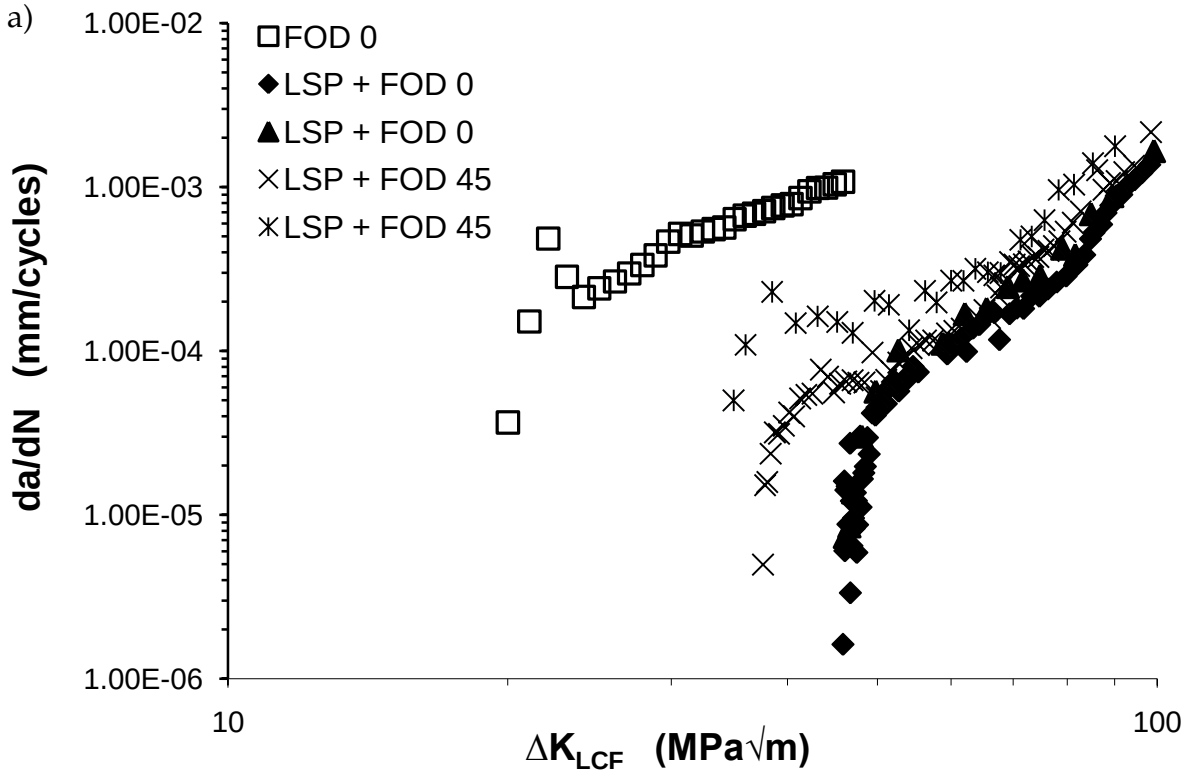

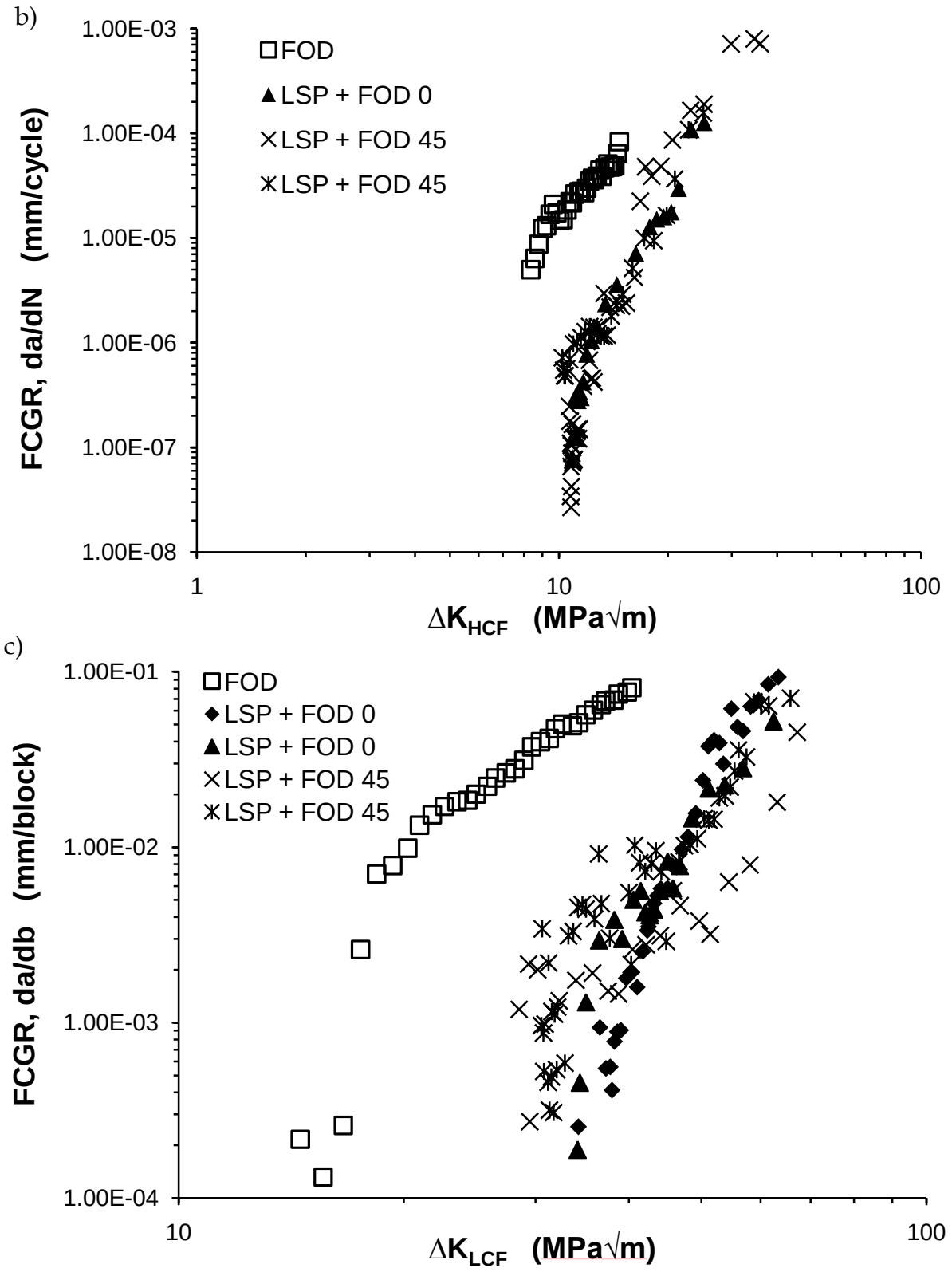

Figure 6-6 Fatigue crack growth versus stress intensity factor range estimated using a standard single edge crack solution for loading conditions a) LCF cycles only, R=0.1, b) HCF cycles only, R=0.7, and c) LCF+HCF, R=0.1 and R=0.7, n=1:1000.

To obtain similar crack growth rates for FOD+LSPed material, the ΔK level has to be increased. In the early crack growth regime, similar slopes are obtained for the LSPed and the untreated FODed specimens. Further on, the LSP+FODed specimens seem to follow a steeper slope, especially for LCF and HCF only conditions, indicating faster crack growth rates as compared to the FOD only specimens (Figs 6-6a, b). The crack growth rates for LSPed and untreated FODed specimens differ the least for HCF loading conditions, suggesting a less significant effect of residual compressive stresses on the FCGR under a high R ratio.

The influence of applied stress ratio on fatigue crack growth can also be seen by comparing Figures 6-6a-c with the results of Hatamleh (2009). The onset ΔK value for crack growth for LSP+FODed samples is roughly 30MPa√m for LCF, nearly an order of magnitude greater than that for the untreated FODed specimens. This is consistent with the observation by Ruschau et al. (1999a; 1999b). For HCF only loading conditions the onset ΔK is about 10MPa√m and closer to the unpeened results than those under LCF conditions. The results from the combined LCF+HCF conditions seem to be in between these two results.

The conventional perception is that fatigue crack initiation is a function of the alternating stress amplitude but not the mean stress, while the growth of fatigue cracks is a function of both the stress amplitude and the mean stress (McClung, 2006). This theory implies that residual stresses have potentially significant influence on the fatigue crack growth. This influence may be especially pronounced in the early fatigue crack growth, i.e. near-threshold regime. Residual stresses can make a significant difference between crack growth and crack arrest. Conventional analysis that considers only the geometry effect is clearly inadequate, as it will significantly underestimate fatigue crack growth at low stress intensity factor ranges (Fig. 6-6). This illustrates the importance of considering residual stresses towards a more accurate assessment of the stress intensity factor as the crack driving force. The effects of residual stresses for the given loading conditions on the FCGR are discussed in the following section.

6.2.5 Fatigue crack growth correlated with a modified SIF

The stress intensity factor has been modified to consider the longitudinal residual stresses (1D) in order to be a step closer to the reality at the crack tip. An effective K is obtained, and Figure 6-7 shows a) the effective stress ratio R_{eff}, and b) the effective SIF range ΔK_{eff} for a typical applied stress of 435MPa for R=0.1 (LCF) and R=0.7 (HCF) loading conditions. Under the applied cyclic loads, these parameters were calculated as (Liljedahl et al., 2010; Servetti and Zhang, 2009; Ruschau et al., 1999a; 1999b):

$$\Delta K_{eff} = \left(K_{app,max} + K_{res}\right) - \left(K_{app,min} + K_{res}\right)$$

$$R_{eff} = \left(K_{app,min} + K_{res}\right) / \left(K_{app,max} + K_{res}\right)$$

Under cyclic loads, only R_{eff} changes due to the presence of residual stresses. R_{eff} is the effective stress ratio based on the calculated values of $K_{eff,\,max}$ and $K_{eff,\,min}$, hence R_{eff} differs from the nominal applied load ratio R as it is a function of K_{res}.

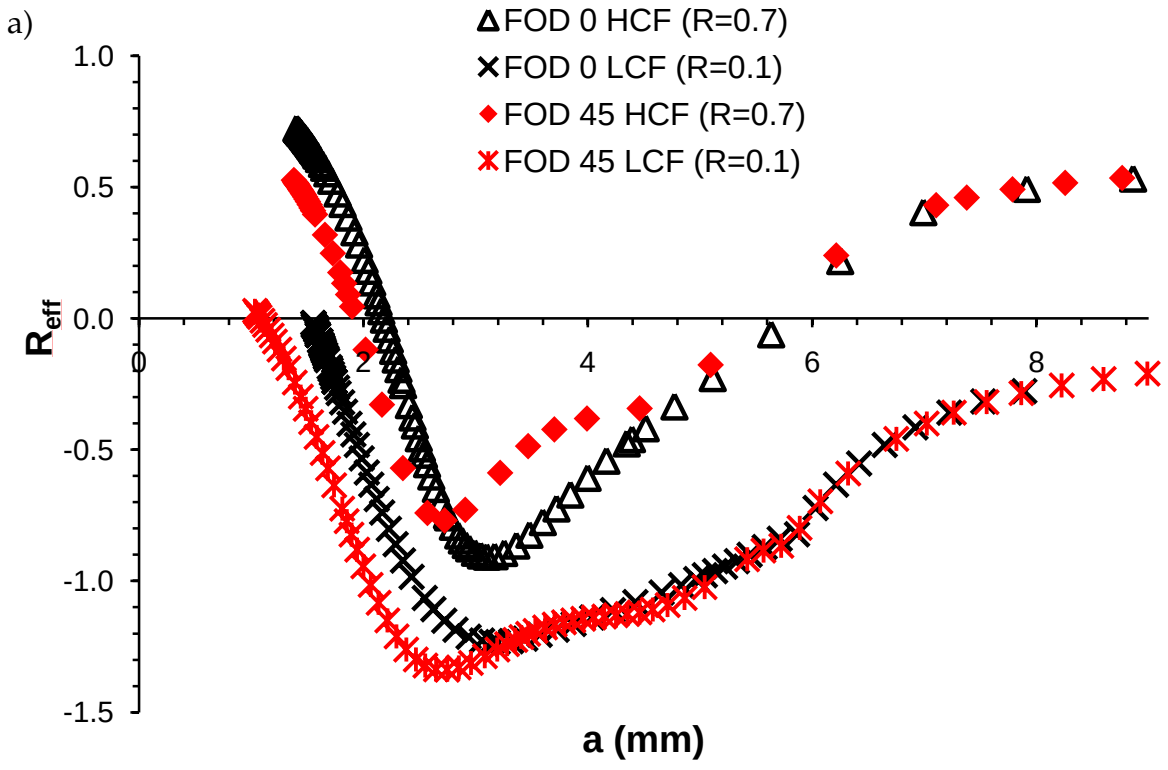

b)

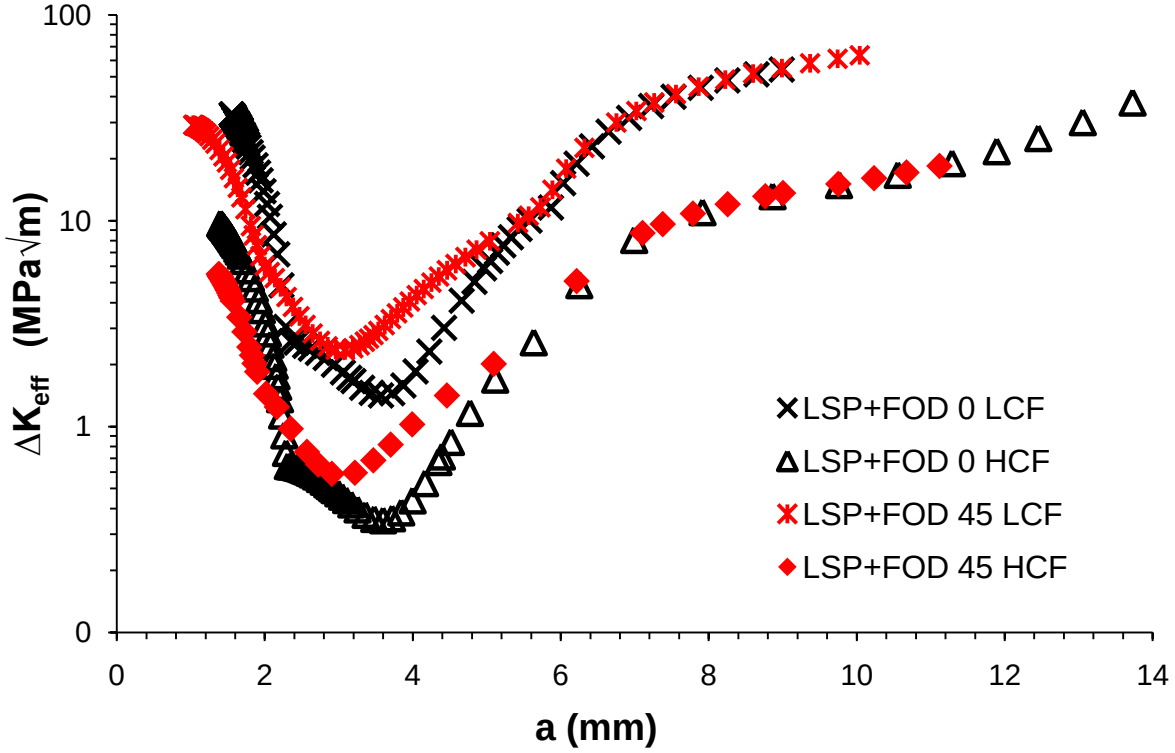

Figure 6-7 a) The effective stress ratios R_{eff} for nominal stress ratios R=0.1, 0.7, and b) the effective stress intensity range with crack length for the loading conditions LCF and HCF for a typical applied stress of 436MPa.

The differences for the two load ratios are clearly visible. The R_{eff} for HCF conditions stays above the R_{eff} for LCF conditions, suggesting overall lower crack closure effects. To achieve a similar effect on crack growth in terms of R-ratio, the load level for LCF conditions has to be increased compared to HCF only loading conditions. This was observed in the experiments, as no crack growth was detectable for LCF conditions at the same load level as that under the HCF conditions.

The minima in both R_{eff} and K_{eff} for 45° impacts under both loading conditions occurred at a smaller crack length (a=2.8mm) and less compressive than that for 0° impacts (a=3.2mm), consistent with their respective residual stress distributions (Fig. 5-2). Figures 6-7a, b seem to suggest that the residual stresses significantly reduce the stress intensity factor and stress ratio early in a test when the ΔK is low, and the effect is reduced as the ΔK increases, consistent with the observation reported in Hatamleh et al. (2009).

When the longitudinal residual stresses are considered, the effective SIF solutions (Chapter 5) are used to correlate the fatigue crack growth rates, and the results are shown in Figures 6-8 for a) LCF conditions, b) HCF conditions, and c) for combined LCF+HCF conditions.

The FCG rates of the LSP+FODed specimens impacted at different angles differ, especially in the early stage, caused probably by the variation in the notch depth, the residual stress distribution and the FOD damage features. The magnitude of the residual stresses depends on the impact angle, and therefore the true stress ratio near the notch tip will vary, influencing the FCGR at the early stage. Generally more scattered data can be observed for the 45° impact cases (Fig. 6-8b, c), which might be due to the multiple crack initiation and growth on both sides of the FOD notch (Chapter 4). After the early stage crack growth, both data sets converge into a similar sloped curve, as observed in previous Chapters 6.2.3, 6.2.4. More scattered crack growth rate data are obtained for LSP+FODed specimens during the early stages of crack growth under combined LCF+HCF loading conditions.

Compared to the results presented in Figure 6-7, significant differences may be observed in the considerable reduction of the values of ΔK in the early crack growth regime for all loading conditions and impact angles due to the compressive residual stresses. The crack growth rate retardation in this stage seems very similar for all loading conditions, although the onset ΔK values are almost unaffected by the residual stress correction compared to those shown in Figure 6-7.

At low ΔK values, variation in crack growth rates is evident, reflecting the discontinuous nature of the early crack growth due to the influence of the residual stresses. However, a negative slope of the da/dN vs. ΔK suggests a reduction of crack driving force and yet increased crack growth rate. The reduction of ΔK is due to the effect of increasing compressive residual stresses. A decrease of the R_{eff} and increased crack closure effects also occur. Only after the residual stress reaches the minimum, the correlation of the crack growth rates in terms of ΔK becomes positive, i.e. increasing ΔK results in an increase of the crack growth rate. The crack arrest phenomena observed by Ruschau et al. (1999a; 1999b) after crack initiation might be

explained by the decreased K_{eff} and R_{eff} due to residual stresses and their retardation effects on crack growth.

a)

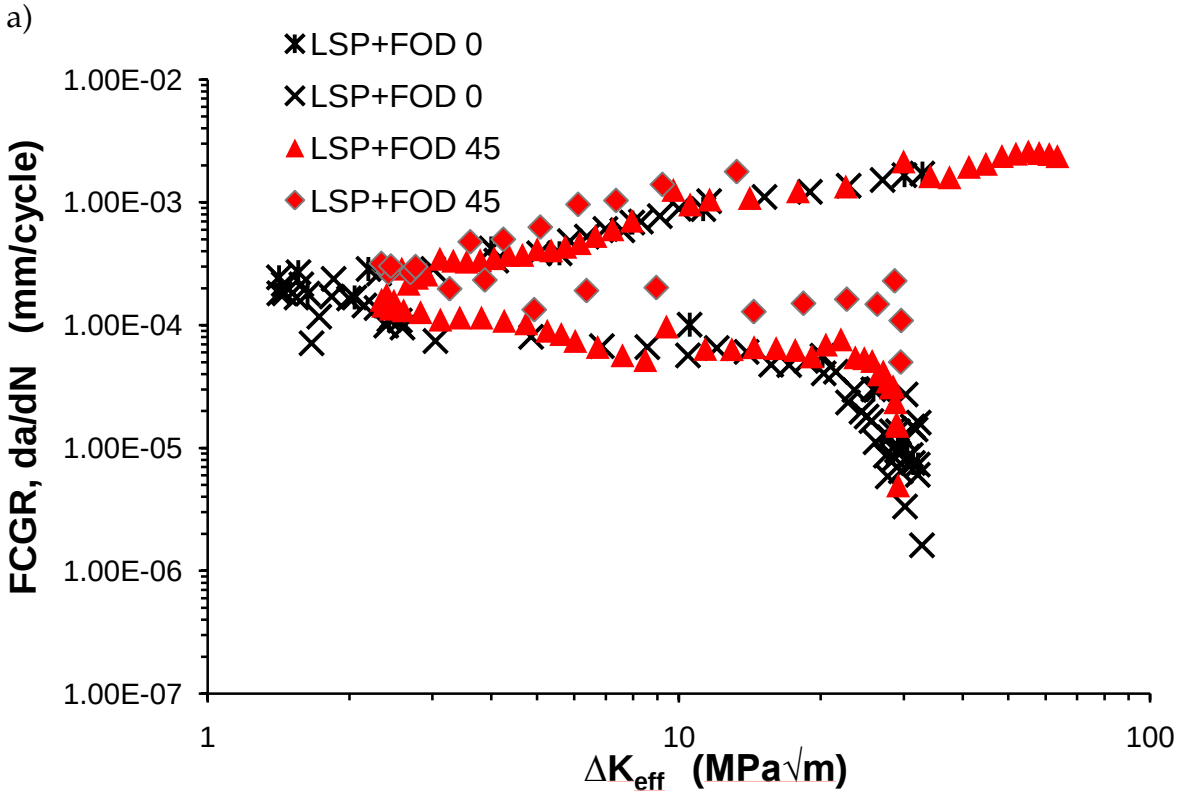

b)

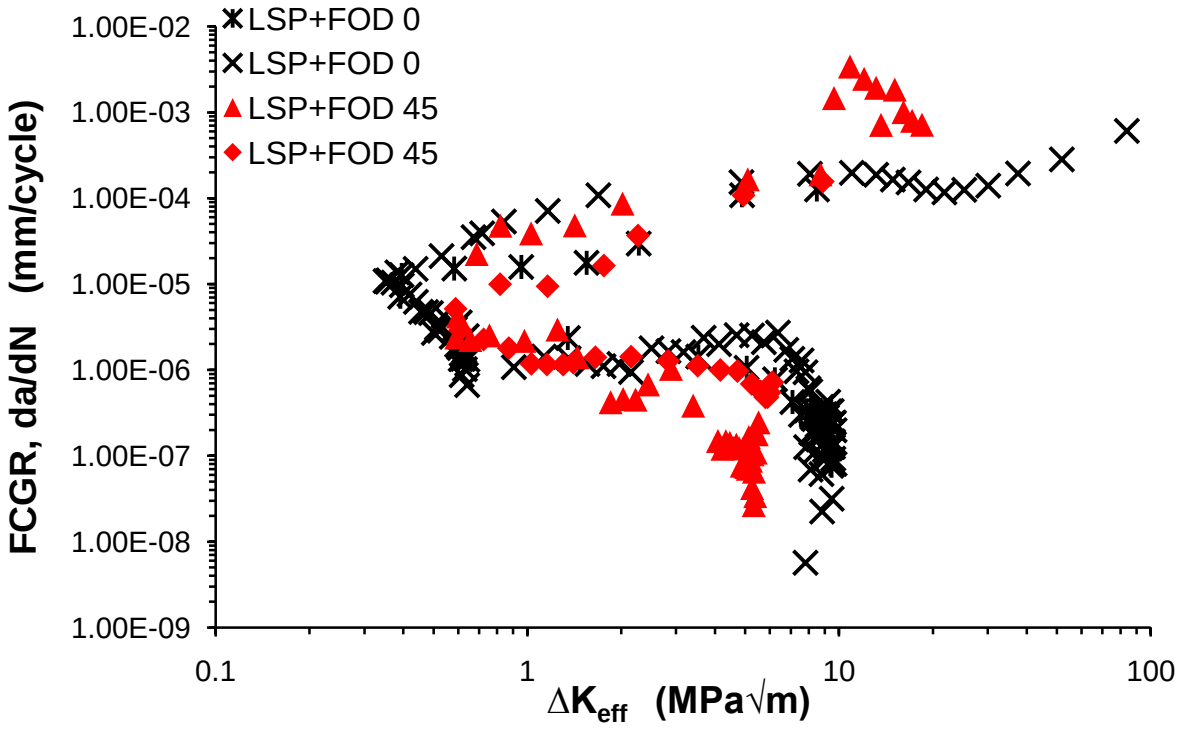

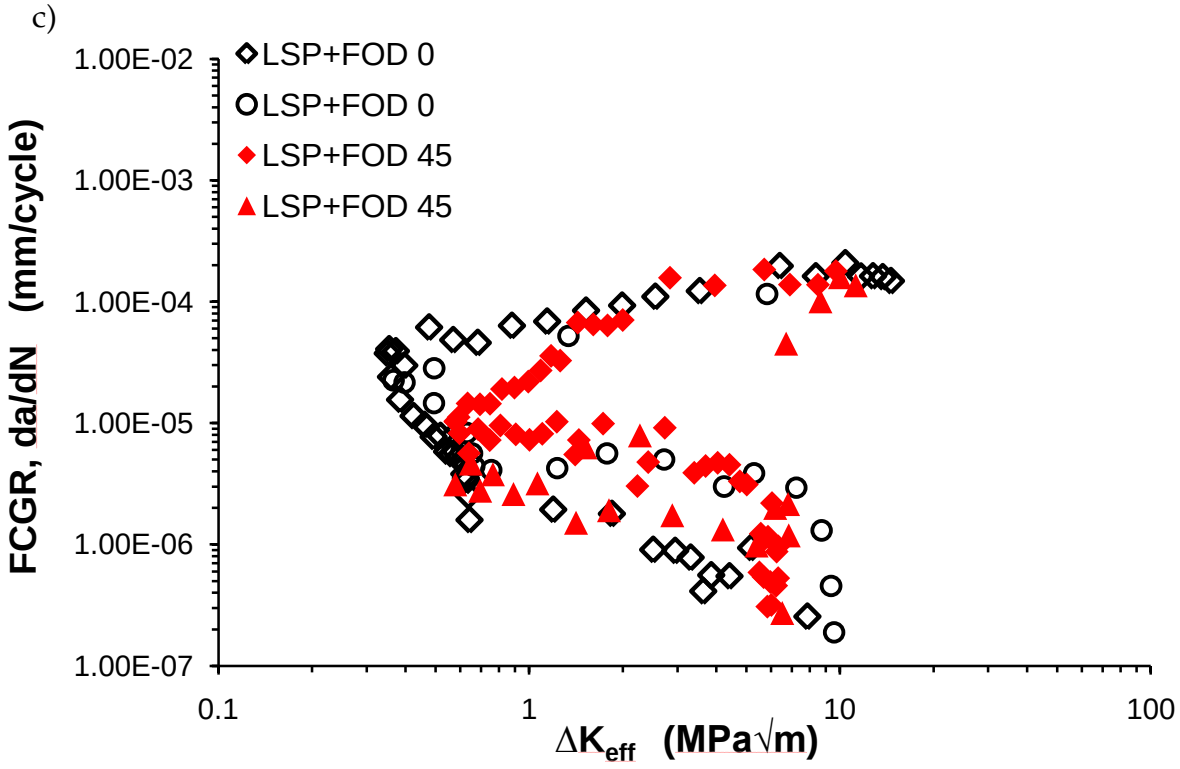

Figure 6-8 Fatigue crack growth rates correlated with the modified stress intensity factor ΔK corrected with longitudinal residual stresses for loading conditions a) LCF cycles only, R=0.1, b) HCF cycles only, R=0.7, and c) LCF+HCF, R=0.1 and R=0.7, n=1:1000.

For HCF-only and LCF+HCF cycles, a comparison of Figures 6-6b-c and 6-7b-c reveals accelerated early crack growth rates in LSP+FODed specimens when residual stresses are considered. For a ΔK value of 0.2MPa√m, the crack growth rates are in the region of 1×10^{-5}, as opposed to the same growth rate for a ΔK value of about 12MPa√m when the residual stresses are ignored. For LCF conditions, higher ΔK values are obtained due to the higher applied loads. The trend in the crack growth rate correlation with the modified ΔK is similar to those of the other two loading conditions, with a somewhat higher ΔK value of about 1.5MPa√m.

An increased load ratio resulted in early crack initiation under lower applied stress range. This might be mainly attributed to the absence of crack closure at a higher load ratio. Load ratio has been proven to have a significant influence on the FCGR (e.g. Noroozi et al., 2007). The change in R ratio introduced by the LSP+FOD residual stresses may be directly related to the change in fatigue crack growth rates as

suggested by the studies of (Hatamleh, 2009; Servetti and Zhang, 2009; Ge et al., 2006). In general, FCGR increases with the increase in positive R, and decreases with the decrease in R (Hill, 1996; Noroozi et al., 2006).

Ruschau et al. (1999a; 1999b) and Hatamleh (2009) concluded that under HCF conditions (high R), the beneficial effect of the residual stresses could be significantly less than that under LCF conditions, the latter may involve low or negative values of R. At low R ratios, enhanced FCGR resistance can be realised due to superposition of residual compressive stresses on the applied stress, provided that the applied cyclic stress is below the residual stresses of the LSP (Ruschau et al., 1999a; 1999b). At high stress ratios, little improvement in FCGR is realised, when the cyclic stresses are above the residual stresses. A higher load (Chapter 6.2.2) was needed to grow a crack under LCF conditions compared to the load levels of HCF only or combined LCF+HCF conditions. Under HCF only conditions the onset ΔK value is about 10MPa$\sqrt{m}$, as opposed to 30MPa$\sqrt{m}$ under LCF, suggesting the more detrimental effect of HCF loading. Ruschau et al. (1999a; 1999b) found, by comparing the LCF+HCF data against the HCF data, that the spectrum crack growth rate is dominated by the minor cycles (R=0.7). They concluded that major cycles have no substantial influence on the crack growth rates, which seems to be consistent with this study (Figs. 6-6b, c).

The small crack growth behaviour during the early phases of crack growth post-FOD impact is common to all LSP+FODed specimens, irrespective of the subsequent loading conditions. This characteristic is revealed only after the predominant residual stress component, i.e. the longitudinal residual stress, is considered in the calculation of the stress intensity factor. A higher scatter band is observed for data obtained under LCF+HCF loading conditions due to reasons mentioned earlier.

The present analysis considered only one directional residual stress distribution along the perceived crack path, an approach similar to that adopted previously (e.g. Bao et al., 2010; Servetti and Zhang, 2009; Liljedahl et al., 2010; Krug et al., 2007; Beghini et al., 1994; Beghini and Bertini, 1990). Pavier at al. (1999) developed a 3D finite element crack analysis, including through-the-thickness variation of residual

stress, stress relaxation and redistribution effects. They concluded that stress intensity factors calculated with 3D analysis are generally higher than those calculated using 2D analysis. The results of Pavier et al. (1999) seem to suggest that consideration of the other two residual stress components in addition to the dominant longitudinal direction has a significant influence on the SIF, and might increase the present modified ΔK values. This might correct the negative correlation of crack growth during the first stage due to, probably overestimation of the influence of the residual stresses. The influence of full-field 3D residual stresses on the crack tip stress fields should ideally be considered in the treatment of crack driving force. This unfortunately could not be dealt with due to time constraint on the project. Further, the residual stresses may be overestimated in any case, as no stress relaxation or redistribution due to applied loads or crack growth was considered in the analysis. The initial steady-state residual stresses associated with LSP+FOD may be altered due to relaxation or redistribution during subsequent fatigue loading and/or crack extension (e.g. Boyce et al., 2006; McClung 2006; Nalla et al., 2003). The magnitude and rate of relaxation have been found to be dependent on the initial residual stress, applied loads and FOD induced stress concentration (Boyce et al., 2003; Sutton et al., 2006). For Ti-6Al-4V, the applied stress needs to be $0.54\sigma_y$ (at R=0.1 and N=1 cycle) for stress relaxation to occur under fatigue loading conditions, whilst at $0.35\sigma_y$, little relaxation occurs (Boyce et al., 2003; Sutton et al., 2006). In this study a ratio of $0.41\sigma_y$ for HCF loading was used suggesting less relaxation effects compared to LCF only with a ratio of $0.55\sigma_y$. A higher applied load was required to open the crack under the LCF loads. Once a crack is initiated, the FCGR is faster due to significant residual stress relaxation caused by the high applied loads. By contrast for HCF cycles, where the crack closure effect is much lower than that in LCF cycles, a crack may be initiated at lower loads, resulting in less residual stress relaxation and a lower crack growth rate. In addition, upon the formation of a fatigue crack, the residual stress relaxation might occur even further due to the stress-concentration effect at the crack tip and plasticity associated with the crack (Boyce et al., 2003). These effects were not considered in the current study.

Residual stress relaxation will generally affect the ΔK and, specifically, increasing the ΔK values in the early crack growth stage. In addition, considering 3D residual stresses to calculate the crack driving force will be more accurate. It is possible that the negative slope in the da/dN vs ΔK plots is due to the inaccuracy of the estimated crack driving force caused by neglecting the above mentioned effects, which is a subject of further work.

Fatigue crack growth rates from specimens with FOD only and specimens with LSP+FOD for head-on impacts are correlated with the modified ΔK and the results are presented in Figure 6-8 for a) LCF, b) HCF, and c) combined LCF and HCF loading conditions. A good agreement in the overall trend of the FCG correlations has been achieved, suggesting consistency in the approach for residual stress modified SIF solutions. Early crack growth data in the current study for LSP+FODed specimens reveal more information in the early crack growth stage, compared to FODed only specimens (Figs. 6-9a, b).

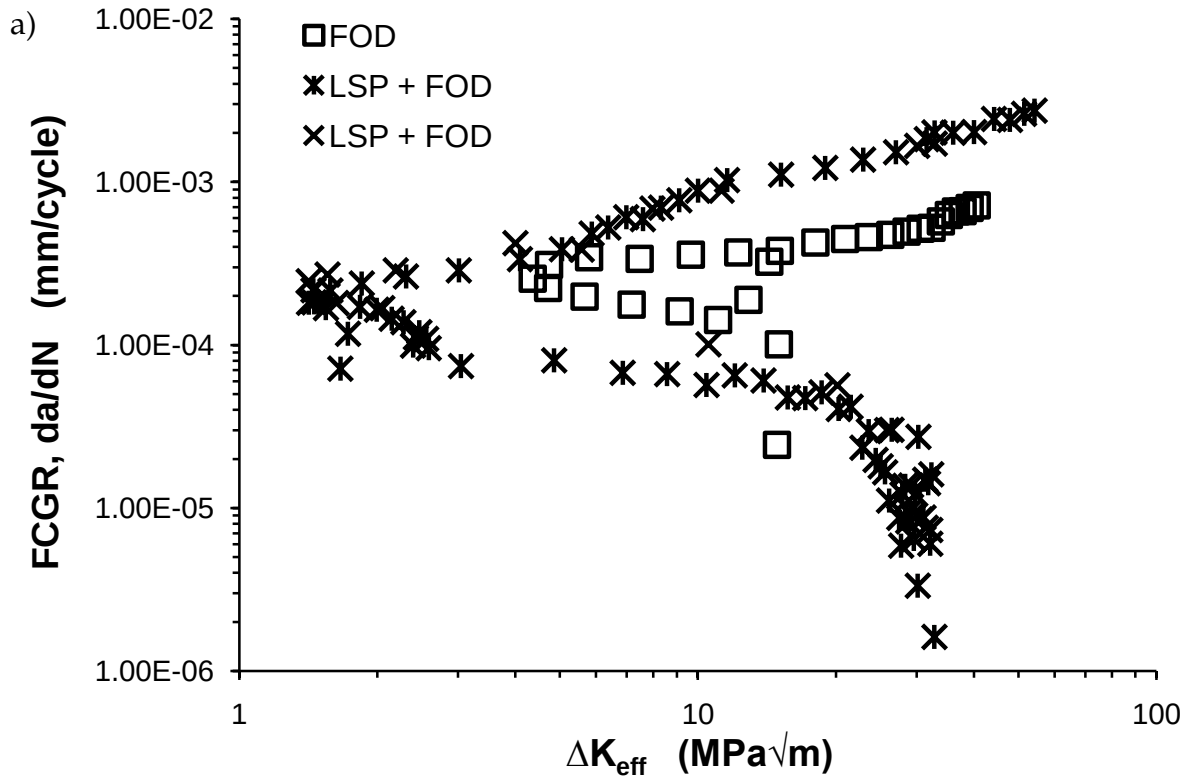

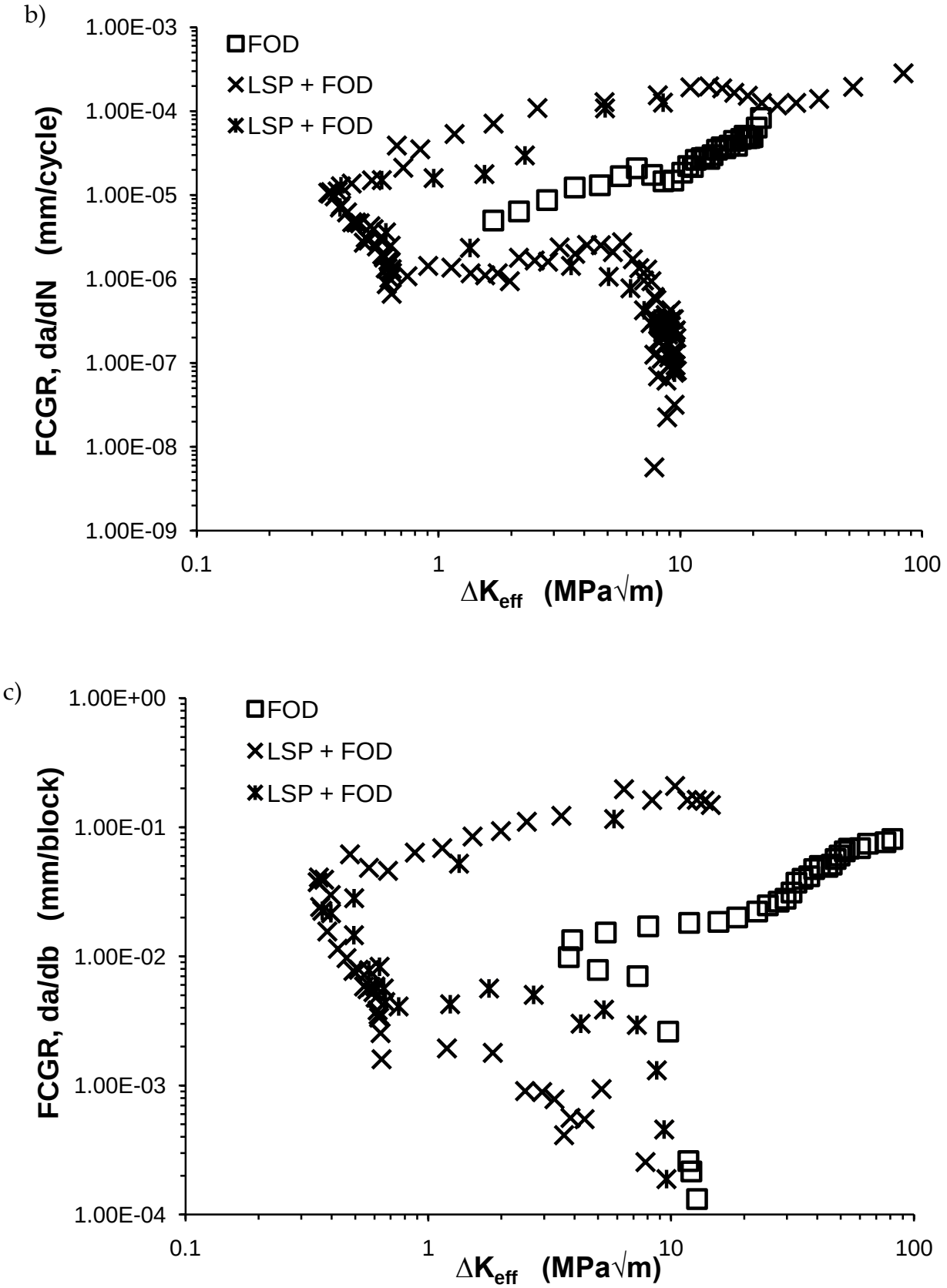

Figure 6-9 Comparison of fatigue crack growth rates correlated with the modified stress intensity factor for a specimen with FOD only and specimens with LSP+FOD for loading conditions a) LCF cycles only, R=0.1, b) HCF cycles only, R=0.7, and c) LCF+HCF, R=0.1 and R=0.7, n=1:1000.

Characteristics for fatigue crack growth in LSP+FODed specimens as opposed to that in FODed specimens are:

- a higher ΔK is required for the onset crack growth under LCF, HCF only conditions but similar for LCF+HCF conditions;
- a slower crack growth rate in the early crack growth stage even at a higher applied stress due to the higher residual stresses;
- an accelerated crack growth rate after the ΔK minimum is reached;

LSP seems to have a major beneficial effect on the early crack growth where the residual stresses cause retardation in the FCCR, but this effect might be reversed once the minimum crack driving force is reached, as crack growth rates can increase thereafter significantly due to the decay of the compressive residual stresses, together with the higher applied load compared to those in the unpeened specimens.

Despite a similar trend for the FCR correlations under all loading conditions, a significant difference can be seen between the FODed only and LSP+FODed specimens at the low ΔK values. For both specimen types, residual stress relaxation effects were not considered. Further investigations considering residual stress relaxation effects might bring together the FCG correlations for LSP+FODed and FOD only specimens.

6.2.6 Effects of loading mode on fatigue limit

The type of fatigue loading can affect fatigue crack initiation and growth. Figure 6-10 shows the fatigue limit stress determined by the load increment scheme as described in Chapter 2, normalised by the ultimate tensile strength (UTS), as a function of notch depth, for samples subjected to head-on and 45° impacts under low cycle fatigue (LCF) and combined low cycle and high cycle fatigue (LCF+HCF) loading conditions.

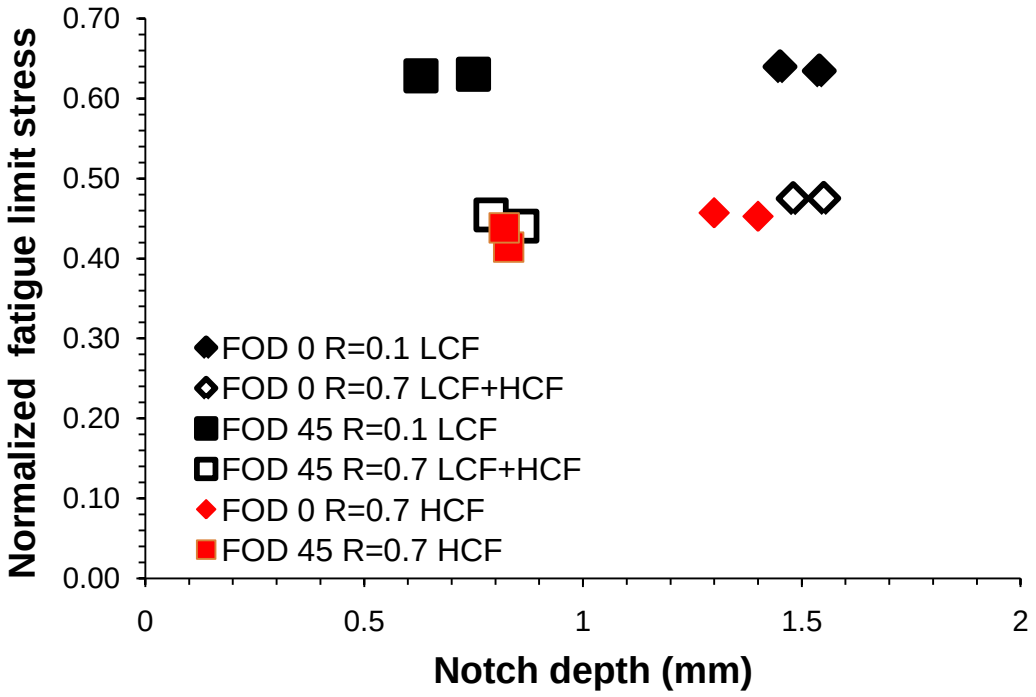

Figure 6-10 The effects of notch depth, impact angle and loading condition on the fatigue limit stress.

Figure 6-10 shows that the type of loading can significantly affect the fatigue limit stress. The superposition of high cycles in a low cycle can reduce the fatigue limit stress by as much as 25% in head-on impacts, and 29% in 45° impacts. This seems to indicate the detrimental role of high frequency loading cycles, which are important during the cruise phase of a flight cycle. It is possible that these load cycles at R=0.7 are effective without the beneficial closure influence of the residual stresses that is likely to be operative at R=0.1. Hence a combined loading block resulted in earlier crack initiation and growth than that under pure low cycle fatigue at R=0.1.

6.3 Conclusions

The fatigue crack growth behaviour in laser shock peened Ti-6Al-4V aerofoil specimens subjected to two types of FOD impact has been investigated for three selected loading conditions. The results indicate that residual stresses due to LSP and FOD play a key role in influencing the fatigue crack growth, resulting in a significant reduction in fatigue crack growth rates compared to those FODed only specimens of the same alloy. The following conclusions may be drawn:

1. The DCPD method is an accurate and reliable method for detecting and monitoring crack growth even for complex shaped specimen geometries.
2. Reduced fatigue crack growth rates were obtained for LSP+FODed samples over FODed only samples of the same material.
3. FOD at 45º seems more detrimental than head-on impact concerning fatigue crack growth due to the difference in the residual stress distribution as well as damage features associated with the impact angle (Chapter 4).
4. Significantly higher stress levels were required to grow cracks in LSPed specimens for all loading conditions. Reduced crack growth rates were also obtained in these specimens, most notably at low R ratios.
5. The beneficial effects of LSP seem to be significantly less for HCF and LCF+HCF conditions than that for LCF condition.
6. A modified stress intensity factor considering longitudinal residual stresses has been used to correlate the fatigue crack growth rates, where a negative correlation in the early crack growth regime was obtained. Consideration of 3D residual stresses may be necessary to improve the correlation.
7. LSP seems to have a major effect on the early crack growth regime, affecting the load ratio and reducing the stress intensity factor at the crack tip.
8. Fatigue crack growth rates in LSP treated specimens become significantly higher than that FODed only samples after the peak residual stress is reached.

9. Crack arrest after crack initiation might be due to the increased compressive residual stresses post crack initiation and their retardation effect on crack growth.
10. Residual stress relaxation and 3D residual stresses were not taken into account in the current analyses; both may have significant influence on crack driving forces such as SIF.

6.4 References

Bao, R., Zhang, X., Yahaya, NA., 2010. Evaluating stress intensity factors due to weld residual stresses by the weight function and finite element methods. Engineering Fracture Mechanics 77, 2550-2566.

Beghini, M., Bertini, L., 1990. Fatigue crack propagation through residual stress fields with closure phenomena. Engineering Fracture Mechanics 36, 379-387.

Beghini, M., Bertini, L., Vitale, E., 1994. Fatigue crack growth in residual stress fields: experimental results and modelling. Fatigue & Fracture of Engineering Materials & Structures 17, 433-444.

Boyce, B.L., Chen, X., Peters, J.O., Hutchinson, J.W., Richie, R.O., 2003. Mechanical relaxation of localized residual stresses associated with foreign object damage. Materials Science and Engineering A349, 48-58.

Elber, W., 1970. Fatigue crack closure under cyclic tension. Engineering Fracture Mechanics 2, 37-45.

Ge, Y.Z., Sutton, M.A., Deng, X., Reynolds, A.P., 2006. Limited weld residual stress measurements in fatigue crack propagation: Part I. Complete field representation through least-squares finite-element smoothing. Fatigue & Fracture of Engineering Materials & Structures 29, 524–536.

Hall, R., Byrne J., Zhao, T., Tong, J., 2008. Influence of foreign object damage on fatigue crack growth of gas turbine aerofoils under complex loading conditions. Fatigue & Fracture of Engineering Materials & Structures 31, 386-397.

Hatamleh, O., 2009. A comprehensive investigation on the effects of laser and shot peening on fatigue crack growth in friction stir welded AA 2195 joints. International Journal of Fatigue 31, 974-988

Hatamleh, O., Lyons, J., Forman, R., 2007. Laser and shot peeining effects on fatigue crack growth in friction stir welded 7075-T7351 aluminum alloy joints. International Journal of Fatigue 29, 421-434.

Hatamleh, O., Hill, M., Forth, S., Garcia, D., 2009. Fatigue crack growth performance of peened friction stir welded 2195 aluminum alloy joints at elevated cryogenic temperatures. Material Science and Engineering A 519, 61-69.

Hill, M., 1996. Determination of residual stress based on the estimation of eigenstrain. Ph.D. thesis. Stanford University, US.

James, M.N., Hughes, D.J., Hattingh, D.G., Bradley, G.R., Mills, G., Webster, P.J., 2004. Synchrotron diffraction measurment of residual stresses in fricton stir welded 5383-H321 aluminium butt joints and their modification by fatigue cycling. Fatigue & Fracture of Engineering Materials & Structures 27, 187-202.

Krug, T., Lang, K.H., Fett, T., Loehe, D., 2007. Influence of residual stresses and mean load on the fatigue strength of case-hardened notched specimens. Materials Science and Engineering A 468-470, 158-163.

Liljedahl, C.D.M., Zanellato, O., Fitzpatrick, M.E., Lin, J., Edwards, L., 2010. The effect of weld residual stresses and their re-distribution with crack growth during fatigue under constant amplitude loading. International Journal of Fatigue 32, 735-743.

Mall, S., Hamrick, JL, Nicholas, T. 2001. High cycle fatigue behaviour of Ti-6Al-4V with simulated foreign object damage. Mechanics of Materials 33, 679-692.

Masona, J.J., Ritchie, R.O., 1997. Fatigue crack growth resistance in SiC particulate and whisker reinforced P:M 2124 aluminium matrix composites. Material Science and Engineering A 231, 170-182

McClung, R.C, 2006. A literature survey on the stability and significance of residual stresses during fatigue. Fatigue & Fracture of Engineering Materials & Structures 30, 173-205.

Nalla, R.K., Altenberger, I., Noster, U., Liu, G.Y., Scholtes B., Ritchie, R.O., 2003. On the influence of mechanical surface treatments - deep rolling and laser shock peening - on the fatigue behavior of Ti-6Al-4V at ambient and elevated temperatures. Material Science and Engineering A355 216-230.

Noroozi, A.H, Glinka, G., Lambert, S., 2007. A study of the stress ratio effects on fatigue crack gorwth using the unified two-parameter fatigue crack growth driving force. International Journal of Fatigue 29, 1616-1633.

Nowell, D., Duo, P., Stewart, I.F., 2003a. Prediction of fatigue performance in gas turbine blades after foreign object damage. International Journal of Fatigue 25, 963-969.

Pavier, M.J., Poussard, C.G.C., Smith, D.J., 1999. Effect of residual stress around cold worked holes on fracture under superimposed mechanical load. Engineering Fracture Mechanics 63, 751-773.

Prevey, P.S., Jayaraman, N., Ravindranath, R., 2004a. HCFperformance and FOD tolerance improvement in Ti-6Al-4V vanes with LPB treatment. Proceedings 42nd AIAA Aerospace Science Meeting Reno, NV.

Prevey, P.S., Jayaraman, N., Shepard, M.J., 2004b. Improved HCF performance and FOD tolerance of surface treated Ti-6-2-4-6 compressor blades. 9th National Turbine Engine High Cycle Fatigue Conference, Pinehurst, NC.

Rooke, D.P., Cartwright, D.J., 1976. Compendium of stress intensity factors. London: Ministry of Defence.

Rubio-Gonzalez, C., Ocana, J.L., Gomez-Rosas, G., Molpeceres, C., Paredes, M., Banderas, A., Porro, J., Morales, M., 2004. Effect of laser shock processing on fatigue crack growth and fracture toughness of 6061-T6 aluminum alloy. Material Science and Engineering A386, 291-295.

Rubio-Gonzalez, C., Felix-Martinez, C., Gomez-Rosas, G., Ocana, J.L., Morales, M., Porro, J.A., 2011. Effect of laser shock processing on fatigue crack growth of duplex stainless steel. Materials Science and Engineering A 528, 914-919.

Ruschau, J.J., Reji, J., Thompson, S.R., Nicholas, T., 1999a. Fatigue crack growth rate characteristics of laser shock peened Ti-6Al-4V. Journal of Engineering Materials and Technology 121, 321-329.

Ruschau, J.J., Reji, J., Thompson, S.R., Nicholas T., 1999b. Fatigue crack nucleation and growth rate behaviour of laser shock peened titanium. International Journal of Fatigue, 199-209.

Ruschau, J.J., Nicholas, T., Thompson, S.R., 2001. Influence of foreign object damage (FOD) on the fatigue life of simulated Ti-6Al-4V airfoils. International Journal of Impact Engineering 25, 233-250.

Ruschau, J.J., Thompson, S.R., Nicholas, T., 2003. High cycle fatigue limit stresses of airfoils subjected to foreign object damage. International Journal of Fatigue 25, 955-962.

Servetti, G., Zhang, X., 2009. Predicting fatigue crack growth rate in a welded butt joint: the role of effective R ratio in accounting for residual stress effect. Engineering Fracture Mechanics 76, 1589-1602.

Sutton, M.A., Reynolds, A.P., Ge, Y.Z., Deng, X., 2006. Limited weld residual stress measurements in fatigue crack propagation: Part II, FEM-based fatigue crack propagation with complete residual stress fields. Fatigue & Fracture of Engineering Material & Structure 29, 537–545.

Thompson, S.R., Ruschau, J.J., Nicholas, T., 2001. Influence of residual stresses on high cycle fatigue strength of Ti-6Al-4V subjected to foreign object damage. International Journal of Fatigue 23, 405-412.

Chapter 7 Conclusions and further work

This chapter summarises the main conclusions of this work and recommends for further work.

7.1 Conclusions

1. The DCPD method is an accurate and reliable method for detecting and monitoring crack growth even for complex shaped specimen geometries under the influence of residual stresses.
2. Impact damage from ballistically simulated cubical FOD at two impact speeds and angles may be characterised by the damage features identified as: Micro-notches, material pile-up/folding, material shear, shear bands and fretting fatigue. These features may be correlated with multiple crack initiation and early crack growth on different crack planes. The impact damage due to 45° impacts seems to be more severe compared to that due to 0° impacts.
3. Compared with spherical FOD impacts, FOD damage due to cubical impacts is more severe and more likely to prompt subsequent fatigue crack initiation and growth at a given impact speed.
4. Both the weight function method and the finite element method are able to provide modify stress intensity factors considering the residual stresses from FOD and LSP. The results of both methods compare very well for small crack length and overall acceptable for the range of cracks investigated.

5. Reduced fatigue crack growth rates were obtained for LSP+FODed samples over FODed only samples of the same material. Significantly higher stress levels were required to grow cracks in LSPed specimens for all loading conditions. The beneficial effects of LSP seem to be notably less for HCF and LCF+HCF conditions than that for LCF condition. FOD at 45° seems to be more detrimental than head-on impact concerning fatigue crack initiation and growth, due to the difference in the residual stress distribution as well as damage features associated with the impact angle.
6. LSP seems to have a major effect on the early crack growth regime, affecting the load ratio and reducing the stress intensity factor at the crack tip such that a negative correlation in the early crack growth regime was obtained. Crack arrest after crack initiation might be due to the increased compressive residual stresses post crack initiation and their retardation effect on subsequent crack growth. Fatigue crack growth rates in LSP treated specimens become significantly higher than those FODed only samples after the peak compressive residual stress is reached.
7. Residual stress relaxation and 3D residual stresses were not taken into account in the current analyses; both may have significant influence on the crack driving force SIF. Consideration of full 3D residual stresses may improve the correlation of modified SIF with the fatigue crack growth rates, particularly in the early crack growth regime.

7.1 Further work

The work undertaken in this study has highlighted a number of areas which warrant further investigation to understand the fatigue process during crack growth. Some suggestions are given here.

Internal crack initiation

The investigation of internal cracking might be significant for the determination of service intervals and to prove if NDI techniques are sufficient to detect internal initiated cracks. In addition, if internal cracking is the major initiation mechanism in the specimens investigated, LSP parameters might have to be adjusted and optimised to find a balance between the residual stress introduced and the surface induced crack initiation. Further experimental studies might include fracture surface investigations by SEM, 3D imaging of crack growth via X-ray computer tomography (CT) to investigate crack nucleation and growth in the early stage; and periodical CT scans of the crack growth to study the phenomena of crack coalescence. Comparison of crack initiation areas with residual stress maps may be obtained whether by FE modelling, or X-ray diffraction to investigate the influence of 3D distribution of the residual stresses due to FOD and LSP.

The effect of residual stress on crack growth under LCF, HCF and combined LCF and HCF loading conditions

Experimental measurement of crack closure may be followed to further investigate the results obtained from this study, i.e. LSP has a more beneficial effect on low R ratios compared to high R ratios. An appropriate method might be the application of a laser interferometric strain/displacement gage (ISDG) with a resolution of 5nm, to obtain data of applied load versus crack-mouth-opening displacement, measurements of crack-opening compliance and observations of crack closure can be obtained. Computerization makes real-time analysis of the data possible and it can efficiently handle the large quantity of data required. Further SEM investigations of

fracture surfaces and mapping of crack initiation areas, fracture surface investigations close to the notch, may also find artefacts of crack closure (smeared faces) like in (Ruschau et al., 1999a; 1999b).

Crack driving force under full 3D residual stresses and residual stress relaxation

To improve the estimation of the crack driving force more knowledge on the residual stress distributions and their behaviour under fatigue and environmental conditions need to be investigated, including:

- Full 3D residual stress distribution utilised to obtain a balanced residual stress field;
- periodically measured RS field after fatigue cycles, crack initiation, and crack growth to develop an empirical mathematical residual stress relaxation model;
- investigate thermal effects, which might be below room temperature as the fan blades are in an environment subzero degrees;

Chapter 8 Conference presentations and papers produced during the course of this work

Spanrad, S., Tong, J., 2010. Characterization of foreign object damage (FOD) and early fatigue crack growth in laser shock peened Ti-6AL-4V aerofoil specimens. International Congress of Fatigue, Prague, Czech Republic.

Zabeen, S., Preuss, M., Spanrad, S., Tong, J., Withers, P.J., 2010. Laser shock peening: A solution to foreign object damage problem. The second international conference on laser peening. San Francisco, CA, US.

Zabeen, S., Preuss, M., Wang, H-T., Spanrad, S., Tong, J., Withers, P.J., 2009. A synchroton x-ray study of residual strain distribution around foreign object damage in laser shock peened Ti-6Al-4V alloy. MECA SENS conference, Mito, Japan.

Tong, J., Wang, H-T., Zhao, T., Spanrad, S., Hall, R., Byrne, J., 2008. FOD characterisation and its influence on FCG of aerofoils under HCF+LCF loading conditions. International Conference on Fatigue Damage of Structural Materials VI, Cape Cod, Hyannis, MA, US.

Spanrad, S., Tong, J., 2011. Characterization of foreign object damage (FOD) and early fatigue crack growth in laser shock peened Ti-6AL-4V aerofoil specimens. Material Science and Engineering A 528, 2128-2136 .

Spanrad, S., Tong, J., 2010. Characterization of foreign object damage (FOD) and early fatigue crack growth in laser shock peened Ti-6AL-4V aerofoil specimens. Procedia Engineering, Vol. 2: 1751–1759.

Zabeen, S., Preuss, M., Withers, P.J., Spanrad, S., Tong, J., Schofield, J., 2010. Synchrotron strain mapping of the residual strain distribution around foreign object damage in laser shock peened Ti-6AL-4V alloy. Materials Science Forum, Vol. 652, 19-24.

Appendices

A Technical drawings of the four-point bend rigs

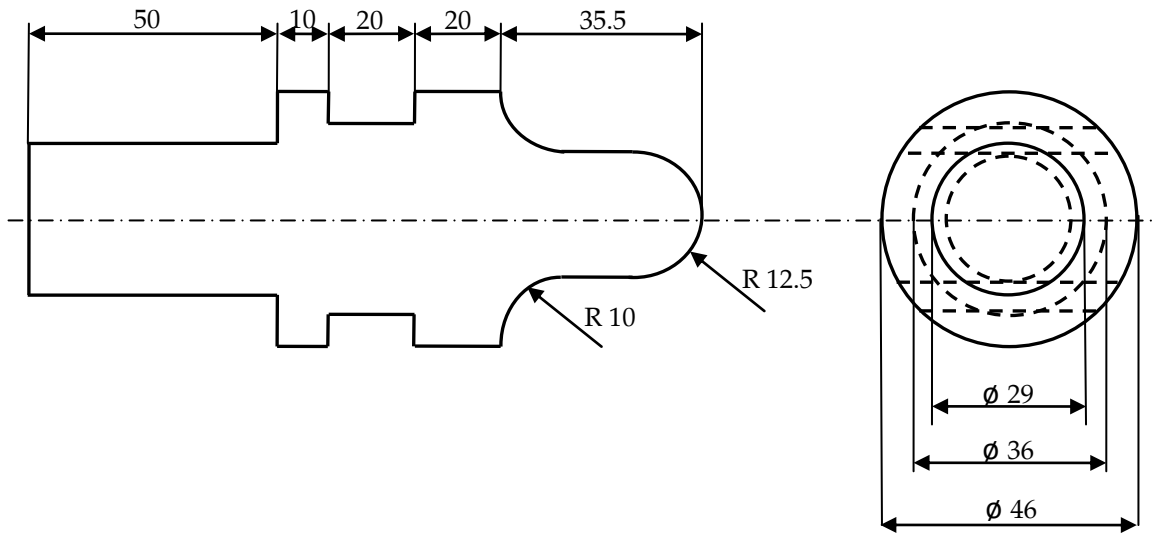

Figure A-1 Technical drawing of the connection bar with all dimensions in mm.

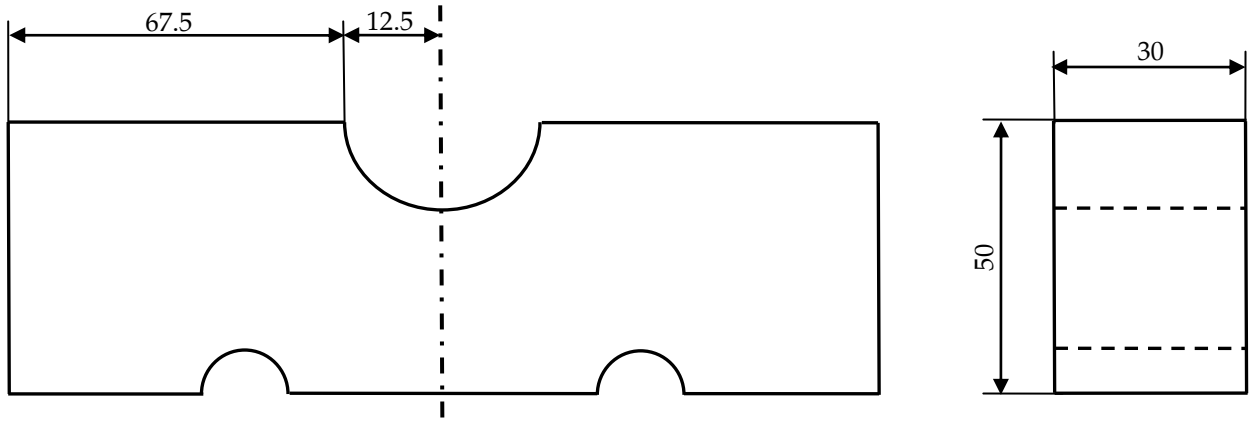

Figure A-2 Technical drawing of the loading beam with all dimensions in mm.

B Table of impact conditions

Table B-1 Summary of the FOD impact parameters.

Edge First 0°, 200m/s, 3.2mm cube		
Shot No.	**Velocity (m/s)**	**Notch depth (mm)**
1	195	1.55
2	192	1.37
3	193	1.40
4	193	1.12
5	196	1.49
6	204	1.49
7	199	1.54
8	202	1.48
9	198	1.47

Point First 45°, 250m/s, 4.8mm cube		
Shot No.	**Velocity (m/s)**	**Notch depth (mm)**
1	240	0.75
2	247	0.63
3	247	0.73
4	247	0.86
5	245	0.82
6	250	0.79
7	247	0.78
8	239	0.83
9	247	0.82

C Contour integrals of residual SIFs

Table C-1 Contour integrals of residual SIF for FOD 0°

	Stress intensity factor K $\left(MPa\sqrt{mm}\right)$					Crack (mm)
	1st	2nd	3rd	4th	5th	
Tip_1	-358.5	-358.2	-358.3	-358.	-358.	1.68
Tip_2	-1043	-1042	-1043	-1043	-1043	2.18
Tip_3	-1261	-1260	-1261	-1261	-1261	2.68
Tip_4	-1352	-1351	-1352	-1352	-1352	3.18
Tip_5	-1469	-1468	-1468	-1468	-1468	3.68
Tip_6	-1542	-1540	-1541	-1541	-1541	4.18
Tip_7	-1557	-1556	-1556	-1556	-1556	4.68
Tip_8	-1562	-1561	-1561	-1561	-1561	5.18
Tip_9	-1576	-1575	-1575	-1575	-1575	5.68
Tip_10	-1447	-1446	-1446	-1446	-1446	6.18
Tip_11	-1264	-1263	-1263	-1263	-1263	6.68
Tip_12	-1148	-1147	-1147	-1147	-1147	7.18
Tip_13	-1069	-1069	-1069	-1069	-1069	7.68
Tip_14	-1017	-1017	-1017	-1017	-1017	8.18
Tip_15	-979.5	-978.8	-979.0	-979.0	-979.0	8.68
Tip_16	-946.0	-945.3	-945.5	-945.5	-945.6	9.18
Tip_17	-911.8	-911.1	-911.3	-911.3	-911.3	9.68
Tip_18	-878.6	-878.0	-878.1	-878.2	-878.2	10.18
Tip_19	-857.3	-856.7	-856.9	-856.9	-856.9	10.68

Table C-2 Contour integrals of residual SIF for FOD 45°

	Stress intensity factor K $\left(MPa\sqrt{mm}\right)$					Crack (mm)
	1st	2nd	3rd	4th	5th	
Tip_1	-90.22	-90.15	-90.17	-90.17	-90.17	1.03
Tip_2	-564.4	-545.0	-545.2	-545.	-545.	1.53
Tip_3	-998.4	-997.7	-997.9	-997.9	-997.9	2.03
Tip_4	-1187	-1186	-1186	-1186	-1186	2.53
Tip_5	--1314	-1313	-1313	-1313	-1313	3.03
Tip_6	-1399	-1399	-1399	-1399	-1399	3.53
Tip_7	-1452	-1451	-1451	-1451	-1451	4.03
Tip_8	-1489	-1488	-1488	-1488	-1488	4.53
Tip_9	-1529	-1528	-1528	-1528	-1528	5.03
Tip_10	-1498	-1497	-1497	-1497	-1497	5.53
Tip_11	-1347	-1346	-1346	-1346	-1346	6.03
Tip_12	-1201	-1200	-1200	-1200	-1200	6.53
Tip_13	-1090	-1083	-1085	-1085	-1085	7.03
Tip_14	-1004	-1003	-1003	-1003	-1003	7.53
Tip_15	-948.2	-947.6	-947.8	-947.8	-947.8	8.03
Tip_16	-908.1	-907.4	-907.6	-907.7	-907.7	8.53
Tip_17	-873.4	-872.8	-873.0	-873.0	-873.0	9.03
Tip_18	-837.8	-837.2	-837.4	-837.4	-837.4	9.53
Tip_19	-800.9	-800.3	-800.5	-800.5	-800.5	10.03
Tip_20	-770.6	-770.1	-770.2	-77.3	-770.3	10.53